This is to certify that the
dissertation entitled

ANALYSIS AND CONTROL OF AN IPMSM FOR TRACTION APPLICATIONS

presented by

CARLOS EDUARDO NINO-BARON

has been accepted towards fulfillment
of the requirements for the

PhD degree in ELECTRICAL ENGINEERING

Elias G Strangas

Major Professor's Signature

02 NOVEMBER 2010

Date

MSU is an Affirmative Action/Equal Opportunity Employer

DATE DUE	DATE DUE	DATE DUE

5/08 K:/Proj/Acc&Pres/CIRC/DateDue.indd

ANALYSIS AND CONTROL OF AN IPMSM FOR TRACTION APPLICATIONS

By

Carlos Eduardo Nino-Baron

A DISSERTATION

Submitted to
Michigan State University
in partial fulfillment of the requirements
for the degree of

DOCTOR OF PHILOSOPHY

Electrical Engineering

2010

ABSTRACT

ANALYSIS AND CONTROL OF AN IPMSM FOR TRACTION APPLICATIONS

By

Carlos Eduardo Nino-Baron

This thesis presents methodologies to optimally design controllers of Interior Permanent Magnet Synchronous Motors (IPMSM's) for traction applications. These controllers include: optimal current reference calculation, optimal torque-speed trajectory design and sensorless control.

The design of the current controller reference requires an accurate machine model; the selected model was a cross saturated model. Cross-magnetization and saturation produce a reduction of the maximum power of the machine; their accurate calculation allows us to predict the generated torque and the stator voltage in the machine under field weakening. The current controller reference is based on maximum torque per ampere and field weakening; this current reference is designed such that the motor can operate with minimal losses over the whole speed and torque range while satisfying voltage and current limits.

Optimal trajectory design is used to generate the speed and torque references for two subsystems in a series Hybrid Electric Vehicles (HEV): traction motors and engine-generator. The trajectory optimization of the traction motors is designed to minimize losses while achieving the speed requirements. The trajectory of the engine-generator subsystem is designed to produce a requested amount of energy in a given period of time while minimizing the energy losses.

Sensorless control deals with the issues in practical implementation of the high-frequency injection methods for control of IPMSM machines without shaft position sensors. The controller is based on the high-frequency injection method, the injection is combined with an sliding mode observer eliminating the requirements of low-pass

filters and improving the performance of the torque controller and hence improving the machine efficiency.

Simulation and experimental results are presented to validate the proposed controllers.

DEDICATION

I dedicate this thesis to my wife Solimar Reyes Rodriguez, who offered me unconditional love and support throughout the course of this thesis. To my parents Jose Armando Nino and Maria del Carmen Baron, my sister Monica Andrea Nino and niece Lina Maria Camargo, for their love and unconditional support all the way since the beginning of my studies.

ACKNOWLEDGMENT

Dr. Elias Strangas has been the ideal thesis advisor and great friend. His sage advice, insightful criticisms, and patient encouragement aided the writing of this thesis in innumerable ways. I wish to thank my committee members who were more than generous with their expertise and precious time: Dr Hassan K. Khalil , Dr Guoming (George) Zhu, Dr Fang Z. Peng and Ranjan Mukherjee. I would also like to thank all my friends in the electrical and machines laboratory Sajjad, Tariq, Sinisa, Wes, John, and many other for their help and time.

TABLE OF CONTENTS

LIST OF TABLES

LIST OF FIGURES

Chapter 1

Introduction

Hybrid Electric Vehicles (HEV's) combine a conventional propulsion system (that includes an internal combustion engine), electric drives, and an energy storage system. The combination of these devices improves the efficiency of the vehicle. The efficiency increase is due to a more efficient operation of the drivetrain, the recovery of the energy during the braking and the engine size reduction. The braking energy is captured by the traction motors, converted through inverters and stored in batteries. During the acceleration, some energy is provided by the batteries, which makes the power requirements of the engine to be less. The flow of energy back and forth produces losses in each element, therefore, an efficient design and control of each device and the integration of all of them improves the efficiency of the whole system.

1.1 Contributions

This thesis present methodologies to design controllers used for Interior Permanent Magnet Synchronous Motors (IPMSM) for traction applications. These controllers are explained and their performance is evaluated and compared to other controllers. The contributions of this thesis to the proposed controllers design are summarized

below.

1.1.1 Cross Saturation Analysis

The cross saturation is a phenomenon in ac electric machines, where the saturation of the iron core causes direct and quadrature axis current components to affect perpendicular fluxes to them. The contributions related to this issue are:

- Develop and apply a methodology to calculate the self and the quasi-mutual inductances and their dependencies on the currents using flux estimation. These inductances are used to model the cross saturation effect.

- Develop and validate a methodology to calculate the optimal current commands to control the IPMSM over the whole operation range with minimal losses by the inclusion of cross saturation effect.

1.1.2 Trajectory Optimization

This thesis present two cases where trajectory optimization was used: Optimal speed control of a traction motor and optimal torque-speed control of engine-generator subsystem, both applied to a series hybrid electric vehicle. The trajectory optimization was used to transfer the system from one operating point to another with minimal energy losses. The main contributions in trajectory optimization are:

- Apply the trajectory optimization to the speed control of an IPMSM by transferring the system from one torque speed point to another with minimal energy losses. Develop an approximation to the optimal trajectory to use it in real time.

- Apply the trajectory optimization, in the subsystem engine-generator, to determine the optimal torque and speed commands in order to produce a requested

energy in a fixed time, while minimizing the energy losses. Develop an approximation to the optimal trajectory to use it in real time.

1.1.3 Sensorless Control

Rotor position sensing requires resolvers or encoders. An alternative is to operate the machine with a rotor position estimator. High frequency injection for sensorless control is used for low speed operation. The main contribution in sensorless control of IPMSM is:

- Design a new controller based on the high-frequency injection method that eliminates the need for low-pass filtering for sensorless operation while improving the motor performance.

1.2 Thesis Organization

The thesis presented here has the following content: Chapter 2 presents the basic configurations of the Permanent Magnet Synchronous Motor (PMSM): rotor structures, magnets location and windings distribution. The concepts of two axis model and field oriented control are presented. The basic criteria to determine the currents commands, based on maximum torque per ampere and field weakening, is described.

Chapter 3 describes the cross saturation and presents the machine model which includes this effect. This model is the most accurate and suitable for control. First the flux linkages calculation is shown in sections 3.1 and 3.2; the results of these sections justify the cross saturation analysis. Section 3.3 explains the cross saturation concept and its effect in the machine performance. Section 3.4 describes the methodology used to extract the machine parameters from the flux linkages calculation. The proposed methodology is validated with FEA simulations, and the model of a prototype machine is calculated.

Chapter 4 presents the optimization of the speed reference for the traction motor controller in series HEV. Section 4.1 describes the optimization problem. The trajectory calculation is done by a multistage optimization. Section 4.2 presents the optimization of the current commands to operate the machine at a desired torque and speed point while minimizing its losses. Section 4.3 presents the numerical trajectory optimization to determine speed command. This trajectory defines the torque and speed points in time to transfer the system from one torque and speed point to another while minimizing energy losses. Simulation and experimental results are presented in section 4.4.

Chapter 5 presents the optimization of the torque-speed reference for the controllers of the engine-generator subsystem. Section 5.2 presents the optimization problem and the engine and generator efficiency maps. Section 5.3 describes the trajectory optimization scheme. The minimization problem is described in continuous time and the problem is solved using numerical optimization in discrete time. Simulation results of the proposed trajectory optimization are presented. Section 5.4 presents an approximation to the optimal trajectory. Section 5.5 shows the resulting efficiency and it is compared to non-optimized control techniques.

Chapter 6 presents the design of a high performance sensorless controller for IPMSM. Section 6.2 is divided in two subsections. Subsection 6.2.1 shows the classical approach, where low pass and high pass filters are used for current control and rotor position estimation respectively. Subsection 6.2.2 describes the proposed methodology. Section 6.3 presents and discusses experimental results, where the filtered demodulation and the proposed controller are compared.

Chapter 7 presents the concluding remarks and expected future work. The chapter is subdivided in sections describing the work done in the topics presented in chapters 3, 4, 5 and 6.

Chapter 2

Background

As high efficient electric drives are becoming more important, Permanent Magnet Synchronous Machines are rapidly replacing induction machines.PMSM's offer high power density and lower losses, so they are more suitable in the applications requiring volume reduction e.g. automotive, aircraft, and portable generator industries.

2.1 Permanent Magnet AC Machines Configuration

The permanent magnet synchronous machine is basically an ordinary AC machine with windings in the stator slots so that the flux created by stator current is approximately sinusoidal, and magnets in the rotor that produce a constant flux. The work presented here concentrates on Permanent Magnet Synchronous Machines (PMSM's) with a sinusoidal flux distribution. Rotating permanent magnet synchronous machines used today come in two different configurations: interior and exterior rotor as shown in Figure 2.1.

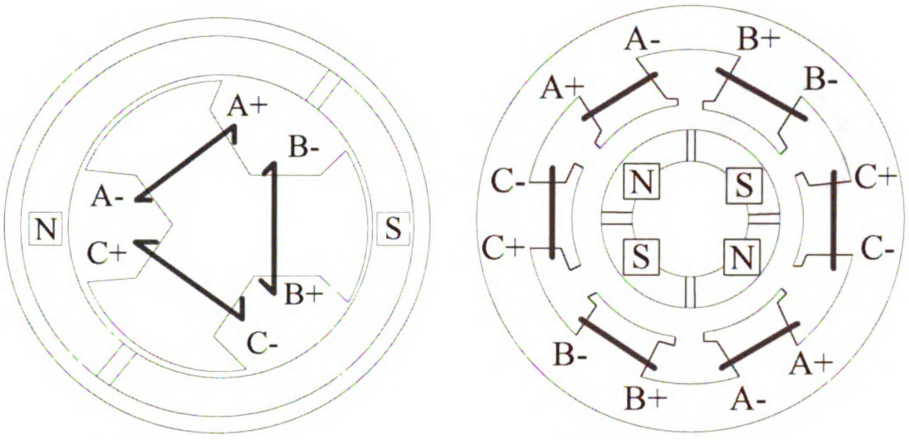

(a) Exterior Rotor (b) Interior Rotor

Figure 2.1: General configuration of a PMSM

2.1.1 Location of the Permanent Magnets

The rotor magnets are the most important elements in the machine; they affect the characteristics of the machine, and their location in the rotor would change maximum torque, maximum speed and power density. Based on the rotor magnets configuration, the PMSM can be: Surface PMSM, Inset PMSM and Interior PMSM as shown in Figure 2.2. In a surface magnet motor the magnets are usually magnetized radially. Due to the use of low permeability rare-earth magnets the synchronous inductances in the d-axis and q-axis may be considered to be equal which can be helpful while designing the motor. The construction of the motor is less expensive and simpler than the other configurations, because the magnets can be attached to the rotor surface. Inset Permanent Magnet (PM) rotor is desirable over surface PM, because it gets an additional component of the torque due to saliency. Inset has a construction more complex than surface PM. The embedded or interior magnet motor has permanent magnets embedded in the deep slots. In the case of an embedded magnet motor, the stator synchronous inductance in the q-axis is often greater than the synchronous inductance in the d-axis, this saliency produces an additional reluctance torque that makes it suitable for traction applications where high torque is required.

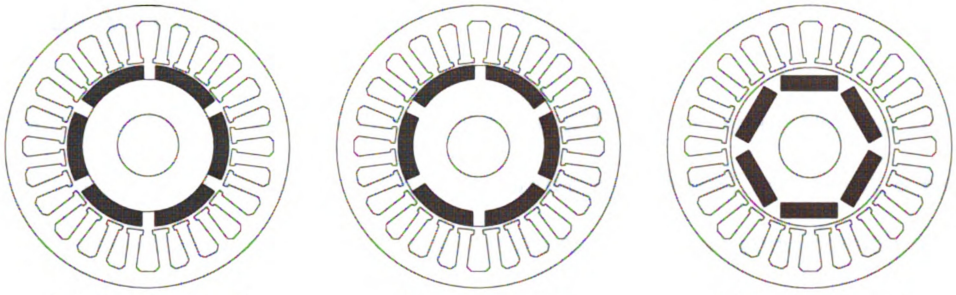

(a) Surface PM (b) Inset PM (c) Interior PM

Figure 2.2: Permanent magnet location

2.1.2 Winding Distribution

The stator windings play an important role in the machine, and their distribution modifies the efficiency and size. Figure 2.3 shows two of the basic configurations: concentrated and distributed windings. Concentrated windings are usually designed for machines with smaller size, however nowadays they have been used for mid power configurations. Their advantage is basically the reduction of end windings, hence the copper losses and leakage flux is reduced. Distributed windings configuration has longer end turns that means more copper losses, however their distribution is used to have a more sinusoidal back-emf and hence this topology allow us to reduce the iron losses.

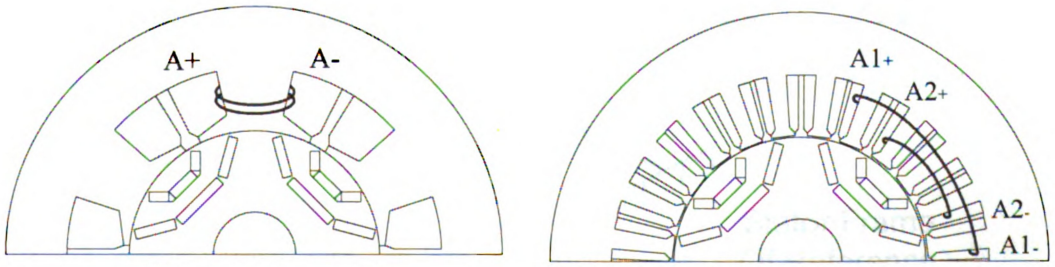

(a) Concentrated (b) Distributed

Figure 2.3: Winding configuration of a PMSM

2.2 2-Axis Model

The PMSM model can be developed in the stator frame of reference or in the rotor frame or reference. The model in the rotor frame is preferred because it is simpler. It allows to decouple the flux into magnetization and torque components; similarly the current can be decomposed in the same fashion. These simplifications make this model suitable for vector control. The phasor diagram of a PMSM is shown in Figure 2.4. The rotor flux linkages are assumed constant and aligned with the direct axis, while the flux component in the quadrature axis is taken as zero. The core losses are neglected. The stator flux is also represented by two components: direct and quadrature fluxes.

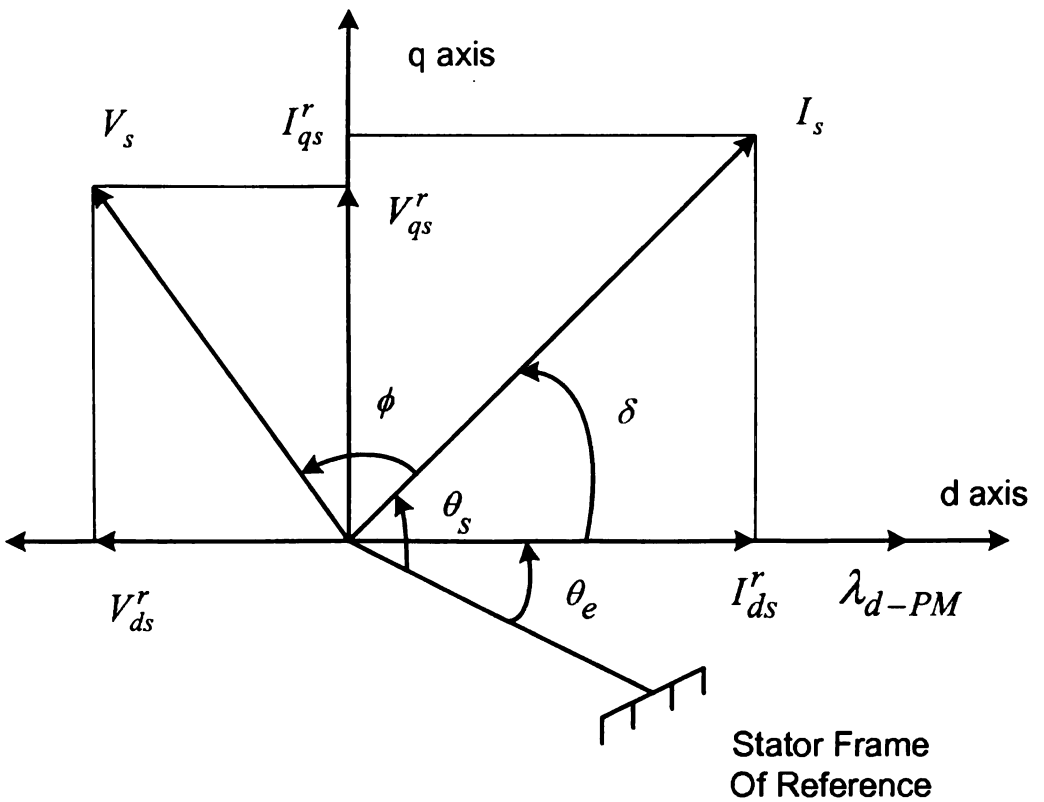

Figure 2.4: Phasor diagram of a PSMS

The stator voltage equations in the rotor frame of reference are:

$$v_d = R_s i_d - \omega_e \lambda_q + \frac{\partial \lambda_d}{\partial t} \tag{2.1}$$

$$v_q = R_s i_q + \omega_e \lambda_d + \frac{\partial \lambda_q}{\partial t} \tag{2.2}$$

where R_s is the stator resistance, v and i are the stator voltage and current and the subscripts d and q refer to the direct and quadrature axes. λ is the the stator flux linkages and ω_e is the electrical frequency. The direct and quadrature axis fluxes in the rotor frame of reference are:

$$\lambda_d = \lambda_{d-PM} + L_d i_d \tag{2.3}$$

$$\lambda_q = L_q i_q \tag{2.4}$$

where λ_{d-PM} is the stator flux linkages due to the PM. The inductances L_d and L_q model the stator flux change due to the stator currents. In general these inductances are not equal, because the reluctance of direct and quadrature paths are not the same. In the IPM of Figure 2.2c, the direct axis reluctance is bigger than quadrature axis reluctance, this produces that $L_d < L_q$. The electrical torque τ_e is given by:

$$\tau_e = \frac{3}{2}\frac{P}{2}\left(\lambda_d i_q - \lambda_q i_d\right) \tag{2.5}$$

where P is the number of poles. By substituting equations 2.3 and 2.4 in 2.5 the torque is calculated as:

$$\tau_e = \frac{3}{2}\frac{P}{2}\left(\lambda_{d-PM} i_q + \left(L_d - L_q\right) i_d i_q\right) \tag{2.6}$$

The first component of the torque, τ_m, is called "PM Torque". This component is due to the interaction between the rotor flux and the quadrature axis current. The

second component, τ_r, is produced due to the relative change of the reluctance of the machine with the rotor position called "Reluctance Torque".

$$\tau_m = \frac{3}{2}\frac{P}{2}\left(\lambda_{d-PM} i_q\right) \tag{2.7}$$

$$\tau_r = \frac{3}{2}\frac{P}{2}\left(\left(L_d - L_q\right) i_d i_q\right) \tag{2.8}$$

$$\tau_e = \tau_m + \tau_r \tag{2.9}$$

2.3 Vector Control

The PMSM vector control is based on the 2-axis model. The operation of the machine is restricted to mechanical and electrical limits. From control systems point of view the electrical limits of the machine are the maximum current and the maximum voltage. The maximum current is determined by the capability to remove heat from the windings and depends on the cooling system; it is usually fixed after the machine design. The maximum voltage is restricted to the peak voltage available from the inverter connected to the machine.

The basic objectives in the motor controller design are to have high dynamic performance, low operational energy losses and operate it within voltage and current limits. The operation in the machine is divided basically in two regions: constant torque and constant power. These regions are separated by the base speed; for speeds below the base, the induced voltage is lower than the maximum available from the inverter. The only restriction there is the current. In this region the criteria commonly selected is to use the maximum torque available restricted by the maximum current. This is called "maximum torque per ampere".

When the machine speed is higher than the base speed, the induced voltage that

is the product of the flux and the speed reaches its maximum. At this point it is necessary to control the flux in order to operate the machine at the voltage limit. The stator current is controlled in a such way that one component i_d reduces the direct axis flux and hence the induced voltage. Under this condition the current limit should be also satisfied. The component i_q is chosen in such way that the current limit is satisfied and the torque produced at this point is maximum but lower than the maximum torque per ampere for the same total current. This control technique is called "direct flux weakening control". Figure 2.5 shows the block diagram used to control the PMSM.

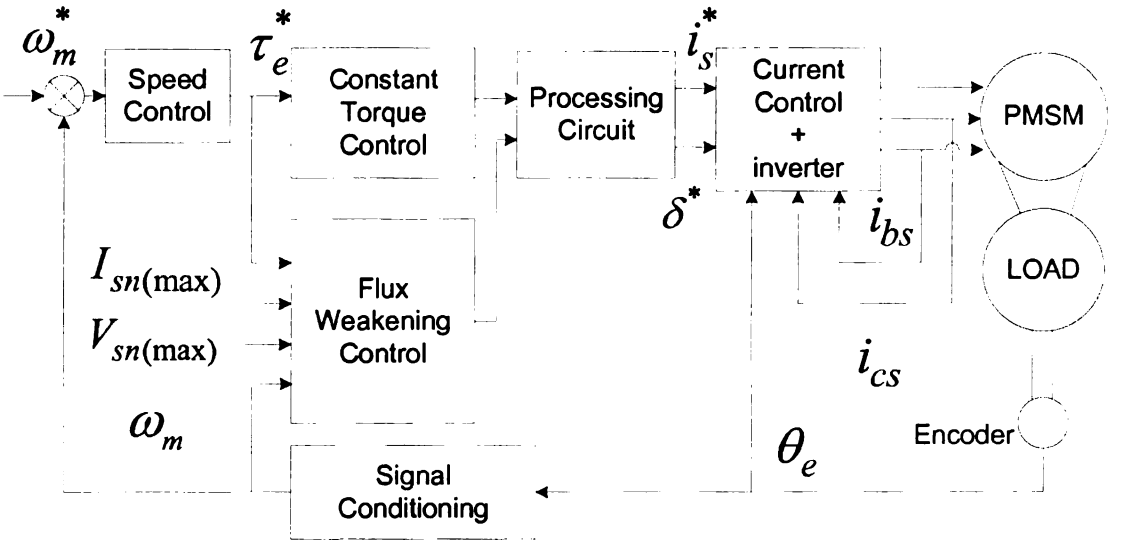

Figure 2.5: Schematic of the PMSM-drive control strategy

2.3.1 Maximum Torque Per Ampere

The Maximum Torque Per Ampere (MTPA) control operates the motor in the region where the induced voltage is lower than the maximum voltage. Then equation 2.6 is satisfied under the restriction of maximum current and to maximum torque production. Lets consider the case where the current is equal to the maximum current $I_{\max}$, this current can be decomposed in terms of i_d and i_q as:

$$i_d = I_{\max}\cos(\delta) \text{ and } i_q = I_{\max}\sin(\delta) \tag{2.10}$$

were δ is the angle of the current space vector. By substituting equation 2.10 in 2.6 the torque is given by:

$$\tau_e = \frac{3}{2}\frac{P}{2}\left(\lambda_{d-PM} I_{\max}\sin(\delta) + \left(L_d - L_q\right) I_{\max}^2 \sin(2\delta)\right) \tag{2.11}$$

The relation of torque per ampere is given by

$$\frac{\tau_e}{I} = \frac{3}{2}\frac{P}{2}\left(\lambda_{d-PM}\sin(\delta) + 0.5 * \left(L_d - L_q\right) I_{\max}\sin(2\delta)\right) \tag{2.12}$$

The angle at where the maximum torque occurs is given by:

$$\frac{\partial\left(\frac{\tau_e}{I}\right)}{\partial\delta} = \frac{\partial}{\partial\delta}\left(\frac{3}{2}\frac{P}{2}\left(\lambda_{d-PM}\sin(\delta) + 0.5 * \left(L_d - L_q\right) I_{\max}\sin(2\delta)\right)\right) = 0 \tag{2.13}$$

solving for δ

$$\delta = \cos^{-1}\left(\frac{-\lambda_{d-PM} + \sqrt{\lambda_{d-PM}^2 + 8I_{\max}^2\left(L_d - L_q\right)^2}}{4\left(L_d - L_q\right) I_{\max}}\right) \tag{2.14}$$

The range of δ should be between 90^0 and 180^0 in order to have positive reluctance torque when $L_d < L_q$, which is the common case in IPMSM's. For an specified value of stator current I_s, the angle is calculated from equation 2.14 and the current commands are calculated from equation 2.10.

2.3.2 Direct Flux Weakening Control

The direct flux weakening control operates the motor in the region defined by the base speed and above. There, the machine has reached the maximum voltage and the current space vector angle δ should be increased as the speed increases. The value of δ is selected such that it maximizes the output torque and keeps the motor in or below the voltage limit. It is clear that in this region equation 2.14 is not longer satisfied. By combining equations 2.1 -2.2 and neglecting the voltage drop in the resistor the maximum voltage in steady state can be written as:

$$\begin{aligned} V_{\max}^2 &= V_d^2 + V_q^2 \\ &= (\omega_e \lambda_q)^2 + (\omega_e \lambda_d)^2 \\ &= (\omega_e L_q I_q)^2 + \left(\omega_e \left(\lambda_{d-PM} + L_d I_d\right)\right)^2 \end{aligned} \tag{2.15}$$

in this region it is also required to produce the maximum torque available, then it is desirable to use the maximum current. The maximum voltage can be written as:

$$V_{\max}^2 = \omega_e^2 \left[L_q^2 \left(I_{\max}^2 - I_d^2 \right) + \left(\lambda_{d-PM} + L_d I_d \right)^2 \right] \tag{2.16}$$

in a compact form equation 2.14 is

$$\begin{aligned} V_{\max} &= \omega_e \sqrt{I_d^2 a + b I_d + \lambda_{d-PM}^2 + c} \; with \\ a &= L_d^2 - L_q^2 \\ b &= 2\lambda_{d-PM} L_d \\ c &= {\lambda_{d-PM}}^2 + L_q^2 I_{\max}^2 \end{aligned} \tag{2.17}$$

For fixed input voltage, speed and stator current, the value of I_d is calculated

2.3.2 Direct Flux Weakening Control

The direct flux weakening control operates the motor in the region defined by the base speed and above. There, the machine has reached the maximum voltage and the current space vector angle δ should be increased as the speed increases. The value of δ is selected such that it maximizes the output torque and keeps the motor in or below the voltage limit. It is clear that in this region equation 2.14 is not longer satisfied. By combining equations 2.1 -2.2 and neglecting the voltage drop in the resistor the maximum voltage in steady state can be written as:

$$\begin{aligned} V_{\max}^2 &= V_d^2 + V_q^2 \\ &= (\omega_e \lambda_q)^2 + (\omega_e \lambda_d)^2 \\ &= (\omega_e L_q I_q)^2 + \left(\omega_e \left(\lambda_{d-PM} + L_d I_d\right)\right)^2 \end{aligned} \tag{2.15}$$

in this region it is also required to produce the maximum torque available, then it is desirable to use the maximum current. The maximum voltage can be written as:

$$V_{\max}^2 = \omega_e^2 \left[L_q^2 \left(I_{\max}^2 - I_d^2 \right) + \left(\lambda_{d-PM} + L_d I_d \right)^2 \right] \tag{2.16}$$

in a compact form equation 2.14 is

$$\begin{aligned} V_{\max} &= \omega_e \sqrt{I_d^2 a + b I_d + \lambda_{d-PM}^2 + c} \; with \\ a &= L_d^2 - L_q^2 \\ b &= 2\lambda_{d-PM} L_d \\ c &= {\lambda_{d-PM}}^2 + L_q^2 I_{\max}^2 \end{aligned} \tag{2.17}$$

For fixed input voltage, speed and stator current, the value of I_d is calculated

2.3.2 Direct Flux Weakening Control

The direct flux weakening control operates the motor in the region defined by the base speed and above. There, the machine has reached the maximum voltage and the current space vector angle δ should be increased as the speed increases. The value of δ is selected such that it maximizes the output torque and keeps the motor in or below the voltage limit. It is clear that in this region equation 2.14 is not longer satisfied. By combining equations 2.1 -2.2 and neglecting the voltage drop in the resistor the maximum voltage in steady state can be written as:

$$\begin{aligned} V_{\max}^2 &= V_d^2 + V_q^2 \\ &= (\omega_e \lambda_q)^2 + (\omega_e \lambda_d)^2 \\ &= (\omega_e L_q I_q)^2 + \left(\omega_e \left(\lambda_{d-PM} + L_d I_d\right)\right)^2 \end{aligned} \tag{2.15}$$

in this region it is also required to produce the maximum torque available, then it is desirable to use the maximum current. The maximum voltage can be written as:

$$V_{\max}^2 = \omega_e^2 \left[L_q^2 \left(I_{\max}^2 - I_d^2 \right) + \left(\lambda_{d-PM} + L_d I_d \right)^2 \right] \tag{2.16}$$

in a compact form equation 2.14 is

$$\begin{aligned} V_{\max} &= \omega_e \sqrt{I_d^2 a + b I_d + \lambda_{d-PM}^2 + c} \; with \\ a &= L_d^2 - L_q^2 \\ b &= 2\lambda_{d-PM} L_d \\ c &= {\lambda_{d-PM}}^2 + L_q^2 I_{\max}^2 \end{aligned} \tag{2.17}$$

For fixed input voltage, speed and stator current, the value of I_d is calculated

from equation 2.17, and I_q is calculated by: $I_q = \sqrt{\left(I_{\text{max}}^2 - I_d^2\right)}$.

2.3.3 Machine Operation

The torque controller of the machine determines the current commands from the commanded torque, the machine speed and maximum voltage. The control methodology will be subdivided in two regions as stated before.

For speed below than the corner, the relation between I_s, δ and τ_e can be precalculated an use it to calculate the current commands. The stator current I_s is varied in fixed steeps from 0 to I_max; equation 2.14 is used to determine the corresponding angle δ for MTPA. For each set of I_s and δ, equation 2.6 is used to determine the torque produced by the machine. From this analysis the relation of I_s, δ and τ_e is determined, that is for a specific current value I_s , there is a corresponding set of δ and τ_e. A numerical inversion of the function $\tau_e(I_s)$ is used to determine the current command for a requested torque command τ_e. The value of δ is calculated by the relation established between it and I_s.

For the corner speed and beyond, the relation between I_d and ω_e is precalculated and used as a command independently of the motor torque. For defined values of maximum voltage, maximum current and machine speed the direct axis current component can be calculated from 2.17. The speed is varied from corner to maximum in fixed steeps; and for every speed value a correspondent I_d is calculated. I_d is used as command, and the stator current component I_q is changed in real time to produce the required torque, that is a PI controller will adjust I_q to produce the required torque or speed.

Chapter 3

Machine Modeling

3.1 Introduction

Applications of electric vehicles (EVs) require traction motors with high efficiency, high power density and extended field weakening capability. The Permanent Magnet Synchronous Motor (PMSM) has high efficiency and high power density. The Interior Permanent Magnet Synchronous Motor (IPMSM) has an extended field-weakening region due the additional torque obtained by the saliency; its accurate torque calculation is important to operate the machine efficiently and within its designed operational limits.

The developed torque in a PMSM has three components: permanent magnet, reluctance and cross-saturation. As seen earlier, the permanent magnet torque is due to the interaction between the flux produced by the rotor magnets and the stator current. The reluctance torque is produced by the interaction between the stator current and the reluctance change in the machine when the rotor moves. The cross saturation torque is the component that represents the change of the total torque due to the coupling between the direct and quadrature axis currents with their perpendicular fluxes caused by saturation. This cross saturation component becomes relevant

in high power density machines, where the simplified model presented in section 2.2 produce: significant error in the torque calculation, controller detuning and hence efficiency reduction.

The PMSM model presented here includes self inductances (L_d and L_q) and quasi-mutual inductances (M_{qd} and M_{dq}). The self-inductance, L_d, relates the change of direct axis flux linkages due to the change in the direct axis current, and L_q represents the same relation in the quadrature axis. The cross magnetization is modeled by the inclusion of two quasi-mutual inductances, M_{qd} and M_{dq}. M_{qd} models the change of quadrature axis flux due to change of the direct axis current and M_{dq} models the change of direct axis flux due to change in the quadrature axis current.

The generated torque in IPMSM is calculated from the estimated flux in the machine and directly from Finite Element Analysis (FEA). The torque calculated directly by FEA is not useful enough, because it does not allow us to determine the percentage of PM-torque, reluctance torque and cross magnetization torque, which are important to optimize the machine design. The torque computation from flux estimation using the 2-axis model presented in [1] does not include the saturation effect. To make an accurate estimation of the torque, it is necessary to consider the saturation and the consequent reduction of the flux in the machine [2, 3, 4, 5]. Additional considerations of the cross-magnetization effect include the dependence of the inductances on the currents as $L_d(i_d, i_q)$ and $L_q(i_d, i_q)$[6, 7, 8]. In [9, 10, 11] the inclusion of mutual inductances in the machine model was presented; [9, 10] assume that the direct and quadrature flux can be modeled by superposition, where L_d and M_{qd} depend only on i_d , and L_q and M_{dq} depend only on i_q.

There is a coupling between the direct and quadrature currents and their perpendicular fluxes due to cross magnetization and saturation. In [11] this effect is described and the methodology of a square wave voltage injection is applied to calculate self and mutual inductances, the inductances depend on the stator current components

as follows: $L_d(i_d, i_q)$, $L_q(i_d, i_q)$, $M_{dq}(i_d, i_q)$ and $M_{qd}(i_d, i_q)$. This methodology was validated by comparing simulated and experimentally calculated flux linkages, however, the main disadvantage is that the test has to be made at standstill neglecting entirely the dependance of the flux on the rotor position. Rahman *et al.* [12] proposed a methodology to calculate the flux linkages while the machine is operating at constant speed, however the results were not used for the inductances calculation.

The methodologies presented above for the model calculation vary from a constant parameter to a cross saturated model, however the methodologies could not validated experimentally or the models are not calculated under the normal operation of the machine.

This chapter describes the cross saturation effect and presents a methodology to calculate the self and mutual inductances using flux estimation. These inductances are used to calculate the voltage, torque and the field weakening profile of the machine. The proposed methodology was validated by FEA analisys and experiments. Four different machine configurations were simulated: Half Slot per Pole per Phase (HSPP), 1 Slot per Pole per Phase (SPP), 2 SPP and 4 SPP. The experimentally determined parameters of a prototype IPMSM with 2 SPP are presented.

3.2 Flux Linkages Calculation and Machine Modeling

The two axis model in the rotor frame of reference of a PMSM described by the flux, current, voltage and torque equations is summarized by equations 3.1 to 3.7.

$$\lambda_d = \lambda_{d-PM} + L_d i_d \tag{3.1}$$

$$\lambda_q = L_q i_q \tag{3.2}$$

$$v_d = R_s i_d - \omega_e \lambda_q + \frac{\partial \lambda_d}{\partial t} \tag{3.3}$$

$$v_q = R_s i_q + \omega_e \lambda_d + \frac{\partial \lambda_q}{\partial t} \tag{3.4}$$

$$\tau_m = \frac{3}{2}\frac{P}{2}\left(\lambda_{d-PM} i_q\right) \tag{3.5}$$

$$\tau_r = \frac{3}{2}\frac{P}{2}\left(\left(L_d - L_q\right) i_d i_q\right) \tag{3.6}$$

$$\tau_e = \tau_m + \tau_r \tag{3.7}$$

The model described above assumed constant inductances, that is not entirely true in high power density machines, where the saturation in the iron core produces that the flux in the machine changes nonlinearly with the stator currents. The machine is usually operated under saturation; therefore the flux is not linearly dependent on the currents, and hence the inductances are not constant.

The calculation of the stator flux linkages demonstrate the dependence of direct and quadrature axis fluxes on the stator currents; torque, voltage and inductances calculation are based on the calculated flux. The general procedure to calculate the stator flux linkages is described below.

3.2.1 Flux Linkages Calculation

The test proposed to calculate the flux linkages and the analysis are described in this section. This methodology is similar to [12], however some modifications have been made in order to obtain the machine voltage from experiments. The experimental calculation of the flux linkages requires the measurement or estimation of the induced voltage. One approach requires for example filter and then measure the voltage, then extract the first harmonic and correct it for the shift and amplitude reduction due to the filter [12]. The methodology proposed here uses the commanded voltage, a bandstop filter is used to remove the Pulse With Modulation (PWM) content of the power signal. The test used to calculate the flux linkages is presented below:

1. Connect the machine to a dynamometer operated in speed mode, that is the dynamometer will keep the speed value constant independently of the load.

2. Command zero stator current and measure/estimate the induced voltage in the stator.

3. Integrate the voltages with respect to time, and calculate the stator fluxes in the stator frame of reference. With the transformation matrix of equation 3.8 convert the stator fluxes from the stator to the rotor frame of reference. The direct and quadrature axis fluxes linkages calculated are λ_{d-PM} and λ_{q-PM}.

$$T(\theta_e) = \begin{pmatrix} \cos(\theta_e) & \cos(\theta_e + 2\pi/3) & \cos(\theta_e - 2\pi/3) \\ \sin(\theta_e) & \sin(\theta_e + 2\pi/3) & \sin(\theta_e - 2\pi/3) \\ 0.5 & 0.5 & 0.5 \end{pmatrix} \tag{3.8}$$

4. Command a rotating, fixed-magnitude current space vector aligned with the quadrature axis. Measure the induced voltage and subtract the drop of voltage in the resistance. Follow the procedure described above to calculate the total

flux in the direct and quadrature axis $\lambda_d(I_d, I_q)$ and $\lambda_q(I_d, I_q)$.

5. Repeat step 4, for magnitudes of the current space vector from 0.05 to 1 per unit (pu) and values of δ from 90^0 to 180^0 electrical degrees. This means a variation of the current space vector from the quadrature axis to the negative direct axis.

6. The flux linkages components due to stator current are given by:

$$\Delta\lambda_d(I_d, I_q) = \lambda_d(I_d, I_q) - \lambda_{d-PM} \tag{3.9}$$

$$\Delta\lambda_q(I_d, I_q) = \lambda_q(I_d, I_q) - \lambda_{q-PM} \tag{3.10}$$

Four machines with the same rotor and with different stator configurations were evaluated: HSPP, 1SPP, 2SPP and 4SPP, Figure 3.1. Figures 3.2-3.3 show the calculated $\Delta\lambda_d(i_d, i_q)$ and $\Delta\lambda_d(i_d, i_q)$. The calculated flux linkages components, direct and quadrature, depend on the direct and quadrature axis currents. Although, it is clear that the direct axis flux depends more on i_d and quadrature axis flux depends more on i_q, there exists a dependence of the fluxes on their perpendicular currents. This effect is called "cross saturation".

3.3 Cross Magnetization: Concept

Lets consider the interior permanent magnet synchronous motor with 4 SPP shown in Figure 3.4. This machine has 4 poles and sinusoidally distributed windings. The direct and quadrature axis of the machine are presented in Figure 3.4-a. The windings of phase "a" are distributed as shown in Figure 3.4-b. The equivalent flux linkages due to current in this phase are aligned in the direction described by the arrow. The same convention is used for phases "b" and "c" with a shift of 120^0 and 240^0 electrical

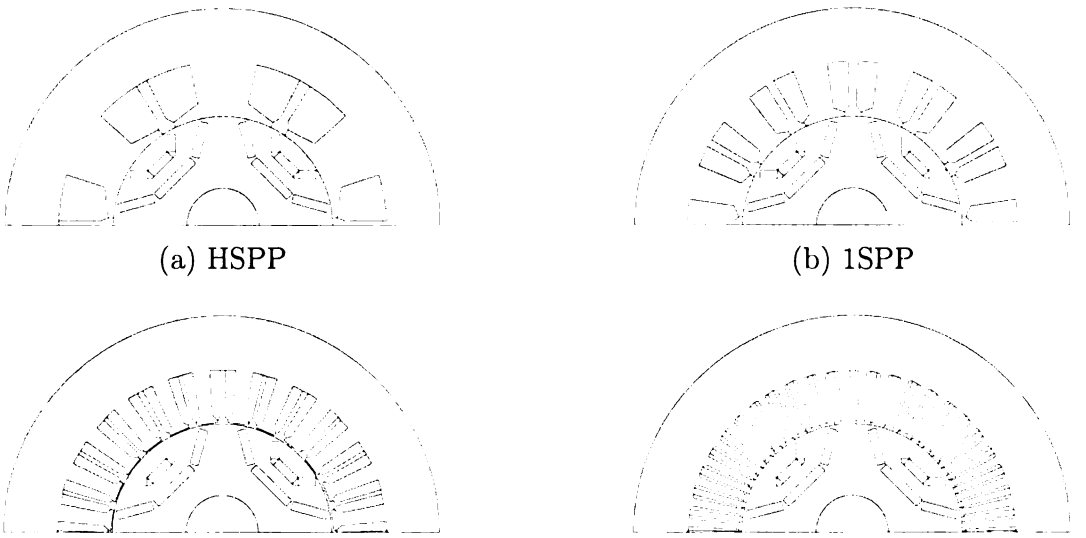

(a) HSPP (b) 1SPP

(c) 2SPP (d) 4SPP

Figure 3.1: Machine's stator configurations

degrees (60^0 and -60^0 mechanical degrees).

The flux linkages components in the stator are given by equation 3.11. In this equation, the stator flux linkages depends on the rotor position θe and on the projection of the flux linkages of each phase over the direct and quadrature axis.

$$\lambda = \lambda_d + j\lambda_q = e^{j\theta e}\left(\lambda_a + \lambda_b e^{j2\pi/3} + \lambda_c e^{j4\pi/3}\right) \tag{3.11}$$

Figure 3.5 shows the machine at rotor position of 90^0. With no stator current, the rotor flux only links the phases "b" and "c". The direct axis flux linkages consist of the sum of the projections of the flux linkages of phases "b" and "c". The quadrature axis flux linkages is zero because the projection of the flux linkages of phases "b" and "c" cancel each other. When the rotor position changes, the direct and quadrature flux linkages components of each phase change, however, the stator flux linkages have only a direct axis component and their magnitude remains almost constant.

Now let us consider a machine with stator saliency like the machine with HSPP whose stator and rotor are shown in Figure 3.6.

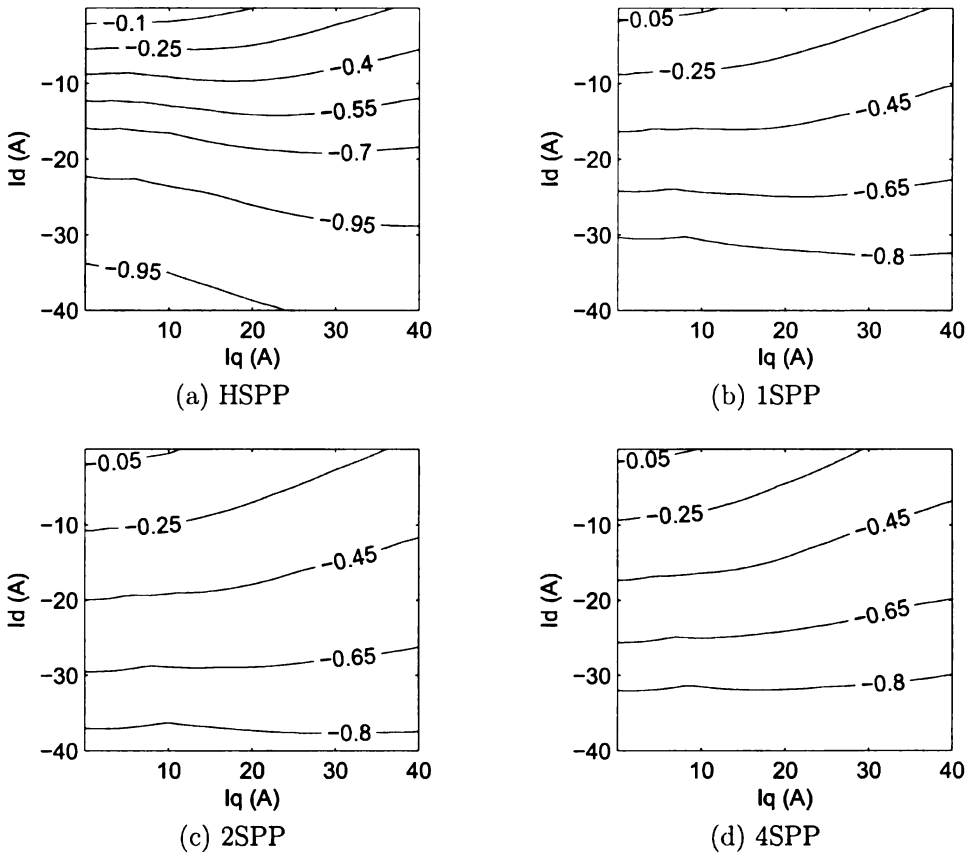

(a) HSPP (b) 1SPP

(c) 2SPP (d) 4SPP

Figure 3.2: Direct axis flux $\Delta\lambda_d(i_d, i_q)$

Figure 3.7 a-b shows the machine and the equivalent flux diagram at a rotor position of 90^0, with no stator currents. The stator flux linkages have only direct axis components. When the rotor moves, Figure 3.7 c-d, the stator slots modify the shape the rotor flux linkages, creating a quadrature flux linkages component oscillatory with the rotor position, however, its average over one revolution is zero. In a similar way, when the rotor moves, the direct axis flux linkages change, but its average over one revolution is similar to the value at $\theta_e = 0^0$.

A similar analysis can be done when a stator current is applied. Let us consider the case when the current space vector is aligned with the quadrature axis, at rotor

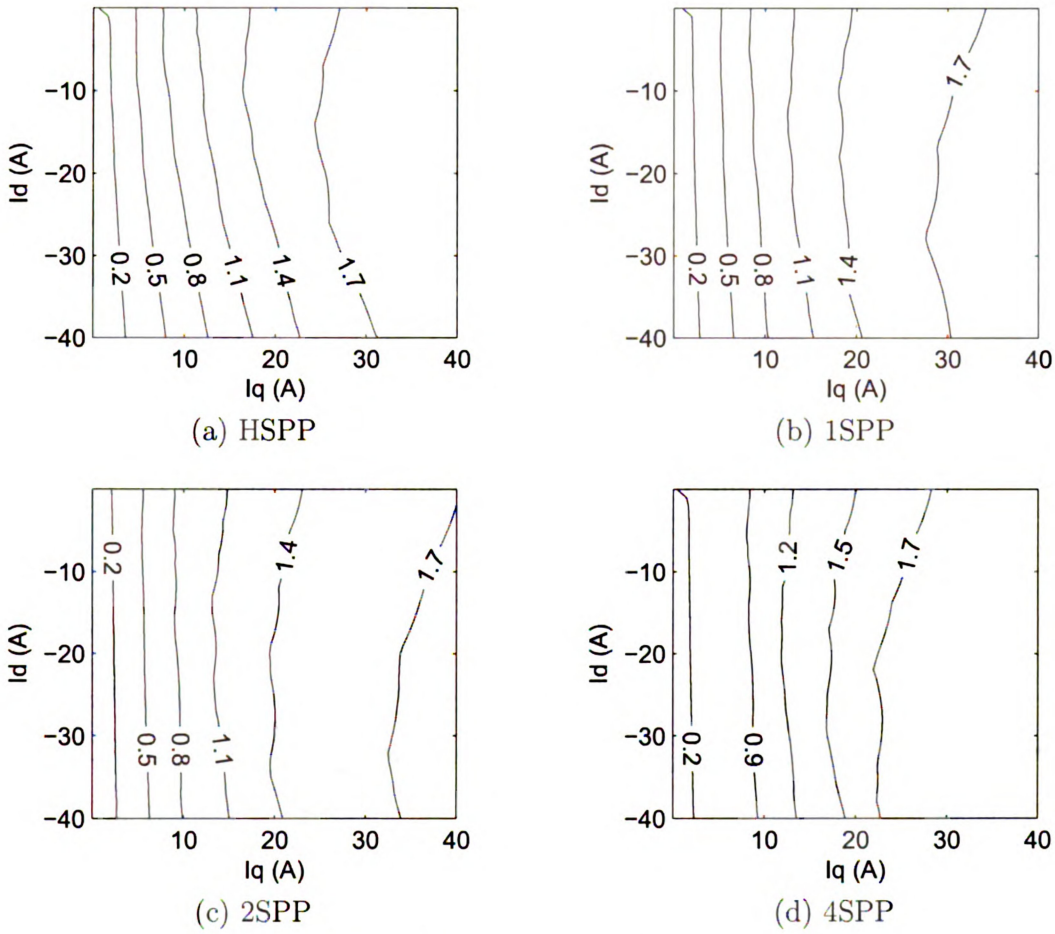

(a) HSPP (b) 1SPP

(c) 2SPP (d) 4SPP

Figure 3.3: Quadrature axis flux $\Delta\lambda_q(i_d, i_q)$

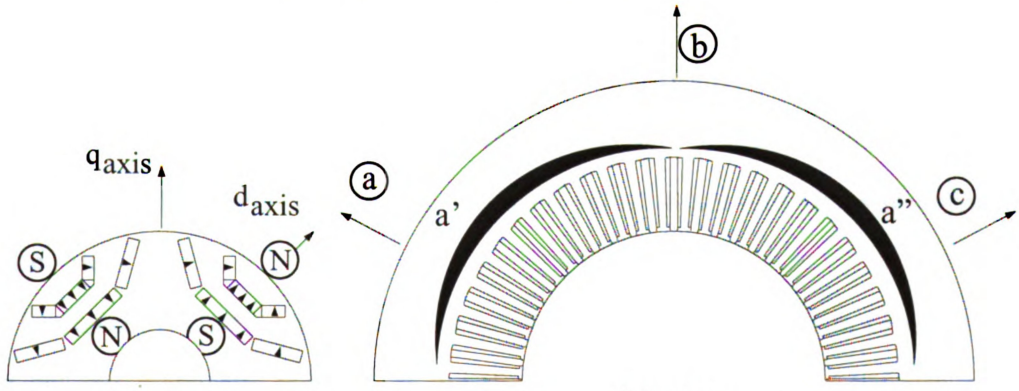

(a) rotor (b) stator

Figure 3.4: IPMSM with 4SPP and with sinusoidally distributed windings

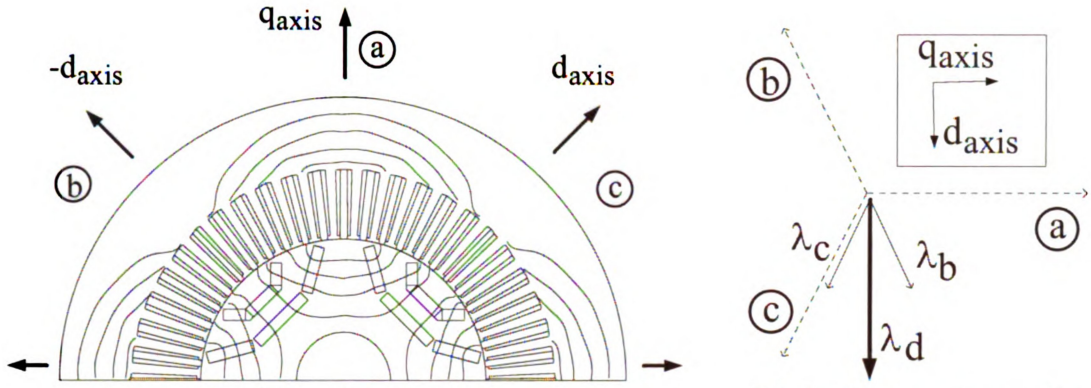

(a) Flux distribution

(b) Equivalent phasor diagram

Figure 3.5: Rotor flux linkages for a 4SPP machine $\theta_e = 90^0$

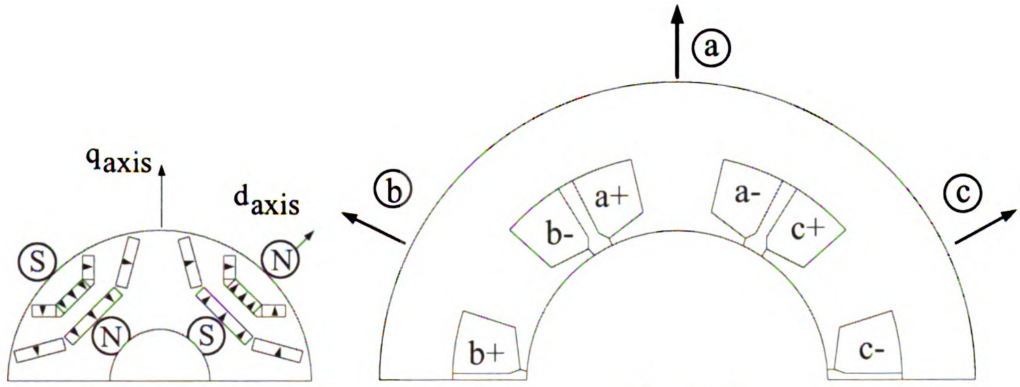

(a) rotor

(b) stator

Figure 3.6: IPMSM with HSPP and with concentrated windings

position of 90^0, as shown in Figure 3.8-a. Under no saturation, the stator flux linkages are equal to the sum of the flux linkages due to the rotor magnets and the quadrature axis current. However, when the saturation is taken in account this statement is no longer true.

To explain the saturation effect, let us calculate the flux density in two points "m" and "n" symmetrically located around the quadrature axis. The rotor flux linkages define the operation point of the machine, then, with no stator currents, the points "m" and "n" have the same flux density 3.8-b. When the quadrature axis stator current is applied, the flux linkages due to the current add to the rotor flux linkages

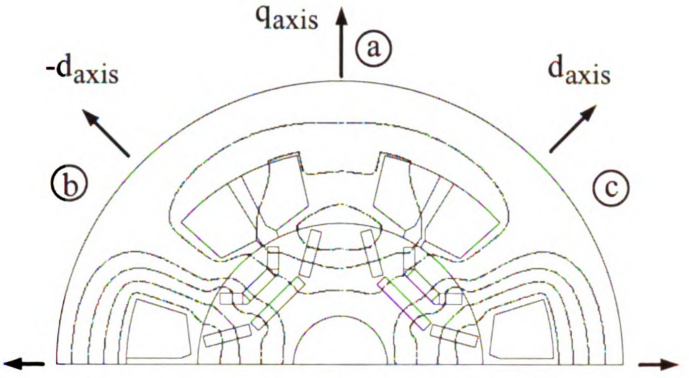

(a) Flux distribution $\theta_e = 90^0$

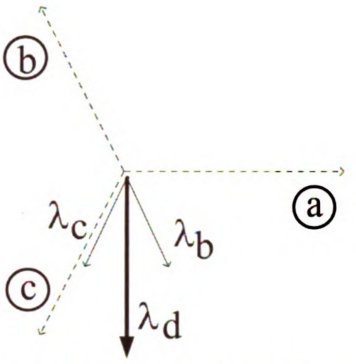

(b) Equivalent phasor diagram $\theta_e = 90^0$

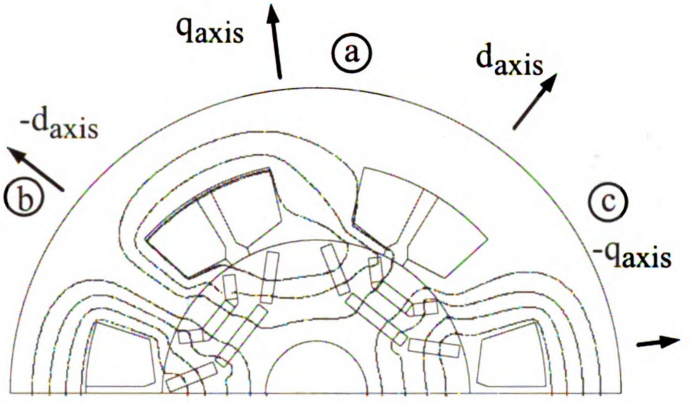

(c) Flux distribution $\theta_e = 75^0$

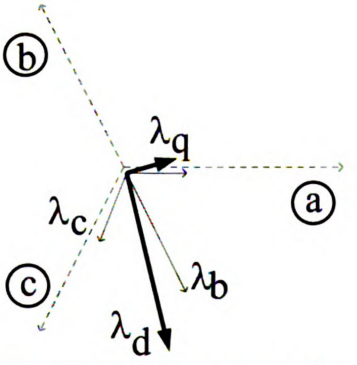

(d) Equivalent phasor diagram $\theta_e = 75^0$

Figure 3.7: Rotor flux linkages for a HSPP machine $\theta_e = 90^0$ and $\theta_e = 75^0$

in the point "n" and subtract in the point "m" as shown in Figure 3.8-c. Under saturation, the flux density in "n" is lower than the linear sum of the rotor flux linkages and the stator flux linkages due to the stator currents; the flux density in "m" is more than the difference of these fluxes because the flux moves away from saturation.

The previous analysis can be used to determine the total flux linkages at the same rotor position. The rotor flux linkages and the flux linkages due the stator currents are added in the tooth of phase "b" (like in the point n), this means that under

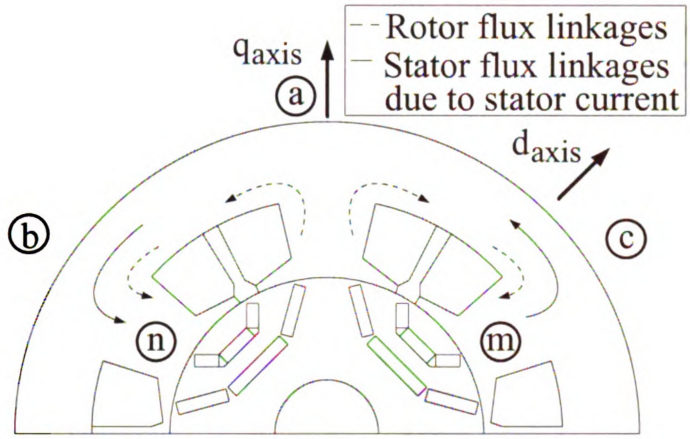

(a) Flux distribution

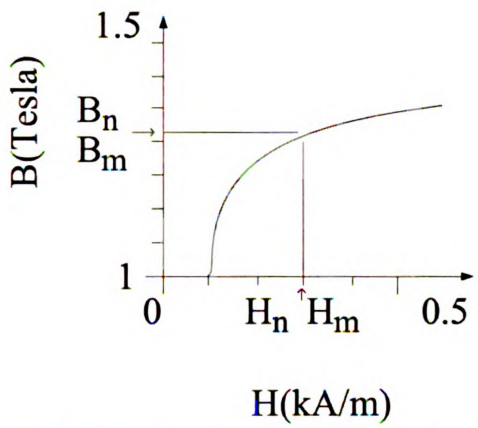

(b) Rotor flux linkages in m and n

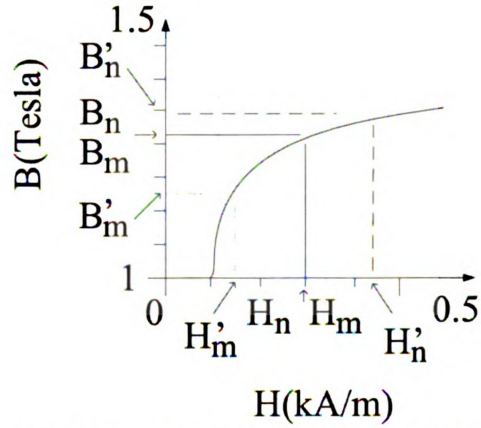

(c) Stator flux linkages in m and n

Figure 3.8: Stator flux linkages for HSPP machine $\theta_e = 90^0$

saturation the total flux linkages are lower than the linear sum. In the tooth of phase "c" (like in the point m), the total flux linkages is the difference between the rotor flux linkages and the flux linkages due the stator currents. At this rotor position the direct axis component of the flux is lower than the rotor flux linkages, and the quadrature axis flux linkages is lower that the flux due to the stator currents as shown in Figure 3.9-c.

When the rotor moves, the saturation and the saliency produce pulsation in the stator flux linkages as shown in Figure 3.10. The saturation produces a decrease in the stator flux linkages as shown in Figures 3.10 a-b. This analysis shows how the direct

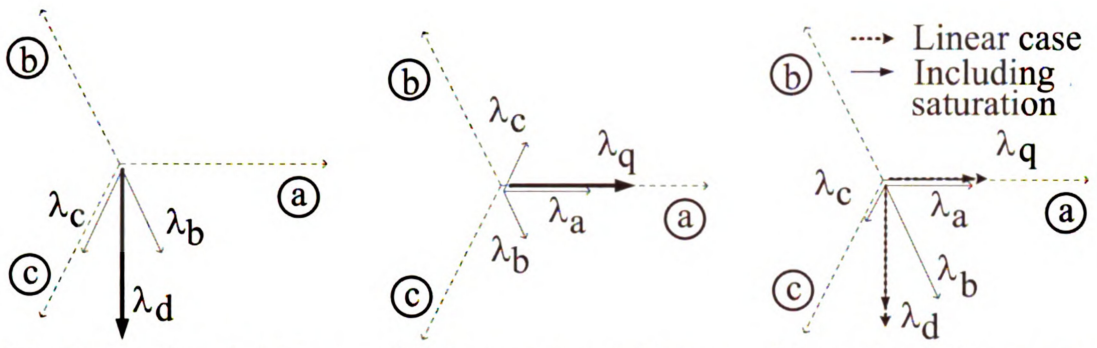

(a) Stator flux linkages due to PM

(b) Stator flux linkages due to stator current

(c) Total flux linkages in the stator

Figure 3.9: Space vector diagram of flux linkages

axis current produces a decrement in the rotor linkages flux. Permanent axis flux and quadrature axis current component are orthogonal one to each other, then exist cross-magnetization. In a general case the saturation level of the machine depends nonlinearly with the stator currents. Then the cross magnetization effect depends nonlinearly on the direct and quadrature axis components of the stator currents.

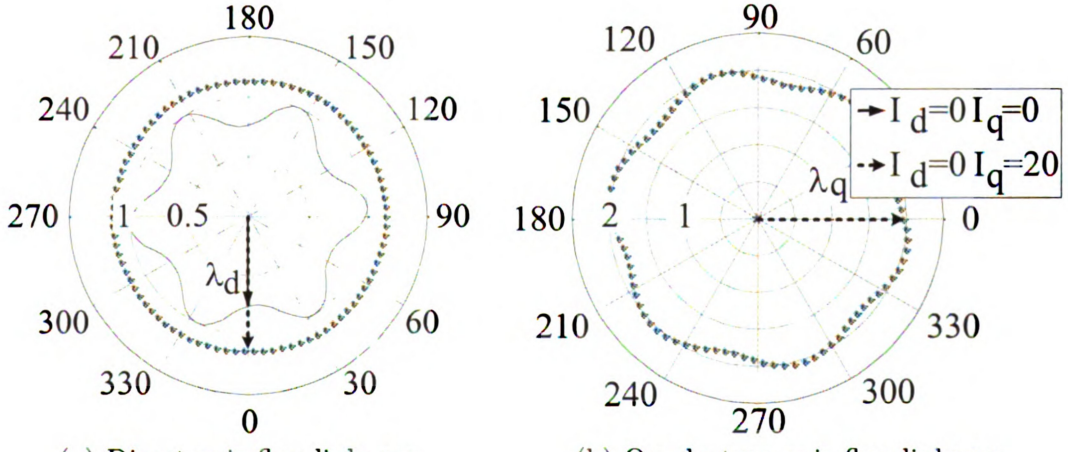

(a) Direct axis flux linkages

(b) Quadrature axis flux linkages

Figure 3.10: Stator flux linkages as function of θ_e

3.4 Cross Magnetization: Machine Model and Calculation

The 2-axis model presented in section 3.2 does not include the cross-magnetization effect. Figure 3.2 shows that $\Delta\lambda_d$ changes with i_q and $\Delta\lambda_q$ with i_d, Figure 3.3. The model that includes the dependence of the flux linkages on i_d and i_q is presented below, and the methodology to calculate the parameters is explained and applied to the machines presented in section 3.3 .

3.4.1 Machine Model

A more detailed model that includes cross-magnetization was presented in [9, 10]. This model includes mutual inductances in the flux, voltage and torque equation as follows:

$$\lambda_d = \lambda_{d-PM} + L_d i_d + M_{dq} i_q \tag{3.12}$$

$$\lambda_q = \lambda_{q-PM} + L_q i_q + M_{qd} i_d \tag{3.13}$$

$$v_d = R_s i_d - \omega_e \lambda_q + \frac{\partial \lambda_d}{\partial t} \tag{3.14}$$

$$v_q = R_s i_q + \omega_e \lambda_d + \frac{\partial \lambda_q}{\partial t} \tag{3.15}$$

$$v_s^2 = v_d^2 + v_q^2 \tag{3.16}$$

$$\tau_m = \frac{3}{2}\frac{P}{2}\left(\lambda_{d-PM} i_q - \lambda_{q-PM} i_d\right) \tag{3.17}$$

$$\tau_r = \frac{3}{2}\frac{P}{2}\left(\left(L_d - L_q\right) i_d i_q\right) \tag{3.18}$$

$$\tau_c = \frac{3}{2}\frac{P}{2}\left(-M_{qd} i_d^2 + M_{dq} i_q^2\right) \tag{3.19}$$

$$\tau = \tau_m + \tau_r + \tau_c \tag{3.20}$$

This model includes the dependence of λ_d on i_q by including the quasi-mutual inductance M_{dq}; in the same manner, it includes the dependence of λ_q on i_d by the mutual inductance M_{qd} . An additional torque component τ_c is produced due to cross saturation, which is dependant on the currents and the mutual inductances.

3.4.2 Model Calculation

The model parameters are stator resistance, rotor flux linkages, self inductances and mutual inductances. The resistance can be measured and its value will be considered constant for the whole operation of the machine. The rotor flux linkages will be assumed constant with a value equal to the flux linkages when the stator currents are zero; any change in the stator flux linkages will be taken in account by the inductances. Theses inductances are calculated as the ratios of the flux linkages $\Delta\lambda$ due to stator currents and the stator currents components that produces the flux. Let us consider two particular cases:

1. The stator current only has direct axis component. The inductances L_d, M_{qd} can be calculated as follows:

$$L_d(I_d, 0) = \frac{\lambda_d(I_d, 0) - \lambda_{d-PM}}{I_d} \tag{3.21}$$

$$M_{qd}(I_d, 0) = \frac{\lambda_q(I_d, 0) - \lambda_{q-PM}}{I_d} \tag{3.22}$$

2. The stator current only has quadrature axis component. The inductances L_q, M_{dq} can be calculated as follows:

$$L_q(0, I_q) = \frac{\lambda_q(0, I_q) - \lambda_{q-PM}}{I_q} \tag{3.23}$$

$$M_{dq}(0, I_q) = \frac{\lambda_d(0, I_q) - \lambda_{d-PM}}{I_q} \tag{3.24}$$

The calculated self and mutual inductances are presented in Figures 3.11 and 3.12.

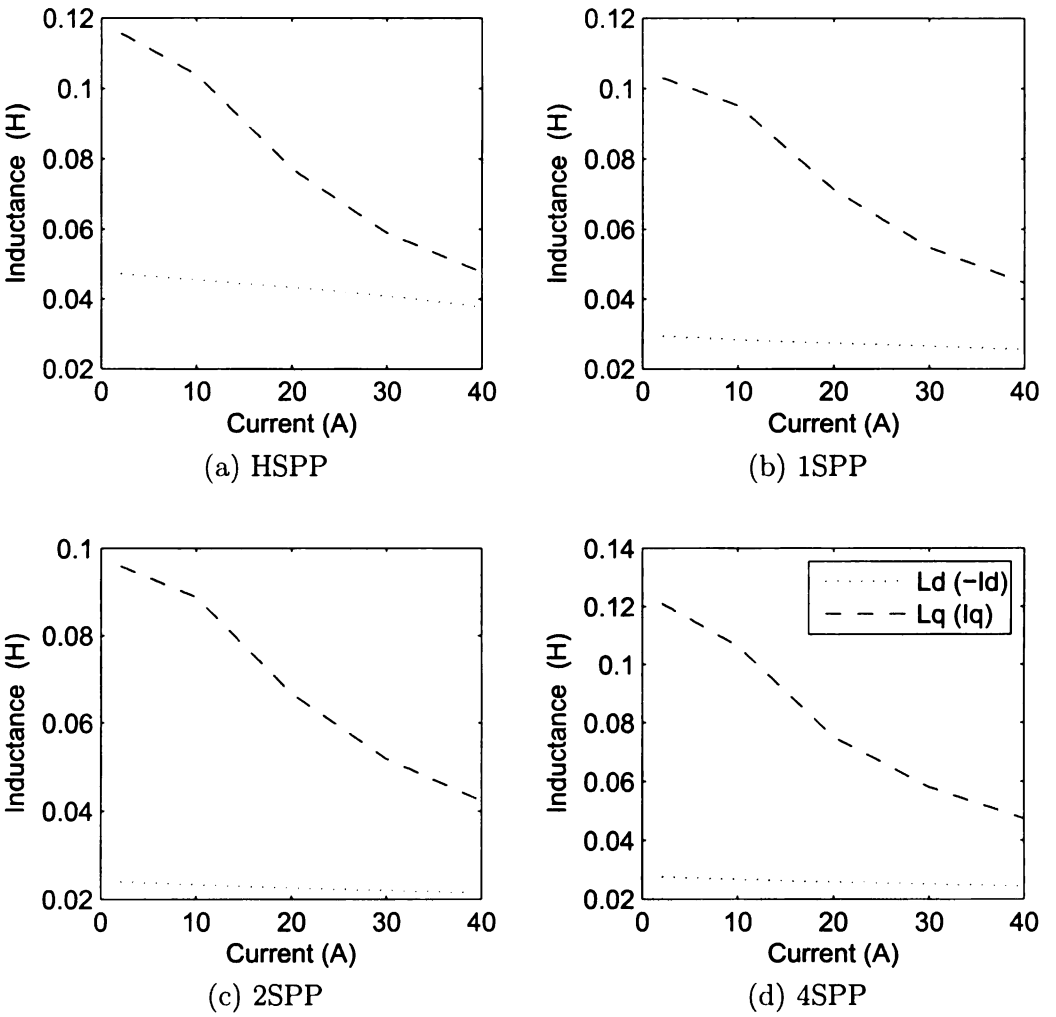

(a) HSPP (b) 1SPP

(c) 2SPP (d) 4SPP

Figure 3.11: Self inductances L_d and L_q

These figures show that the inductances L_d and M_{qd} are almost independent of I_d, and L_q, M_{dq} change considerably with I_q. The basic approach to calculate the machine parameters with cross-magnetization is to include the dependence of self and mutual inductances on both I_d and I_q . However, to calculate the inductances we have two equations (3.12,3.13) and four unknowns (L_d, L_q, M_{dq} and M_{qd}), hence

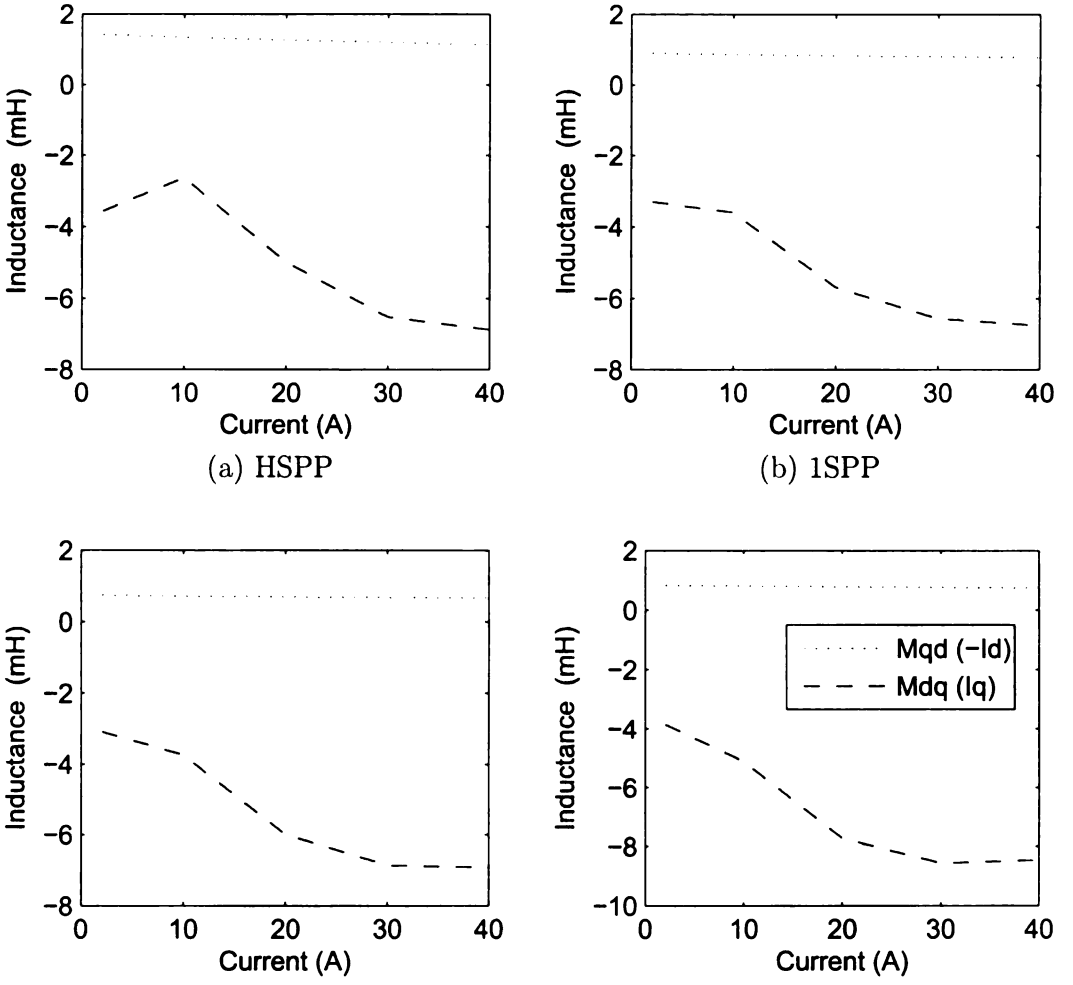

(a) HSPP (b) 1SPP

(c) 2SPP (d) 4SPP

Figure 3.12: Mutual inductances M_{qd} and M_{dq}

it is necessary to make some simplifications. The previous results show that L_d remains almost independent of currents (it changes about 5% for 1SPP, 2SPP and 4SPP and 21% for HSPP) and the inductance M_{qd} is the smallest compared with other inductances and it is almost independent of I_d. Then, the dependence of these parameters on I_q should be small. The assumptions proposed here are to consider that L_d and M_{qd} are independent of I_q, and the flux components due to these inductances are equal to the product of them with I_d. Any additional change in the stator flux linkages will be included by considering that L_q and M_{dq} are functions of both I_d

and I_q. The procedure used to calculate the inductances is described below:

1. Calculate the flux linkages following the procedure described in section 3.2.

2. Calculate $L_d(I_d, 0)$ and $M_{dq}(I_d, 0)$ by using equations (3.21) and (3.22) .

3. Calculate $L_q(I_d, I_q)$ and $M_{dq}(I_d, I_q)$ from equations (3.25) and(3.26).

$$L_q(I_q, I_q) = \frac{\lambda_q(I_d, I_q) - \lambda_{q-PM} - M_{qd}(I_d, 0)I_d}{I_q} \tag{3.25}$$

$$M_{dq}(I_d, I_q) = \frac{\lambda_d(I_d, I_q) - \lambda_{d-PM} - L_d(I_d, 0)I_d}{I_q} \tag{3.26}$$

The procedure described above was used to calculate the inductances of the machines analyzed. TL_d and M_{qd} are the same as shown in Figures 3.11-3.12 and L_q and M_{dq} with cross magnetization are shown in Figures 3.13-3.14.

To determine the accuracy of the proposed methodology and the improvements in the flux and torque calculation over the classical 2-axis model, the torque as function of the angle of the current space vector is calculated. The cases analyzed are:

1. Classical 2-axis model of equations (3.1-3.7), and include the saturation effect: $L_d(I_d, 0)$, $L_q(0, I_q)$, $M_{dq} = 0$ and $M_{qd} = 0$.

2. Cross-magnetization model of equations (3.12-3.20), include the saturation effect of each inductance but not the dependence of them on both currents I_d and I_q: $L_d(I_d, 0)$, $L_q(0, I_q)$, $M_{dq}(0, I_q)$ and $M_{qd}(I_d, 0)$.

3. Use the cross-magnetization model of equations (3.12-3.20), and include the saturation effect of each inductance and the dependence of them on both currents I_d and I_q: $L_d(I_d, 0)$, $L_q(I_d, I_q)$, $M_{dq}(I_d, I_q)$ and $M_{qd}(I_d, 0)$.

4. The FEA model; the torque is calculated directly from FEA.

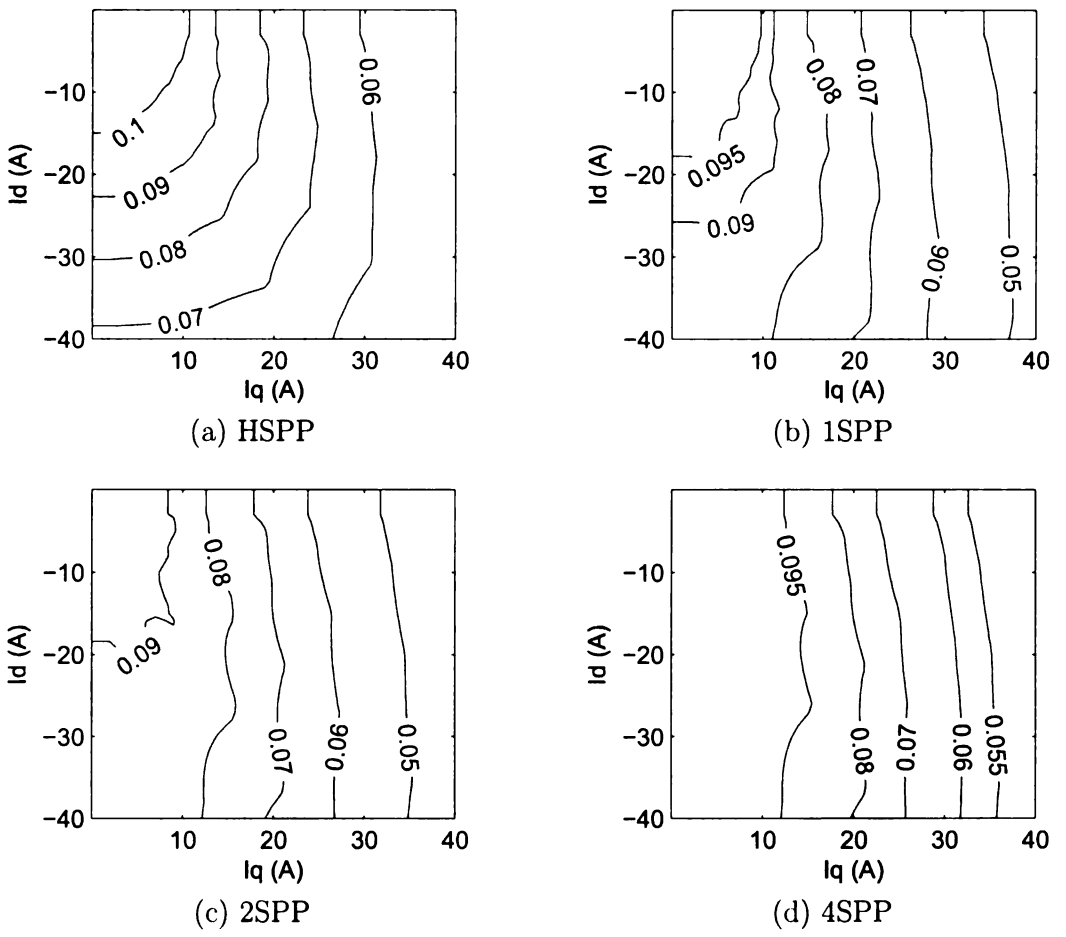

(a) HSPP (b) 1SPP

(c) 2SPP (d) 4SPP

Figure 3.13: Self Inductance calculation $Lq(i_d, iq)$

The cases described above were used to calculate the total torque Figure 3.15. This figure shows the calculated torque as a function of the current space vector angle. The most accurate torque calculation is the one produced by FEA analysis, and the torque error is calculated with respect to the value of FEA. The model presented in the numeral 1 has an error of about 15% for a current space vector angle of 90^0. The model described in the numeral 2 has an error of 15% at maximum torque, while the proposed model in item 4 has a maximum error less than 2%.

The torque calculation shows the accuracy of the methodology to determine the model parameters. After validating the results it is possible to accurately decompose

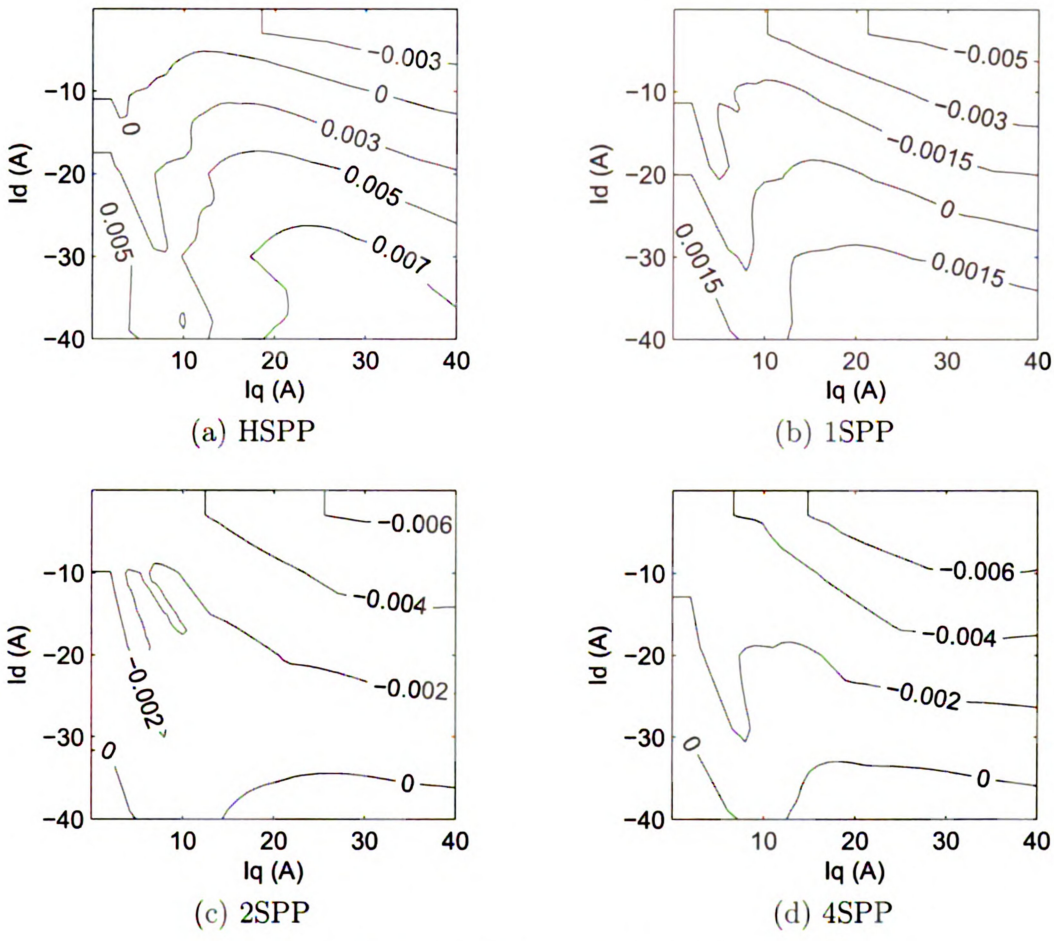

(a) HSPP (b) 1SPP

(c) 2SPP (d) 4SPP

Figure 3.14: Mutual Inductance calculation $M_{dq}(i_d, i_q)$

this torque in: PM torque, reluctance and cross magnetization. This decomposition gives the tool to redesign and optimize the machine according to the requirements.

Figure 3.16 shows that different stators can achieve different torque components. For example with 4SPP it is possible to achieve more PM torque and reluctance torque, however due to the cross magnetization the total torque is reduced. For the configuration of HSPP, the reluctance torque is the smallest, however the total torque is not negligible compared with the other stator configurations.

Finally, after selecting the maximum voltage of the power supply the field weakening profile is calculated. Figure 3.17 presents the field weakening curves for maximum

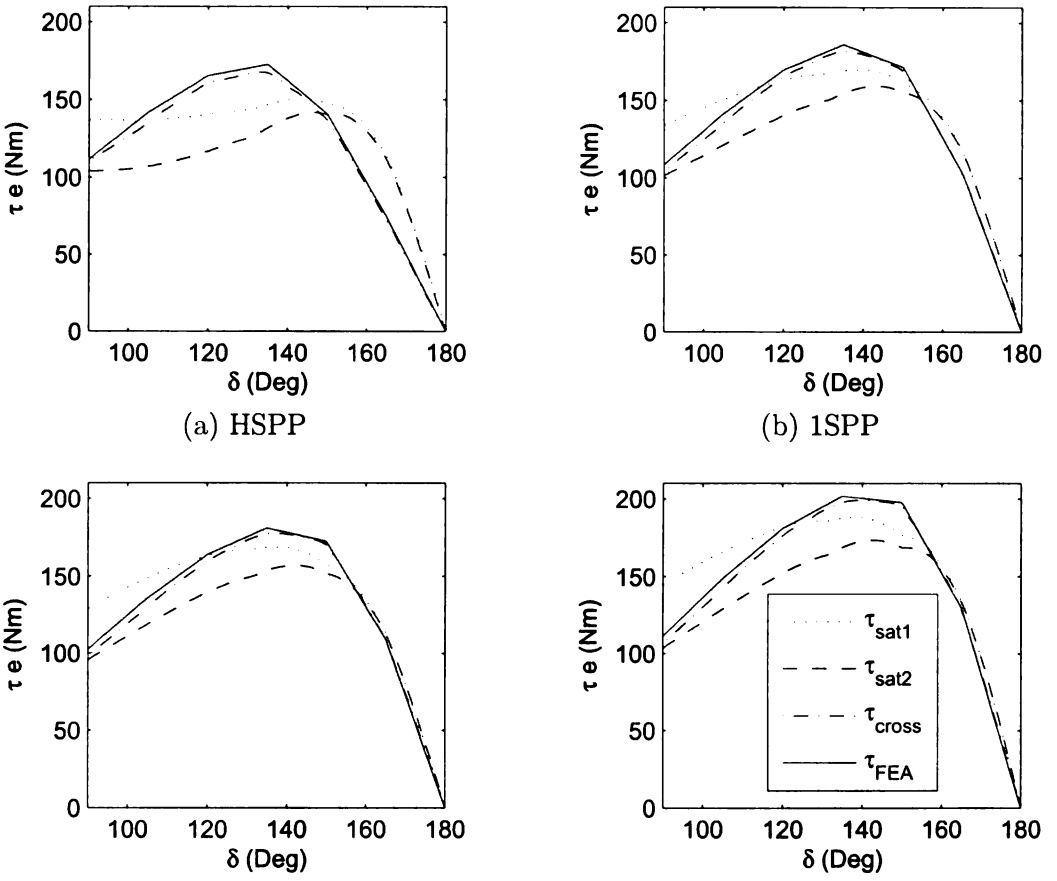

(a) HSPP (b) 1SPP

(c) 2SPP (d) 4SPP

Figure 3.15: Torque calculation including cross saturation

torque per ampere; it shows that although the configuration of 4 SPP has the highest maximum torque it has lower field weakening range and lower maximum speed compared with 1SPP and 2SPP. Although the configuration of HSPP has the maximum inductance L_d and hence more capability to weaken the rotor flux linkages, the field weakening range is limited because it has the lower maximum torque.

3.4.3 Experimental Model Calculation

The cross saturated model parameters were calculated for an IPMSM with the procedure described in the previous sections. The experimental setup is shown and

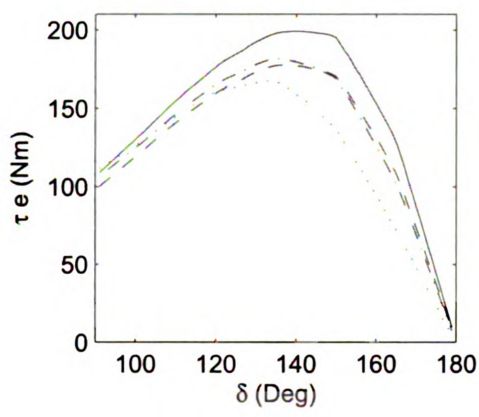

(a) Total Torque

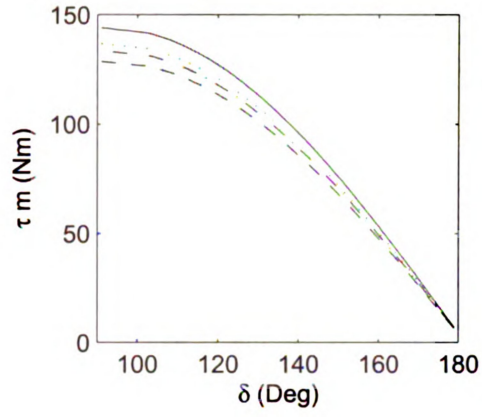

(b) PM torque

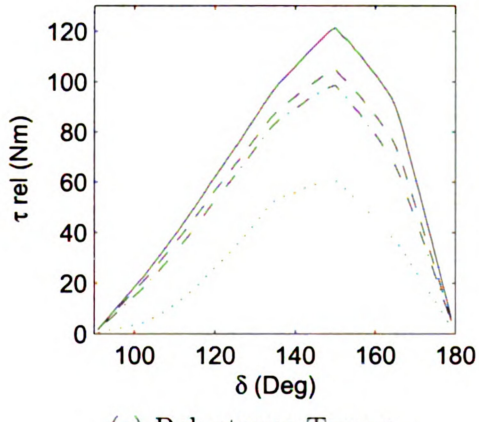

(c) Reluctance Torque

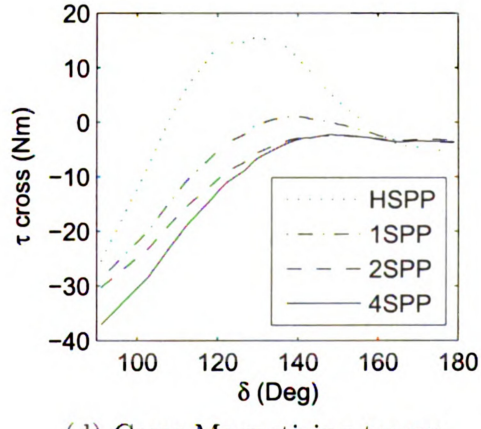

(d) Cross Magnetizing torque

Figure 3.16: Torque components calculation

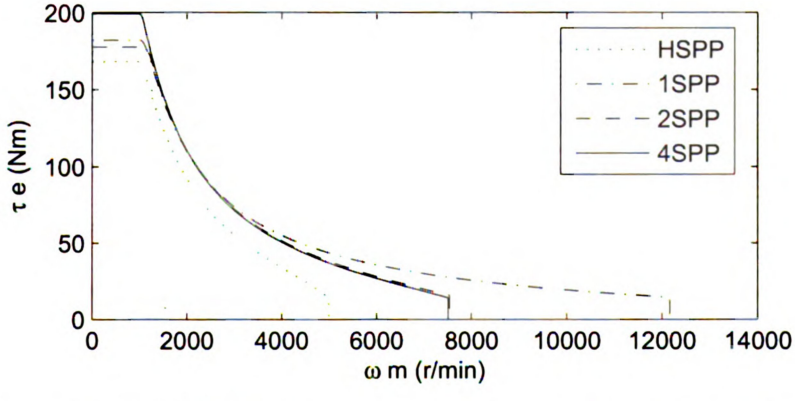

Figure 3.17: Field weakening curve for the configurations analyzed

described in Apendix A, for reference, the schematic of the experimental setup is shown in Figure 3.18. Experimental calculation of the flux linkages requires the measurement or estimation of the induced voltage.

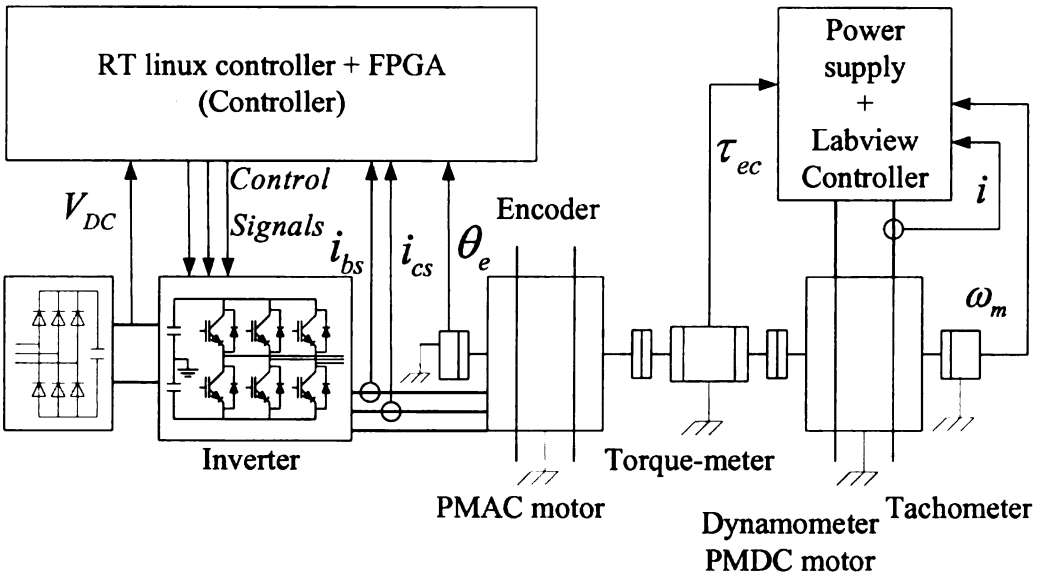

Figure 3.18: Schematic of the experimental setup

The initial approach was to consider that the commanded voltage is equal to the machine's terminal voltages. This commanded voltages were used calculate the flux linkages as shown in Figure 3.19. Figure 3.19-a shows a significant dependence of λ_d on i_q. In Figure 3.19-b it is shown that λ_q changes with i_d when $i_q = 0A$, which can not be explained by the cross saturation model.

The second approach uses the procedure described in [12], where a low pass filter and a data acquisition system sampling with a sampling frequency of 10 times the switching frequency where used to record the voltage signals. The calculated flux linkages using this method are shown in Figure 3.20.

The results of Figure 3.19 and Figure 3.20 have significant difference caused by the dead time, that is, the commanded voltage is different to the filtered-measured voltage. Let us consider the three phase inverter presented in Figure . To determine

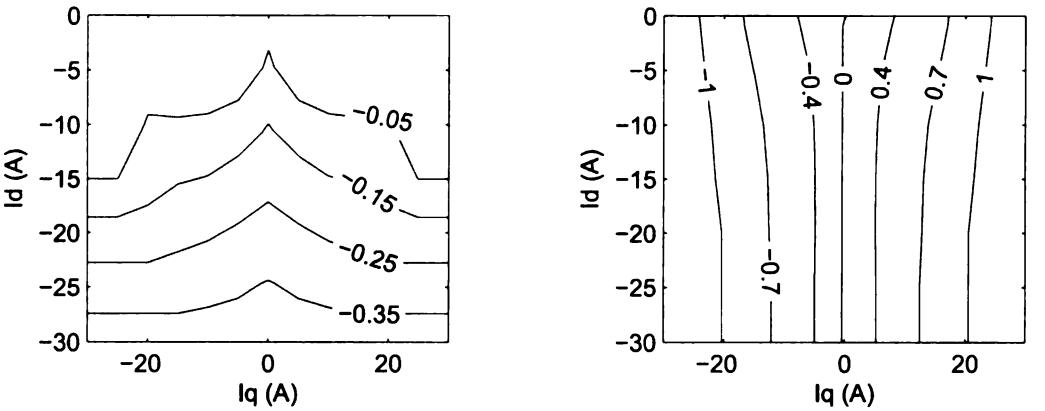

(a) $\Delta\lambda_d$ (b) $\Delta\lambda_q$

Figure 3.19: Calculated experimental Flux linkages using V^*

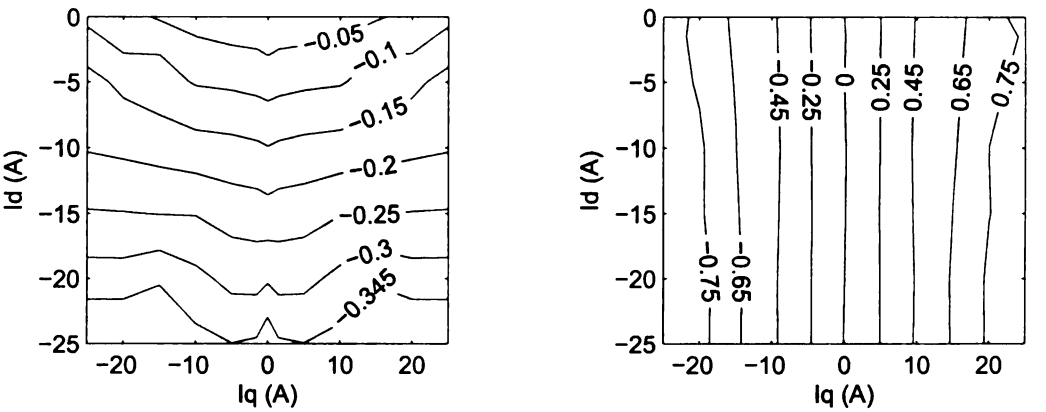

(a) $\Delta\lambda_d$ (b) $\Delta\lambda_q$

Figure 3.20: Calculated experimental Flux linkages using V_{mes}

the dead time effect in the machine voltage, the voltage in one phase leg is analyzed, Figure -b. The ideal switching commands are shown in Figure -a. The ideal pulses need to be modified to provide dead time to avoid a short circuit in the phase leg, Figure -b. During the dead time, the phase voltage is not zero, because due to the current, the diodes conduct during this time connecting the phase terminal either to $Vdc/2$ or to $-Vdc/2$. By neglecting the on time and off time of the switches and diodes it is possible to determine the increment or decrement in the phase voltage, Figures -c and -d.

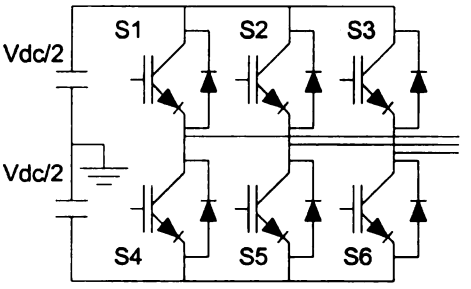

(a) Three phase inverter configuration

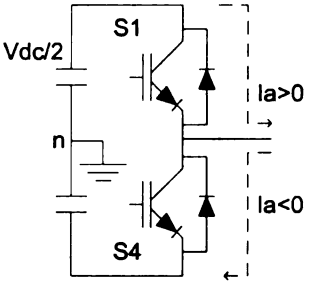

(b) Configuration of one phase leg

Figure 3.21: Three phase Inverter

The increment the three phases voltages due to the three phase currets is calculated as follows:

$$\begin{aligned}
\Delta v_a &= -\frac{T_d}{T_{sw}}\frac{V_{DC}}{3}\left[2sign(i_a) - sign(i_b) - 2sign(i_c)\right] \\
\Delta v_b &= -\frac{T_d}{T_{sw}}\frac{V_{DC}}{3}\left[2sign(i_b) - sign(i_a) - 2sign(i_c)\right] \\
\Delta v_c &= -\frac{T_d}{T_{sw}}\frac{V_{DC}}{3}\left[2sign(i_c) - sign(i_a) - 2sign(i_b)\right]
\end{aligned} \tag{3.27}$$

where T_{sw} is the period associated to the switching frequency and T_d is the dead time and V_{dc} is the DC-link voltage. v_a^* , v_b^* and v_c^* are the commanded voltages. These differences produces that the commanded voltage differ from the machine terminal voltages. Dead time compensation were used to reduce the error difference between both commanded and measured voltages. Several approaches have been proposed to compensate for dead time [13, 14, 15], where dead time, on-time off-time of the power

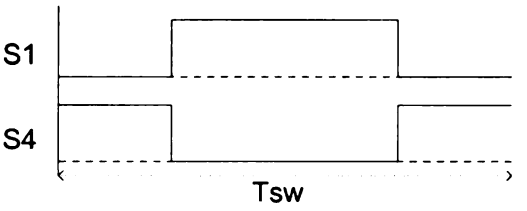

(a) Ideal

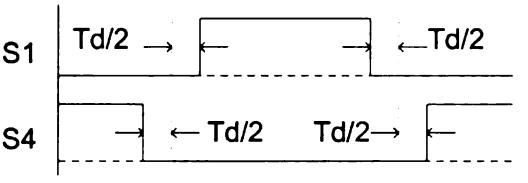

(b) With dead time

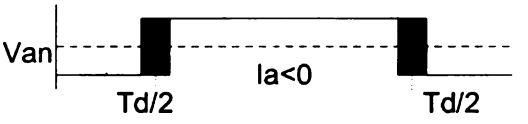

(c) Van for $ia > 0$

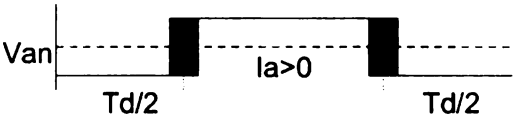

(d) Van for $ia < 0$

Figure 3.22: Switching pattern and actual voltage in the machine

devices and their associated drop-off voltage where included to corrected to for this effect.

A simple approach is used here to correct for dead time. The drop of voltage in the power electronics devices and the associated on and off times were neglected. The commanded voltages were corrected as follows:

$$\begin{aligned} v_{a-INV} &= v_a^* + \frac{T_d}{2T_{sw}}\frac{V_{DC}}{3}\left[2sign(i_a) - sign(i_b) - 2sign(i_c)\right] \\ v_{b-INV} &= v_b^* + \frac{T_d}{2T_{sw}}\frac{V_{DC}}{3}\left[2sign(i_b) - sign(i_a) - 2sign(i_c)\right] \\ v_{c-INV} &= v_c^* + \frac{T_d}{2T_{sw}}\frac{V_{DC}}{3}\left[2sign(i_c) - sign(i_a) - 2sign(i_b)\right] \end{aligned} \tag{3.28}$$

where v_{a-INV}, v_{b-INV} and v_{b-INV} are the voltage used to calculate the switching times in the inverters. v_a^* , v_b^* and v_c^* are the output voltages of the PI current controllers that are used to calculate the flux linkages. The calculated flux linkages with dead time compensation are presented in Figure 3.23.

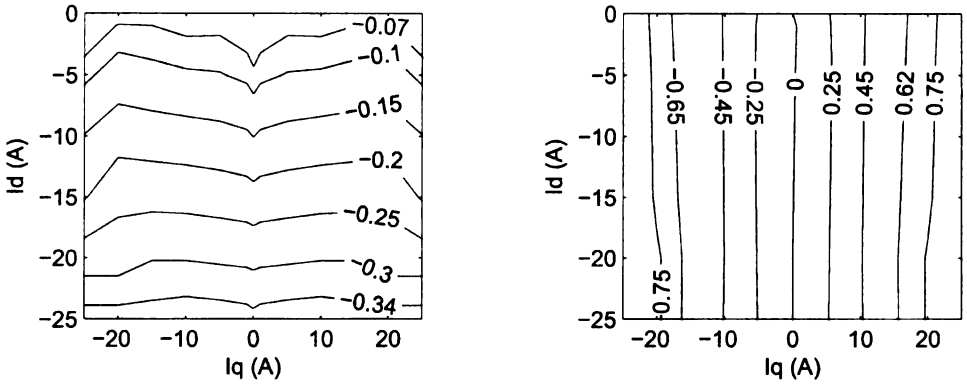

(a) $\Delta\lambda_d$ (b) $\Delta\lambda_q$

Figure 3.23: Calculated Flux linkages using V^* and dead time compensation

A better agreement was obtained between the calculated flux linkages of Figure 3.20 and Figure 3.23. Phase voltages where compared and the maximum error is less than 5% and the maximum phase shift was about 3 electrical degrees. The previous analysis verified the accuracy of the proposed approach for dead time compensation. The flux linkages shows the effect of cross saturation, where, the direct axis flux linkages changes with the quadrature axis current. Taking into account the cross saturation effect and dead time compensation, the parameters calculated for an IPMSM prototype are shown in Figures 3.24.

In addition to the cross saturated model complexity, the iron losses were included in the torque equation by subtracting a torque component due to the iron loss from the electrical torque. This component is proportional to the speed with a slope of k_{i-loss} as described By Senjyu *et* al. [16], however, the dependence of the iron losses on the stator current was neglected here. The iron loss coefficient of the motor

is $k_{i-loss} = 0.0013\ Nms$. The remaining parameters of the motor drive are presented in Table 3.1.

Table 3.1: Machine parameters

Parameter	Value	Units
Number of pole pairs	2	
Stator resistance	0.4	Ω
Rotor flux linkages	.4652	Wb
Rated peak voltage per phase	120	V
Rated peak current	20	A
Rotor inertia J_m	0.1938	kgm^2
Viscous friction coefficient B_m	0.0043	Nms
Iron loss coefficient k_{i-loss}	0.0013	Nms

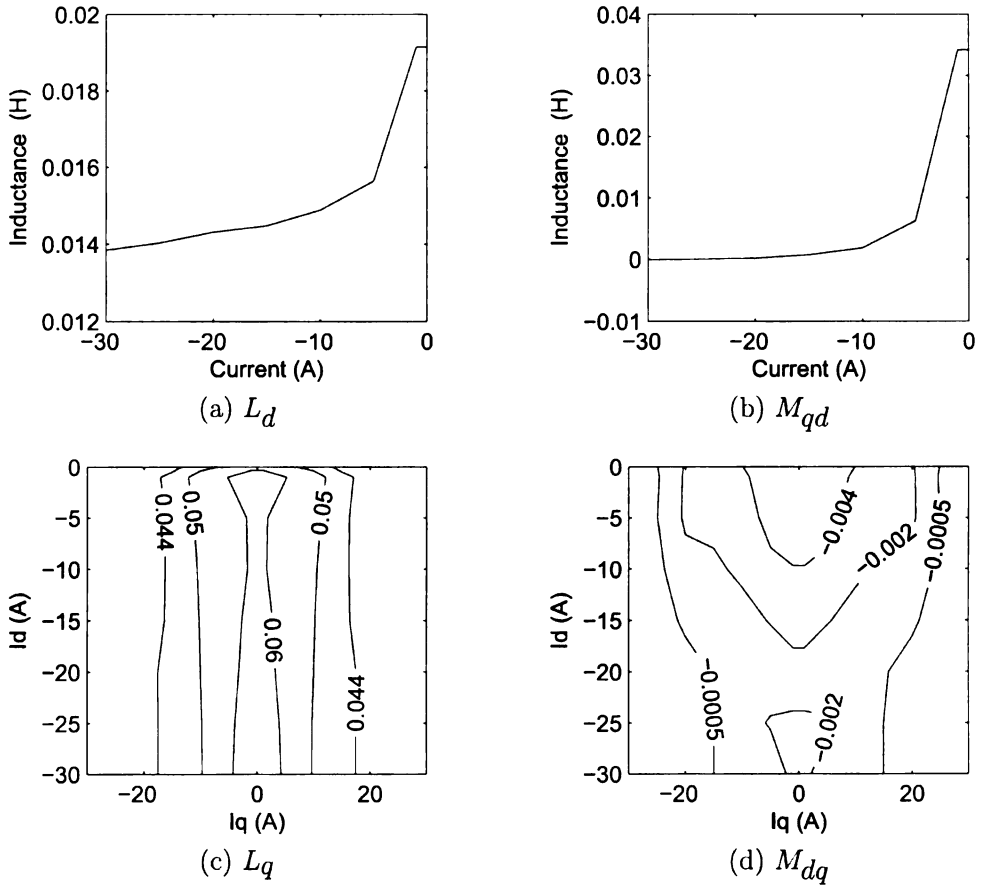

(a) L_d (b) M_{qd}

(c) L_q (d) M_{dq}

Figure 3.24: Calculated experimental inductances using V^*

Chapter 4

Trajectory Optimization for the Operation of Traction Motors

Motor efficiency and hence the motor controller performance depend on the model accuracy used for the controller design. In high power and high power density machines saturation and cross saturation significantly affects the flux linkages and torque; in the same manner current commands calculated from the cross saturated model differs significantly from those calculated using the classical two-axis model with constant inductances. Here the cross-saturated model [9, 17, 11] of the IPMSM was used for the algorithm design.

Several approaches have been developed to design the speed, torque and current controllers for PMSM. Jeong *et al.* [18], Shinn-Ming *et al.* [19] and Cheol *et al.* [20] calculated the optimized currents commands for torque control, however, cross saturation was not considered and the trajectory calculation for the speed control was not analyzed. In [21] the online calculated current commands depend on the predefined motor losses; this control scheme allows the operation of the motor with fixed losses for a wide range of speed, but cross saturation was neglected. Molavi *et al.* [22], Mademlis *et al.* [23] and Cavallaro *et al.* [24] designed optimal speed

controls without including the saturation effect in the inductances. In [22] the current commands were calculated using a suboptimal controller by considering the motor as a linear system with constant parameters. In [23, 24] a current controller with minimal losses was presented but the speed control was not analyzed or optimized.

Panahi *et al.* [25], Schlemmer *et al.* [26] and Choi *et al.* [27] presented optimal time trajectory references calculation, where motor losses were not optimized. In [25] a simpler algorithm is presented in order to apply it in a low cost controller. In [26, 27] the limitations of the actuator were included to get better accuracy. Niño *et al.* [28] presented an optimal speed controller of an IPMSM, however the iron losses were neglected and the details for an on-line implementation were not presented.

The contributions presented in this chapter are to develop an algorithm to calculate the speed command for the speed controller and an approximation to the optimal controller command to be used in real time. The speed command is calculated by a trajectory optimization. This trajectory has to achieve a predefined speed in a fixed time, minimizes energy losses and keeps good dynamic performance of the drive. The cross saturation effect was included to improve the solution accuracy, where the algorithm and modeling complexity are justified for high power density machines like the motor prototype presented in this thesis.

The optimization presented in this chapter, to determine a trajectory for the speed controller of the traction motors in a series HEV, was developed in two stages. In the first stage the optimal currents I_s and I_d are determined to operate the machine at a specified torque and speed point with minimum losses. In the second stage the optimal trajectory, between two torque and speed points, is determined.

4.1 Problem Description

The optimization problem presented in this chapter results in the calculation of the speed reference for the controller of the traction motors in a series HEV as shown in Figure 4.1. In Series HEV the speed command for the traction motor is given by the main controller, and the transition from one operation point to another is decided by the motor controller. The optimization goal is to produce a transition between two operation points efficiently, that is minimizing the motor losses.

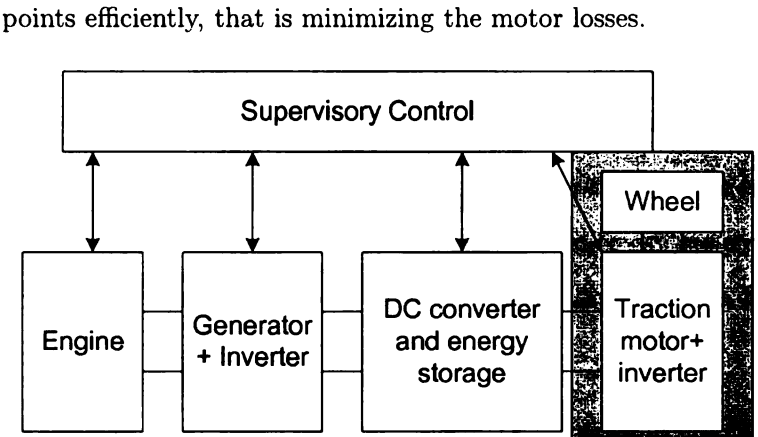

Figure 4.1: Series HEV configuration

The subsystem of traction motor and the wheels are simulated by the motor described in section 3.4.3 and a dynamometer was used to simulate the load (equivalent inertia of the vehicle and the additional torque due to the grade). The experimental setup is the same as shown Figure 3.18 and its details are described in Apendix A.

4.2 Maximum Torque Calculation

The calculation of the optimal currents commands was developed by the numerical inversion of the model shown in equations (3.12-3.20). In order to invert the model,

a control strategy should be defined; the control strategy was based on the maximum efficiency operation of the motor. The algorithm used to calculate the current commands I_d and I_q that operates the PMSM at a specific torque and speed point with minimum losses is presented below.

1. The system of equations (3.12) to (3.20) is solved to determine the relationship between torque and speed with stator current components. The fist part requires to calculate the torque from known values of stator current components I_d and I_q. It is unfeasible to analyze all operation points of the motor, a representative combinations of I_d and I_q where analyzed. For simplicity the torque is evaluated in the points located in a mesh of I_s and δ (that is equivalent to evaluate combinations of I_d and I_q). The points in the mesh are equally spaced in I_s in a range from $I_s = 0$ to $I_s = Imax$ and equally spaced in δ for a range from $\delta = 90^0$ to $\delta = 180^0$.

2. The torque is evaluated for a selected value of I_s, the angle of the Current Space Vector (CSV) 'δ' is varied from 90^0 to 180^0 and the machine output torque is calculated. As an example, two typical curves of the torque as a function of δ are shown in Figure 4.2 for stator current values of $I_s = I_{max}$ and $I_s = I_{max}/2$. For the selected stator current I_s, the angle $\alpha_0(I_s)$ for maximum torque was calculated, in this case $\alpha_0(I_{max}) = 128^0$ and $\alpha_0(I_{max}/2) = 116^0$. Below the corner speed, the machine was operated at maximum torque per ampere, hence from zero to the corner speed the current CSV angle is equal to $\delta = \alpha_0$.

3. The corner speed was calculated by solving equations (3.12-3.16) in 'steady state'. The unknown values of V_d, V_q and ω_e are calculated from the motor model and with the known values of $v_s = V_{s-max}$ (that is the maximum available voltage produced by the inverter) and the stator current components I_d and I_q (calculated from the selected current I_s and its angle for maximum

torque per ampere $\delta = \alpha_0$). For the example presented above and for $i_s = I_{max}$, the calculated corner speed is 630 r/min.

4. Above the corner speed the machine operates at the maximum voltage of the inverter (not at maximum torque per ampere), and the angle of the current space vector was increased. The CSV angle is increased in fixed steps, from $\delta = \alpha_0$ to $\delta = 180^0$. For the sets of I_d, I_q (generated by changing δ and for the selected I_s) and V_s, equations (3.14), (3.15) and (3.16) were solved for V_d, V_q and ω_m.

5. The previous steps allow us to determine the relation between the angle of the current space vector δ and the speed, hence the relation between torque and speed was established. Figure 4.2 was modified and the horizontal axis was changed to speed, as shown in Figure 4.3.

6. The torque calculation described above did not include the iron losses. To account for them, the torque at every speed was decreased by the torque loss due to the iron losses. Figure 4.4 shows the corrected curve. For the machine presented in section 3.4.3 the iron losses were not significant within the speed range, this is why Figure 4.3 is similar Fig. 4.4. The procedure described in the previous items is used to determine the relation between: τ_e and ω_m with I_d and I_q.

7. The previous process was repeated for I_s from I_{max} to zero. With the calculated values it was possible to create maps of i_s and i_d as shown in Figure 4.5.

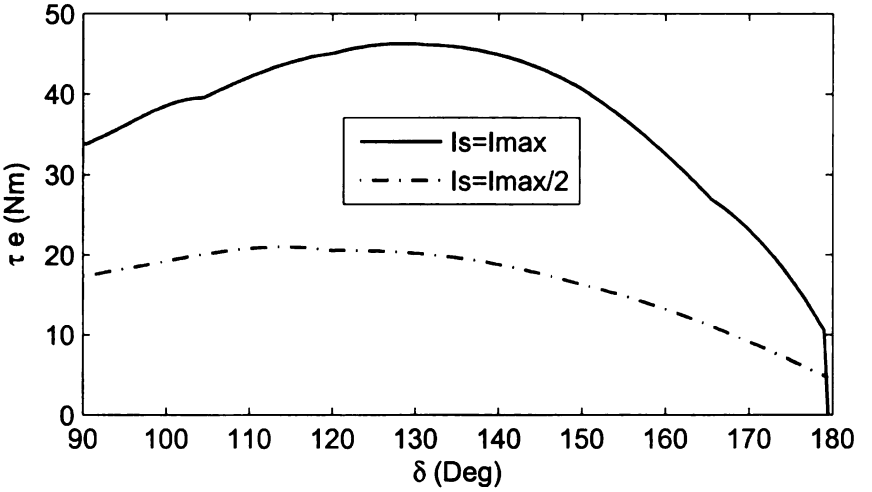

Figure 4.2: Torque as function of δ for rated and half of rated current

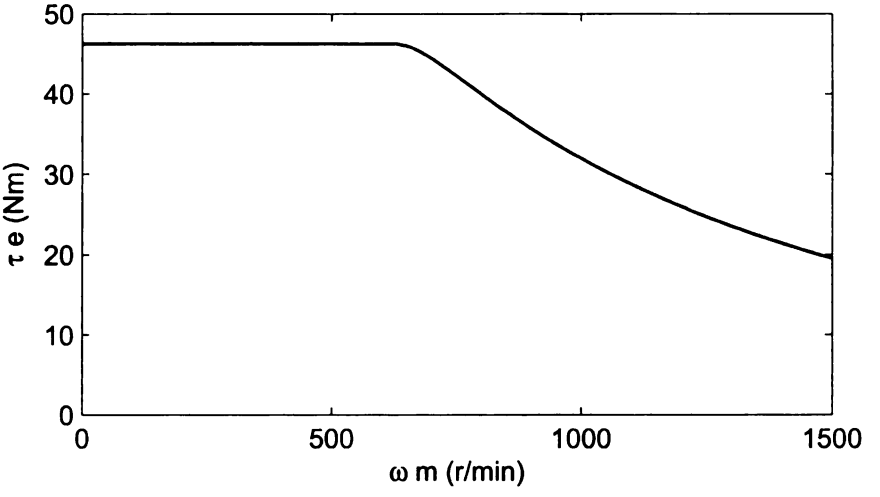

Figure 4.3: Torque as function of speed for maximum current

4.3 Optimal Trajectory Calculation for the Operation of Traction Motors

The second stage of the work address the speed reference calculation by a numerical optimization. The trajectory calculation problem presented in section 4.1 uses the currents commands calculated in section 4.2 to determine the speed reference. The

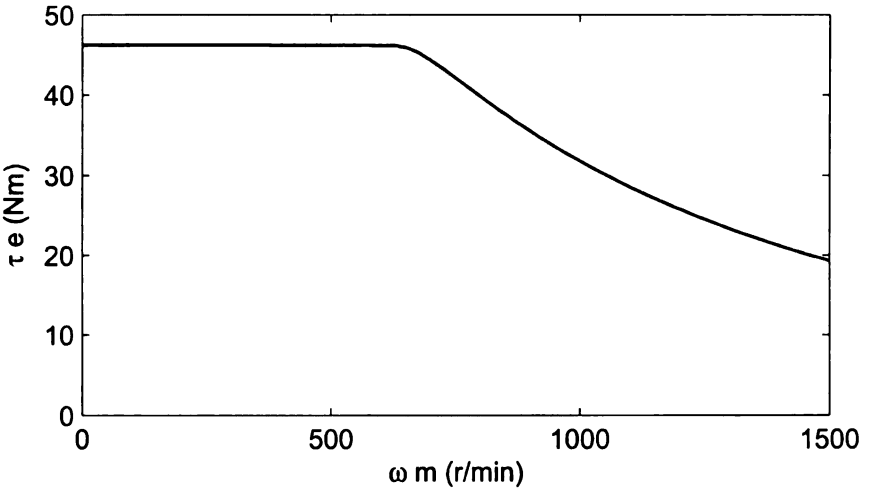

Figure 4.4: Torque as function of speed corrected by the iron losses

trajectory was calculated by minimizing a cost function, this minimization was donee by a numerical constrained optimization, based on the steepest descent method [29]. Trade of between losses minimization and high dynamic performance is the criteria used to determine the trajectory.

4.3.1 General Trajectory Optimization Algorithm

In this subsection, a general minimization problem is presented and the necessary conditions are shown. The performance cost J is a function of the input $u(t)$, the state variables $x(t)$, the initial time t_i, and final time t_f:

$$J = f\left(x(t_f), t_f\right) + \int_{t_i}^{t_f} g\left((t), u(t), t\right) dt, \tag{4.1}$$

where f is a function that depends of the state variables at the final time and g is a function that depends on the inputs, outputs, and time. The state equation (4.2) describes the dynamics of the system.

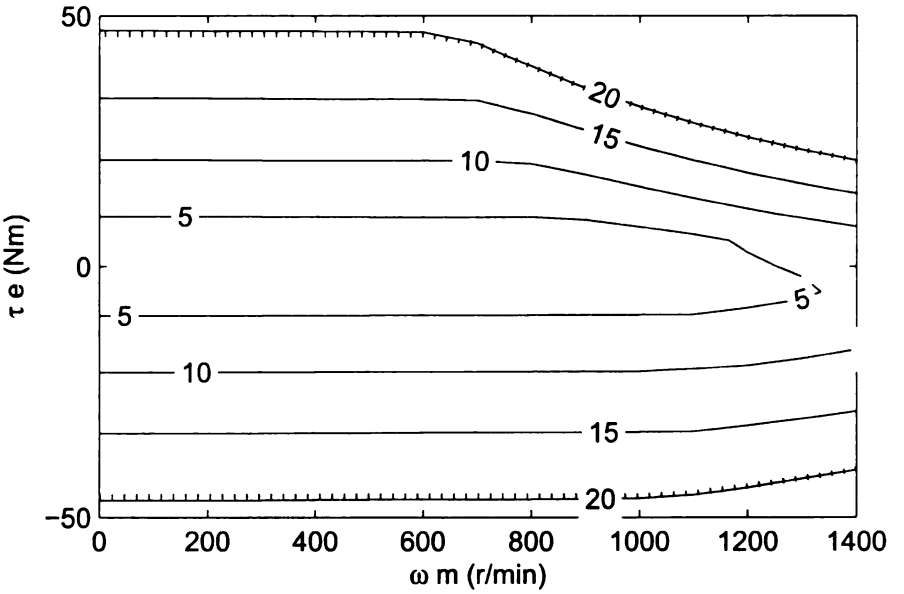

(a) i_s

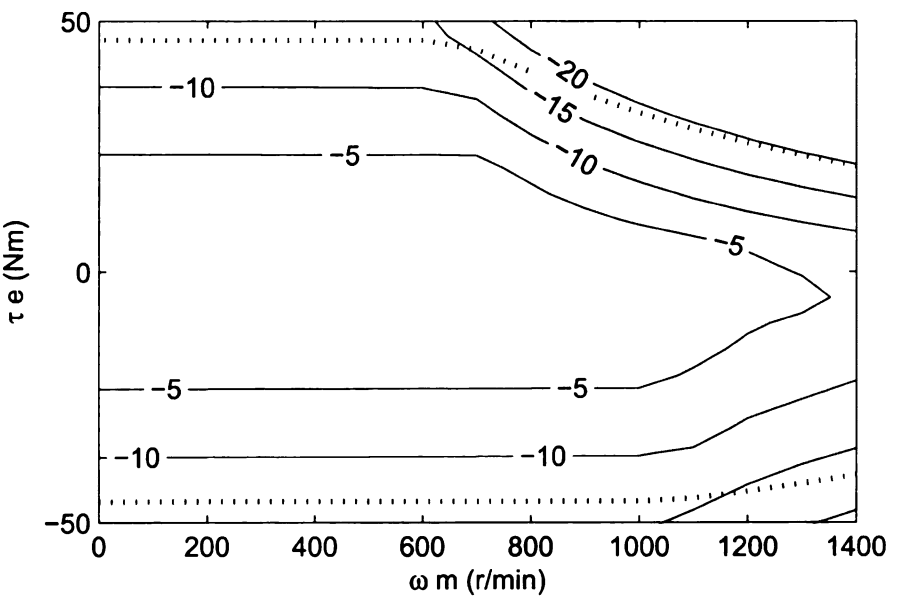

(b) i_d

Figure 4.5: Optimal current commands

$$\frac{\partial x(t)}{\partial t} = a\left(x(t), u(t)\right), \tag{4.2}$$

with the initial condition

$$x(t_i) = x_{ti}. \tag{4.3}$$

To minimize the cost function, the control functions $u(t)$ have to be determined. The minimization method used is the minimal principle as described by Athans and Falb [30]. The calculation of the control function with the minimal principle method requires the calculation of the Hamiltonian shown in equation (4.4). From the Hamiltonian, the differential equations used calculate costate function $P(t)$ and the boundary conditions are determined. Finally, by solving the state and the costate equations, the control function is calculated. The Hamiltonian, $\mathcal{H}$, is defined as:

$$\mathcal{H}\left(x(t), u(t), P(t)\right) = g\left(x(t), u(t)\right) + P(t)a\left(x(t), u(t)\right) \tag{4.4}$$

The costate function has to satisfy:

$$\dot{P}(t) = -\frac{\partial \mathcal{H}\left(x(t), u(t)\right)}{\partial x(t)} \tag{4.5}$$

with the boundary condition:

$$\frac{\partial f\left(x(t_f)\right)}{\partial x(t_f)} - P\left(t_f\right) = 0 \tag{4.6}$$

Besides satisfying the previous equations, the system has to satisfy the following necessary condition:

$$0 = \frac{\partial \mathcal{H}(x(t), u(t), P(t))}{\partial u(t)} \tag{4.7}$$

4.3.2 Continuous Time Trajectory Optimization of the Traction Motor System Controller

The general algorithm for trajectory optimization in subsection 4.3.1 was applied to the calculation of torque and speed references for the traction motor. Initial and reference speed, load torque and final time are assumed to be known before the optimization starts. The performance measure function 'J' was designed to give a tradeoff between dynamic performance of the drive and the motor losses. The performance measure function, also called cost function, is shown below:

$$\begin{aligned} J &= f(\omega_m(t_f), t_f) + \int_{t_i}^{t_f} g\,(\omega_m, i_s, t)dt \\ &= h_0(\omega_m(t_f) - \omega_{ref})^2 \\ &+ \int_{t_i}^{t_f} \left(h_1\left(\omega_m - \omega_{ref}\right)^2 + h_2\left(\frac{3}{2}R{i_s}^2 + k_{i-loss}\omega_m^2\right)\right)dt \end{aligned} \tag{4.8}$$

where h_0 is the weight used to lead the algorithm to reach the final speed, h_1 is the weight for the time required to reach the reference speed, and h_2 is the weight of the motor losses. The selection of these gains leads to a tradeoff between dynamic speed response of the controller and energy losses. The mechanical equation that describes the dynamics of the motor and the load is shown below:

$$J_m\frac{\partial\omega_m}{\partial t} = \tau_e\,(i_s, \omega_m) - \tau_l - B_m\omega_m \tag{4.9}$$

where J_m is the inertia of the system, τ_l is the load torque and B_m is the viscous friction coefficient. The mechanical system can be rearranged as:

$$\begin{aligned}\frac{\partial \omega_m}{\partial t} &= a(\omega_m, i_s, t) \\ &= \frac{\tau_e\,(i_s, \omega_m)}{J_m} - \frac{\tau_l}{J_m} - \frac{B_m \omega_m}{J_m}\end{aligned} \tag{4.10}$$

with the state $x(t) = \omega_m$ and the control input $u(t) = i_s(t)$. The nonlinear relation between τ_l, ω_m and i_s was established in 4.3, where the information presented in Figure 4.5 was stored in lookup tables. The value of $i_s\,(\omega_m, \tau_e)$ is calculated by using a bilinear interpolation described in the next subsection.

Equations (4.8 to 4.10) were used to create the Hamiltonian:

$$\begin{aligned}\mathcal{H}\,(i_s, P, \omega_m) = h_1\left(\omega_m - \omega_{ref}\right)^2 + h_2\left(\frac{3}{2}R{i_s}^2 + k_{i-loss}\omega_m^2\right) \\ + P(t)\left(\frac{\tau_e}{J_m} - \frac{\tau_l}{J_m} - \frac{B_m \omega_m}{J_m}\right)\end{aligned} \tag{4.11}$$

The costate function is rewritten as:

$$\dot{P} = -2h_1(\omega_m - \omega_{ref}) - 2h_2 k_{i-loss}\omega_m - \frac{P(t)}{J_m}\left(\frac{\partial \tau_e}{\partial \omega_m} - B_m\right) \tag{4.12}$$

$$P_{tf} = 2h_0(\omega_m(t_f) - \omega_{ref}) \tag{4.13}$$

with the boundary condition:

$$0 = 2h_2 R i_s + P(t)\left(\frac{1}{J_m}\frac{\partial \tau_e}{\partial i_s}\right) \tag{4.14}$$

4.3.3 Numerical Optimization

The continuous time optimization problem of subsection 4.3.2 was solved numerically. State and costate equations have to be solved in discrete time and the calculation of

the control input have to be done iteratively.

First we rewrite the state equation in discrete time as:

$$\omega_m^{i+1} = \Delta t \left[\frac{\tau_e^i \left(i_s^i, \omega_m^i \right)}{J_m} - \frac{\tau_l^i}{J_m} - \frac{B_m \omega_m^i}{J_m} \right] + \omega_m^i \tag{4.15}$$

where Δt is the sampling time, and i is the sample number. The control input i_s is related with τ_e in a nonlinear form. To determine τ_e for a given value of i_s and ω_m a bilinear interpolation can be used. Figure 4.6 shows a representative grid of the data stored as a lookup table, equation (4.16) is used to determine $\tau_e \left(i_s, \omega_m \right)$

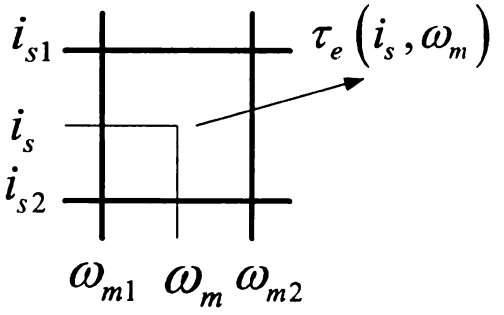

Figure 4.6: Bilinear interpolation

$$\begin{aligned} \tau_e \left(i_s, \omega_m \right) \approx & \frac{\tau_e \left(i_{s1}, \omega_{m1} \right)}{\Delta i_s \Delta \omega_m} \left(i_{s2} - i_s \right) \left(\omega_{m2} - \omega_m \right) \\ & + \frac{\tau_e \left(i_{s2}, \omega_{m1} \right)}{\Delta i_s \Delta \omega_m} \left(i_s - i_{s1} \right) \left(\omega_{m2} - \omega_m \right) \\ & + \frac{\tau_e \left(i_{s1}, \omega_{m2} \right)}{\Delta i_s \Delta \omega_m} \left(i_{s2} - i_s \right) \left(\omega_m - \omega_{m1} \right) \\ & + \frac{\tau_e \left(i_{s2}, \omega_{m2} \right)}{\Delta i_s \Delta \omega_m} \left(i_s - i_{s1} \right) \left(\omega_m - \omega_{m1} \right) \end{aligned} \tag{4.16}$$

with $\Delta \omega_m = \omega_{m2} - \omega_{m1}$ and $\Delta i_s = i_{s2} - i_{s1}$. The costate and its final condition

equation in discrete time are given by:

$$P^{i-1} = -\left[-2h_1(\omega_m^i - \omega_{ref}) - 2h_2 k_{i-loss}\omega_m^i - \frac{P^i}{J_m}\left(\frac{\partial \tau_e^i}{\partial \omega_m^i} - B_m\right)\right]\Delta t + P^i \tag{4.17}$$

$$P_{Ntf} = 2h_0(\omega_m^{Ntf} - \omega_{ref}) \tag{4.18}$$

where the partial derivative can be calculated as follows:

$$\begin{aligned}
\tau_e^i\left(i_s^i, \omega_{m1}^i\right) &\approx \frac{\tau_e^i\left(i_{s2}^i, \omega_{m1}^i\right) - \tau_e^i\left(i_{s1}^i, \omega_{m1}^i\right)}{i_{s2}^i - i_{s1}^i}\left(i_s^i - i_{s1}^i\right) + \tau_e^i\left(i_{s1}^i, \omega_{m1}^i\right) \\
\tau_e^i\left(i_s^i, \omega_{m2}^i\right) &\approx \frac{\tau_e^i\left(i_{s2}^i, \omega_{m2}^i\right) - \tau_e^i\left(i_{s1}^i, \omega_{m2}^i\right)}{i_{s2}^i - i_{s1}^i}\left(i_s^i - i_{s1}^i\right) + \tau_e^i\left(i_{s1}^i, \omega_{m2}^i\right) \\
\frac{\partial \tau_e^i\left(i_s^i, \omega_m^i\right)}{\partial \omega_m^i} &\approx \frac{\tau_e^i\left(i_s^i, \omega_{m2}^i\right) - \tau_e^i\left(i_s^i, \omega_{m1}^i\right)}{\Delta \omega m}
\end{aligned} \tag{4.19}$$

Equation (4.14)becomes:

$$0 = 2h_2 R i_s^i + P^i\left(\frac{1}{J_m}\frac{\partial \tau_e^i}{\partial i_s^i}\right) \tag{4.20}$$

where the partial derivative can be calculated as follows:

$$\tau_e^i\left(i_{s1}^i,\omega_m^i\right) \approx \frac{\tau_e^i\left(i_{s1}^i,\omega_{m2}^i\right)-\tau_e^i\left(i_{s1}^i,\omega_{m1}^i\right)}{\omega_{m2}^i-\omega_{m1}^i}\left(\omega_m^i-\omega_{m1}^i\right)+\tau_e^i\left(i_{s1}^i,\omega_{m1}^i\right)$$

$$\tau_e^i\left(i_{s2}^i,\omega_m^i\right) \approx \frac{\tau_e^i\left(i_{s2}^i,\omega_{m2}^i\right)-\tau_e^i\left(i_{s2}^i,\omega_{m1}^i\right)}{\omega_{m2}^i-\omega_{m1}^i}\left(\omega_m^i-\omega_{m1}^i\right)+\tau_e^i\left(i_{s2}^i,\omega_{m1}^i\right)$$

$$\frac{\partial\tau_e^i\left(i_s^i,\omega_m^i\right)}{\partial\omega_m^i} \approx \frac{\tau_e^i\left(i_{s2}^i,\omega_m^i\right)-\tau_e^i\left(i_{s1}^i,\omega_m^i\right)}{\Delta i_s} \tag{4.21}$$

The steepest descent method was chosen to solve the optimization problem. The control function is calculated iteratively, which leads to the iterative minimization of the performance measure function. The steepest descent method [29] is used to calculate the control function iteratively. The control input is updated every iteration, equation (4.14) is modified to create an update for $u(t)$ as follows:

$$\begin{aligned} i_s^{i,l+1} &= i_s^{i,l}+\tau_{adap}\frac{\partial\mathcal{H}(i_s^{i,l},P,\omega_m)}{\partial i_s^{i,l}} \\ &= i_s^{i,l}+\tau_{adap}\left(2h_2Ri_s^{i,l}+P^i\left(\frac{1}{Jm}\frac{\partial\tau_e^i}{\partial i_s^{i,l}}\right)\right) \end{aligned} \tag{4.22}$$

where l is the iteration number and τ_{adap} is the adaptation step. The value of i_s^{l+1} can be greater than the maximum allowed, a basic saturation is used to limit i_s. The general algorithm flowchart do determine the speed reference is presented in Figure 4.7.

4.4 Simulated and Experimental Results

4.4.1 Simulation Results

The proposed algorithm was tested for three sets of weights h_0, h_1, and h_2 to demonstrate the performance of the algorithm. The selection criteria for the weights was a tradeoff between the speed response of the controller and the energy losses. The sets of weights are shown in table 4.1. The final time selected was $t_f = 6s$, the initial speed was $\omega_m(t_i) = 500\ r/min$, the reference speed was $\omega_m(t_f) = 1200\ r/min$, and a load torque was $\tau_l(t) = 17Nm$.

Table 4.1: Weight sets h_0 h_1 h_2

Set Number	h_0	h_1	h_2
Set 1	20000	50	2000
Set 2	20000	100	1333
Set 3	20000	400	333

First the convergence of the algorithm was investigated. Figure 4.8 shows how the cost changes with the number of the iterations. The rate of convergence of the speed depends on the adaptation step τ_{adap}, and the initial guess of the trajectory. This initial trajectory was a straight line between the initial and final points, however a more refined approach can be used to reduce the number of iterations required to reach the minimum, as will be presented in the next section.

Figure 4.9 presents the trajectories resulting from the optimization algorithm for the three sets of weights. For illustration the trajectories were plotted over the contour curves of equal current i_s. Figures 4.10, 4.11 and 4.12 show the change of the speed ω_m, torque τ_e and current i_s as functions of time.

The energy losses are $524J$, $698J$ and $924J$ for sets 1, 2 and 3 respectively. These results show that although all trajectories reach the final speed in the specified final time, different trajectories have different energy losses, e.g. trajectory 3 has 60% more

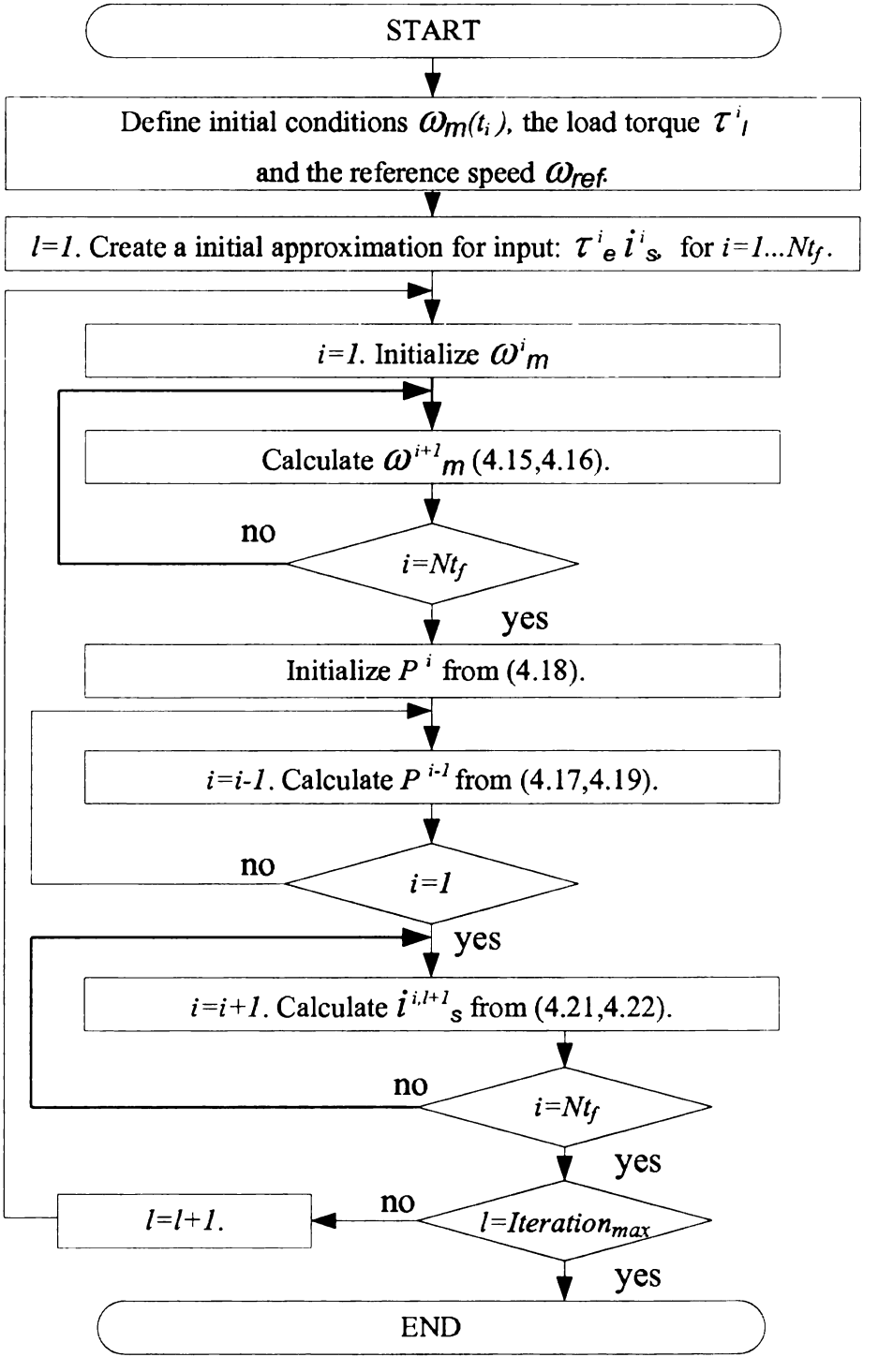

Figure 4.7: Optimal algorithm flowchart

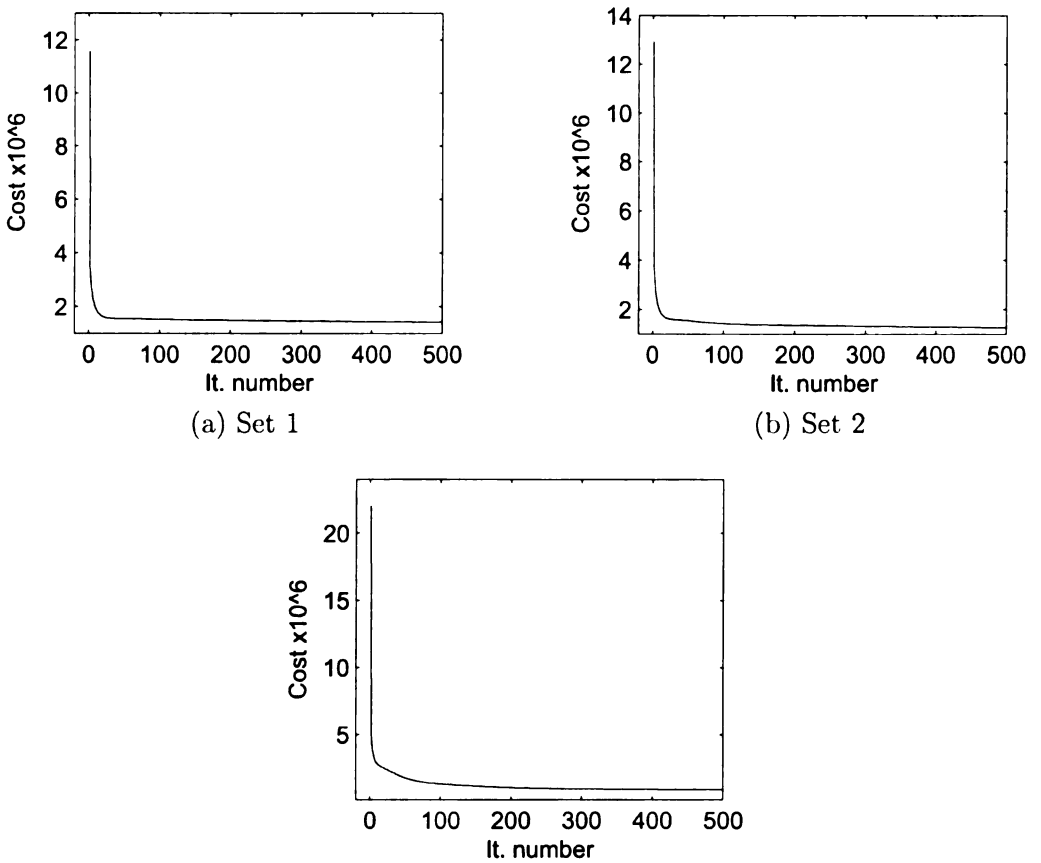

(a) Set 1

(b) Set 2

(c) Set 3

Figure 4.8: Cost vs. iteration number

energy losses than trajectory 1.

Figure 4.13 shows the proposed control scheme, where the trajectory resulting from the optimization process is used as a reference for the feedback controller.

4.4.2 Real Time Optimization

The optimization discussed so far cannot be easily implemented in real time, due to the long computational time required and the difficulty to the backward calculation of the costate function. A modification is discussed here to calculate the trajectory. After the off-line minimization, an approximation to the trajectory was made by cre-

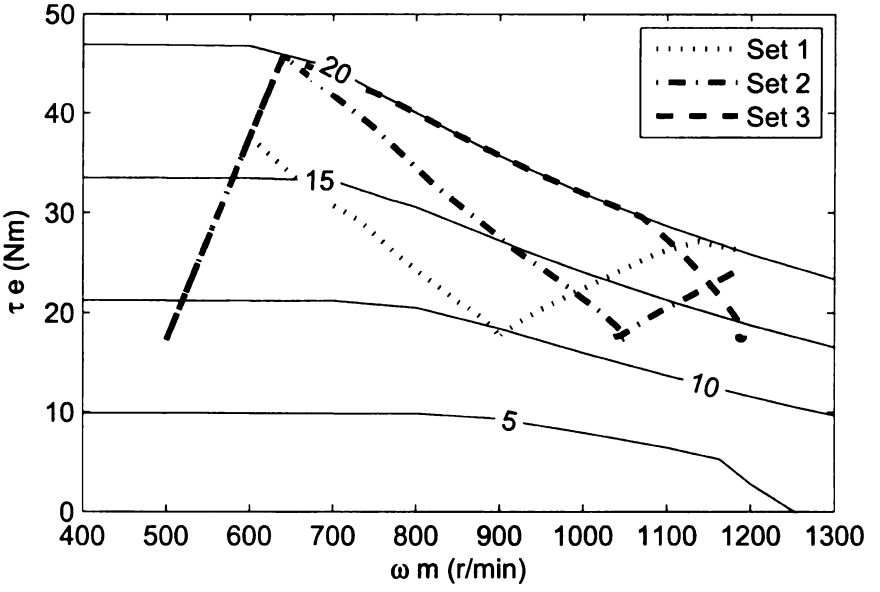

Figure 4.9: Simulated speed ω_m

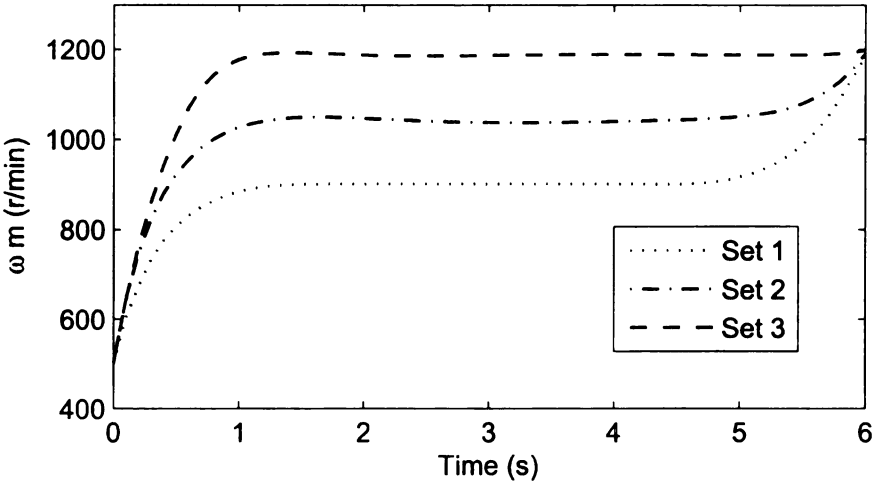

Figure 4.10: Simulated trajectories

ating a continuous function consisting of three sections. The functions were calculated by developing the optimization process for different sets of t_f, $\omega_m(t_i)$, $\omega_m(t_f)$ and τ_l and by making a curve fitting over the resulting data. The three sets of gains presented in the previous sections were further analyzed in order to verify the accuracy

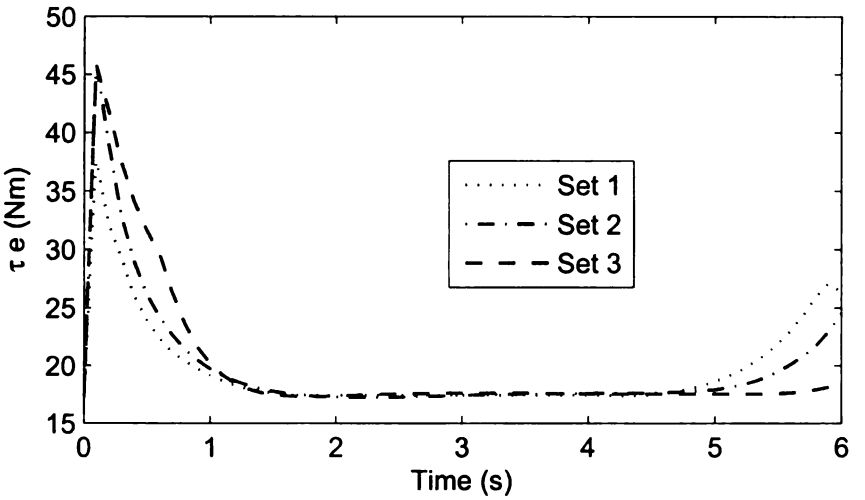

Figure 4.11: Simulated torque τ_e

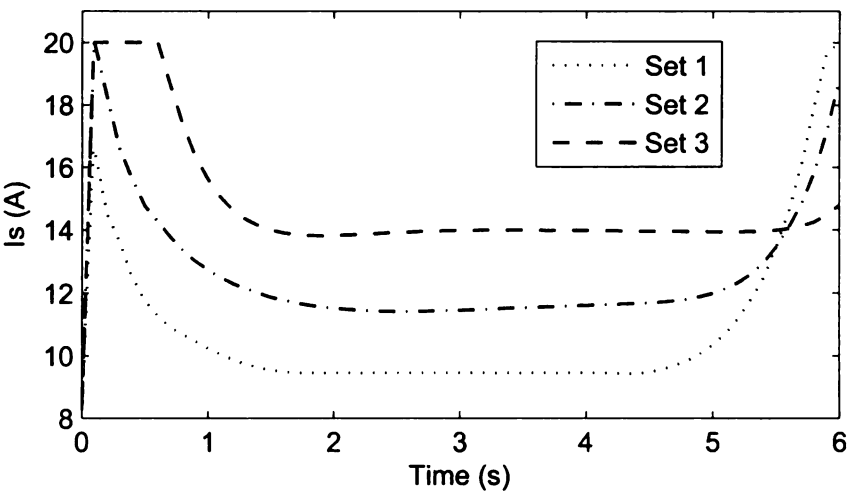

Figure 4.12: Simulated current i_S

of the approximated analytic function that models the optimal trajectory.

Figure 4.11 shows the torque trajectory as function of the time; this trajectory can be approximated by a sequence of three functions: The first is an exponentially decaying function, the second is a constant, and the third one is a exponentially increasing function. The coefficients depend on the initial and final speed, the final time and the final torque. The optimal trajectory calculation presented in the previous

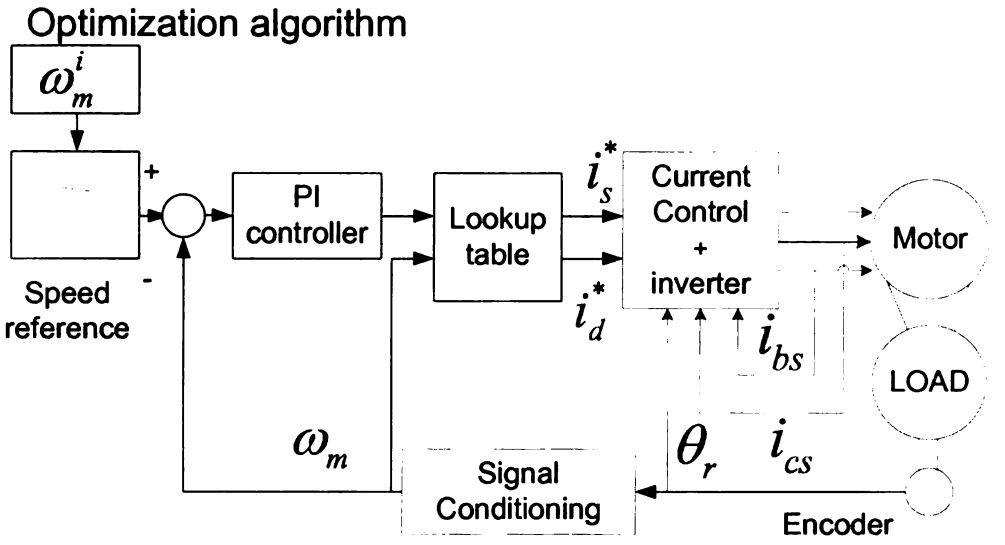

Figure 4.13: Controller topology

section for $t_f > 5\ s$ shows that the sum of the time of the two exponential functions is almost constant, which make the analysis for $t_f > 5s$ simpler than for $t_f < 5s$. As shown in Figure 4.11 for $t_f > 5s$, the duration of the second segment is equal to the difference between final time and $5s$.

The general form of the functions are shown in equations (4.23),(4.24),(4.25) and (4.26).

$$\tau_e(t) = \begin{cases} \tau_{e-1}(t) & for \quad 0 \leq t < t_1 \\ \tau_{e-2}(t) & for \quad t_1 \leq t < t_2 \\ \tau_{e-3}(t) & for \quad t_2 \leq t < t_f \end{cases} \tag{4.23}$$

$$\tau_{e-1}(t) = \left(k_{11} + k_{12}\left(\omega_m\left(t_f\right) - \omega_m\left(t_i\right)\right)\right) e^{-k_{13}t} + k_{14} * \tau_l \tag{4.24}$$

$$\tau_{e-2}(t) = k_{21} * \tau_l \tag{4.25}$$

$$\tau_{e-3}(t) = \left(k_{31} + k_{32}\left(\omega_m\left(t_f\right) - \omega_m\left(t_i\right)\right)\right) e^{+k_{33}t} + \left(k_{34} * \tau_l + k_{35}\left(\omega_m\left(t_f\right) - \omega_m\left(t_i\right)\right)\right) \tag{4.26}$$

where $t_1 = 3.5s$, and $t_f - t_2 = 1.5s$. This means that the approximation is valid for $t_f > 5s$. The constants of each function were calculated for a fixed set of weights of the cost function, i.e. for each set of weights of the cost function (h_0, h_1, h_2) there is a different set of gains $k_{i,j}$. Table 4.2 shows the calculated parameters for the three sets of weights analyzed in the previous sections.

Table 4.2: Constants for on-line optimization approximation for $t_f > 5\ s$

Functions parameters	Set number		
$k_{i,j}$	Set 1	Set 2	Set 3
k_{11}	3.39	2.825	-2.61
k_{12}	.02158	.028125	.088
k_{13}	1.3	1.4	3
k_{14}	.982	1	1.012
k_{21}	1.012	1.012	1.03
k_{31}	-0.11667	-0.11667	-0.11667
k_{32}	1.1667e-3	1.1667e-3	1.1667e-3
k_{33}	1.79	1	.9
k_{34}	1.025	1.025	1.025
k_{35}	-1.1667e-3	-1.1667e-3	-1.1667e-3

The approximate trajectories were evaluated for representative points with different initial and final torque-speed points and different final times. These representative trajectories were computed for each set of weights (h_0, h_1, h_2) described in the previous sections. The error in the cost function was calculated by using equation (4.27)

$$error = \frac{J\left(\omega_m(t_f), \omega_m, i_s\right) - J\left(\omega_m(t_f), \omega_m^*, i_s^*\right)}{J\left(\omega_m(t_f), t_f, \omega_m, i_s\right)} * 100 \tag{4.27}$$

where 'J' is defined in equation (4.8) and ω_m^* is calculated by using the approximated torque of equation (4.23) and solving the differential equation (4.10); 'i_s^*' is calculated by using the relation described in subsection 4.3 between 'i_s^*' and 'τ_e^*'.

Table 4.3 summarizes the results where optimal and suboptimal trajectory are compared in terms of the cost function error.

Table 4.3: Error in the cost function for $t_f > 5\ s$

Gain	Set number		
Cost function error %	Set 1	Set 2	Set 3
Minimum	0.94	0.47	3.33
Maximum	17.17	12.25	30.88
Mean	6.55	5.21	10.97

For $t_f < 5s$ the approximation is more complex and the time intervals t_1, and $t_f - t_2$ are not constant, moreover the function parameters are different than for $t_f > 5s$. The torque curve is composed by three functions as described in equation (4.23) and the time intervals are given in table 4.4. For t_f different than the values presented in table 4.4 a linear interpolation was used to determine the time intervals. The segments are again two exponentials and one straight line as shown in equations (4.24), (4.25), and (4.26), however the coefficients are slightly different, and are summarized in table 4.5.

Table 4.4: Time intervals for $t_f < 5s$

Final time	Time intervals	
t_f	t_1	t_2
$1(s)$	1	0
$2(s)$	1.4	0
$3(s)$	1.4	.8
$4(s)$	1.7	1.5

The performance of the approximation was evaluated. A summary of the analysis in presented in table 4.6.

Table 4.5: Constants for on-line optimization approximation for $t_f < 5s$

Functions parameters	Set number		
$k_{i,j}$	Set 1	Set 2	Set 3
k_{11}	-1.25	-1.75	3.8
k_{12}	.0375	.0525	.0756
k_{13}	1.5	2.3	3
k_{14}	1.02	1.05	.97
k_{21}	1.01	1.02	1.03
k_{31}	-0.035	-0.11667	-0.11667
k_{32}	1.05e-3	1.1667e-3	1.1667e-3
k_{33}	2.8	1.6	.9
k_{34}	1.06	1.048	1.0186
k_{35}	-1.75e-3	-1.1667e-3	-1.1667e-3

Table 4.6: Error in the cost function for $t_f < 5(s)$

Gain	Set number		
Cost function error %	Set 1	Set 2	Set 3
Minimum	.1428	.9254	0.01
Maximum	27.38	17.41	14.18
Mean	10.87	7.35	4.83

The approximate function can also be used as an initial guess for the optimization. The cases presented in the previous section, were further analyzed and the online approximation was used as an initial guess for the trajectory. The minimum value of the cost function is assumed to be the value after 1000 iterations.

The effect of the initial guess on the number of iterations was also considered. Two cases were evaluated: a straight line that connects initial and final torque-speed points, and the proposed curve approximation. The criterion to end the trajectory optimization was that the the cost function is within an error of 2% of the minimum value. Table 4.7 summarizes the results.

From the previous results it is clear that the use of the approximation curve as initial guess for the iterative optimization reduces the number of iterations required to achieve the optimal trajectory to about half.

Table 4.7: Maximum number of iterations

Cases analyzed	Set number		
Initial guess	Set 1	Set 2	Set 3
Linear trajectory	440	576	421
Approximated curve	132	179	78

4.4.3 Experimental Setup

The proposed algorithm was tested experimentally. The experimental setup is shown and described in Apendix A, for reference, the schematic of the experimental setup is shown in Figure 4.14. The speed from the optimization algorithm were used as reference for the controller, as shown in Figure 4.13. Any trajectory can be selected to validate the simulated results; the selected trajectory is the one corresponding to the weight set 3. The dynamometer was used as a load with constant torque. The experimental results are presented in Figures 4.15, 4.16 and 4.17 and the experimental motor energy losses are $875.5J$. Experimental results show a good agreement with the simulated values. The error in the energy losses was about 5.4%.

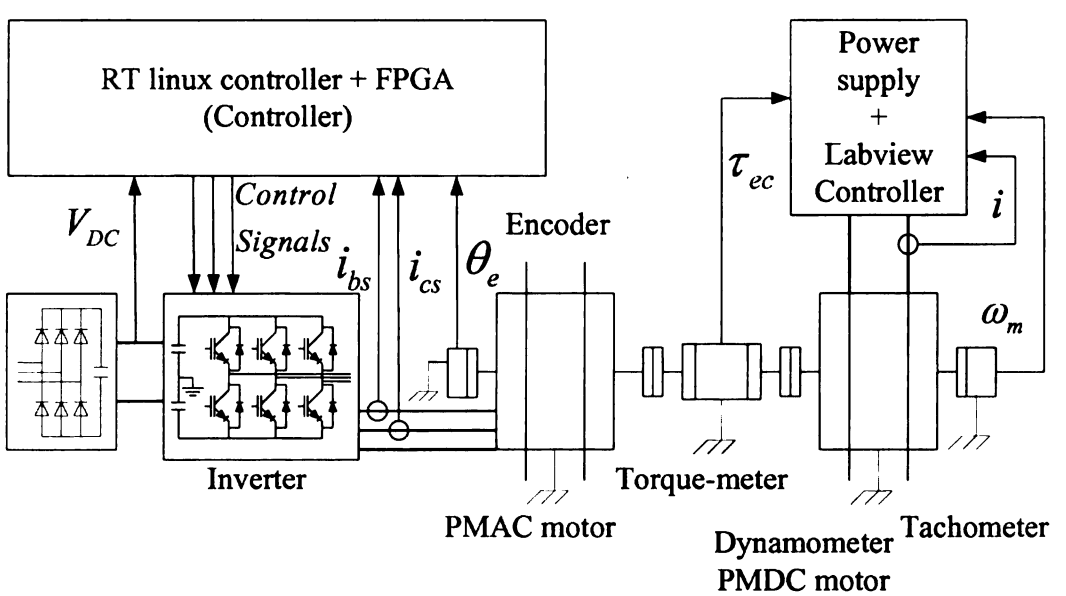

Figure 4.14: Experiment setup

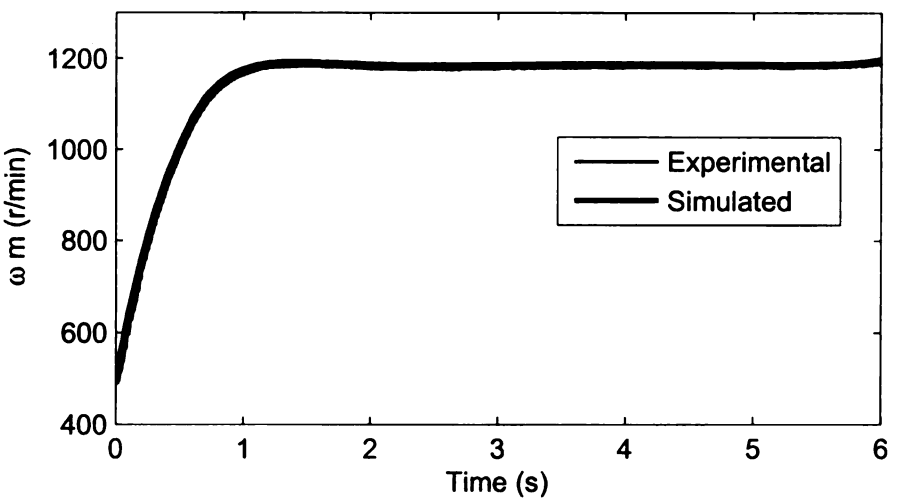

Figure 4.15: Comparison: experimental and simulated speed

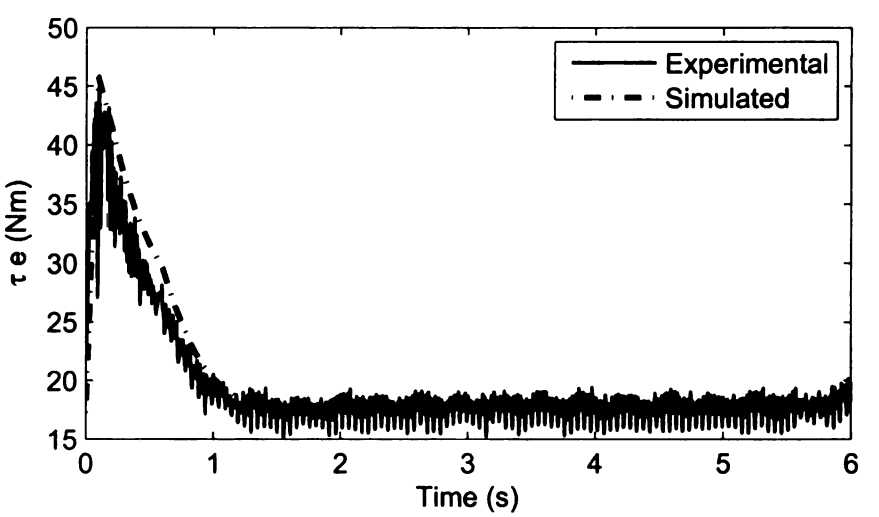

Figure 4.16: Comparison: experimental and simulated torque

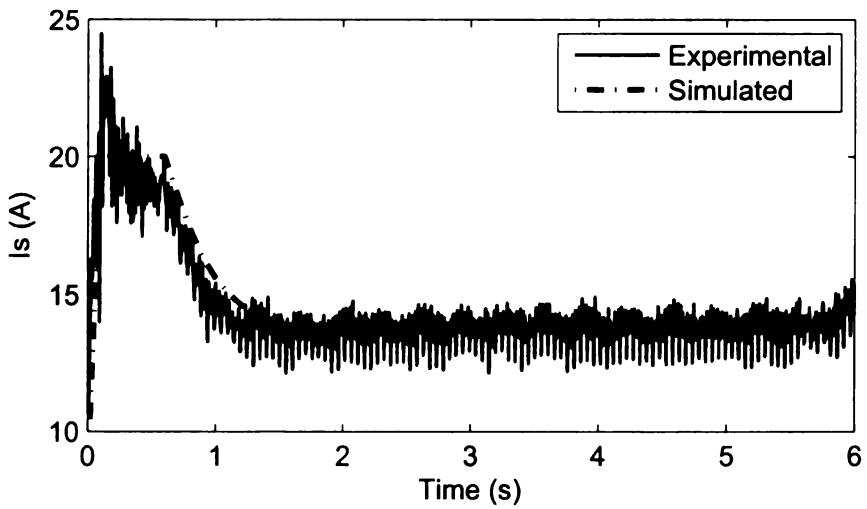

Figure 4.17: Comparison: experimental and simulated current

Chapter 5

Trajectory Optimization for Engine-Generator Operation of a Series Hybrid Electric Vehicle

This chapter presents a methodology of calculating the optimal torque and speed commands for the engine-generator system of a series Hybrid Electric Vehicle (HEV). In series HEVs the engine-generator subsystem provides electrical energy to the DC link. This chapter proposes an optimal control strategy of the engine-generator subsystem to generate a desired amount of energy within a given period of time. The optimization algorithm based on trajectory optimization determines the torque and speed reference signals for the engine-generator subsystem that achieve maximum efficiency with the desired energy. A simplified version of the controller is also presented for online implementation. The proposed control strategy is compared with non-optimized control techniques and simulation results show the improvements in energy efficiency.

5.1 Introduction

Series configuration is often used for high power hybrid electric vehicles [31], where the internal combustion engine converts the fuel energy into mechanical, and the generator converts the mechanical energy into electricity. The electrical energy is either stored in the batteries or consumed by the traction motors [32]. Several control strategies have been proposed to optimize the fuel consumption in electric vehicles [33, 34]. These include global optimization (such as linear programming, control theory, dynamic programming and stochastic digital programming), and online optimization (equivalent fuel consumption, robust control, fuzzy logic and optimal predictive control).

The hybrid vehicle supervisory control system optimizes the engine-generator operation as a single DC source [35, 36, 37] at steady state, while the transient operation is usually neglected. The torque and speed references for the engine-generator result from the optimization of the overall system; the supervisory controller takes into account the efficiency of the devices that comprise the traction system and determines the power distribution of each subsystem [38].

Similar considerations with respect to the generator-engine subsystem were made for the power distribution in series Hybrid Electrical Vehicle (HEV) [39]; the optimization algorithm used there was dynamic programming. The objective function was designed to minimize the energy losses over a driving cycle, while achieving the wheel speed requirements. The power distribution algorithm did not consider the subsystem limitations such as torque and speed, and the mechanical system dynamics were neglected. Simulation results showed the power distribution and the fuel consumption.

Ceraolo *et al.* [40] proposed a methodology that optimized the operation of the engine-generator subsystem. The subsystem torque and speed were determined by

the requested power for a certain period, and the optimization scheme found the optimal operational speed and load conditions that provide the desired power with maximum efficiency. The resulting speed and torque were used as references for the engine and generator controllers. This optimization process does not consider the operational efficiency during the transition between two operational conditions, which is not necessary optimal.

This chapter presents an optimal control strategy of the engine-generator subsystem. Starting from a requested electrical energy to be delivered from the generator in a given time interval, the trajectory optimization scheme determines the optimal torque and speed references required to satisfy this request with minimal energy loss. The advantage of this optimization is that it is based on the fact that the power provided by the engine-generator subsystem is not constant.

The chapter is organized as follows: section 5.2 presents the optimization problem and the engine-generator efficiency maps. Section 5.3 describes the trajectory optimization scheme. The minimization problem is described in continuous time domain and the problem is solved using numerical optimization in discrete time. Simulation results of the proposed trajectory optimization are presented. Section 5.4 presents an approximation to the optimal trajectory. Section 5.5 shows the resulting efficiency and compared it to that of non-optimized control techniques.

5.2 System Description

The optimization problem presented in this chapter results in the calculation of the torque and speed references for the engine-generator subsystem. In series HEVs the system of engine and generator is shown in Figure 5.1. The goal of the optimization is to produce the requested electrical energy at the generator terminals in a given period of time, while minimizing the energy losses.

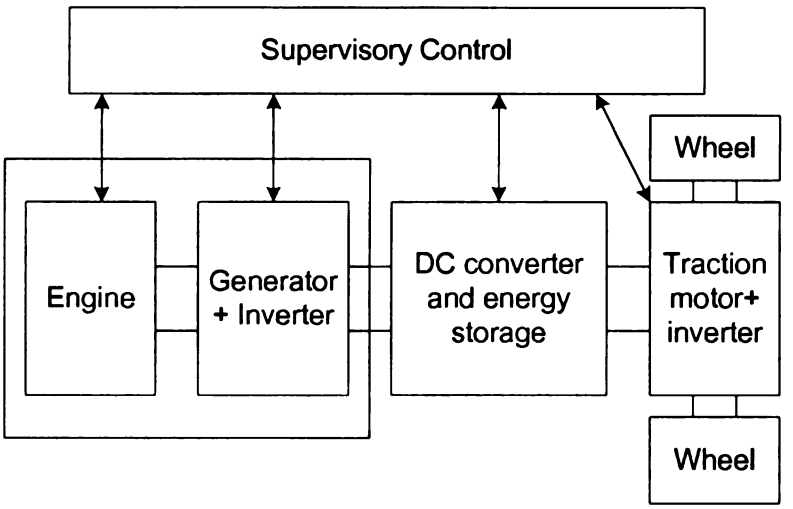

Figure 5.1: Series HEV configuration

The method was applied to a specific engine-generator system. The efficiency maps for the engine and the generator of this system are shown in Figure 5.2 and Figure 5.3 respectively. Figure 5.2 shows the efficiency map of a 6 cylinder Cummings engine rated at 194 kW. Figure 5.3 shows the efficiency map of an IPMSM rated $130kW$ connected to an inverter. Engine and generator efficiency maps presented are for the useful speed range of $1100 - 2200\ r/min$; the torque range as a function of speed is presented by solid bold lines. Subsystem loses are calculated for each operational condition based upon these two efficiency maps. Inertia and viscous friction coefficient of the system are also used for the loss calculation.

5.3 Trajectory Optimization

This section describes the trajectory optimization. The trajectory, consisting of the points in time of torque and speed, was calculated by minimizing a cost function. The numerical constrained optimization used was based on the steepest descent method [29]. The general minimization problem and its necessary conditions were presented in subsection 4.3.1.

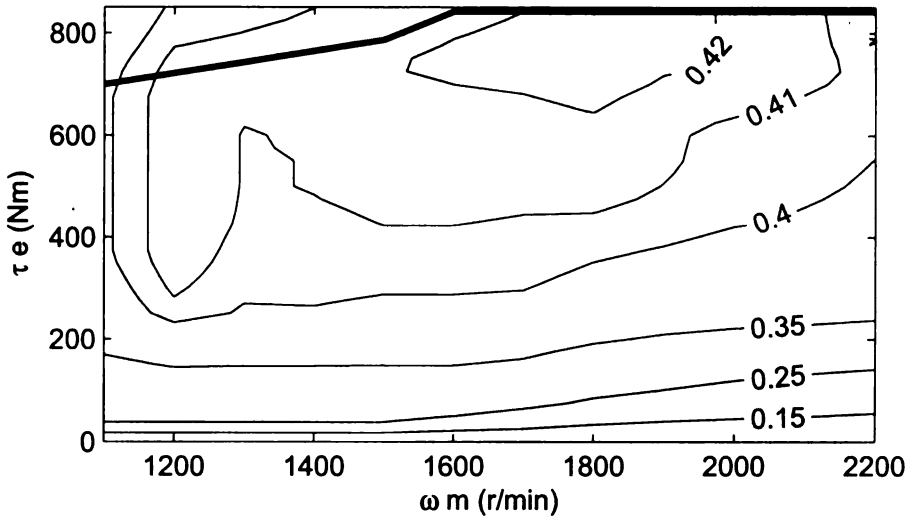

Figure 5.2: Engine efficiency map contours

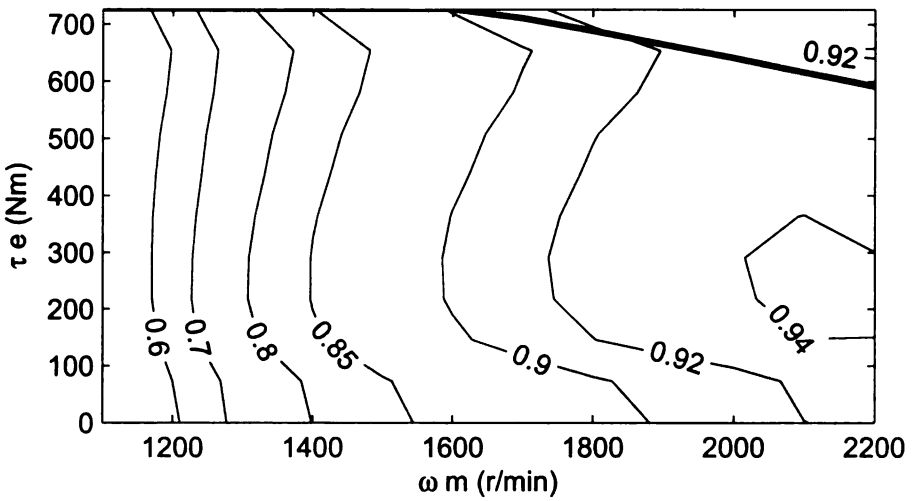

Figure 5.3: Generator efficiency map contours

5.3.1 Trajectory Optimization for the Operation of Engine-generator System

The general algorithm for trajectory optimization in subsection 4.3.1 was applied to the calculation of torque and speed references for the engine-generator subsystem. Initial speed and final command time are assumed to be known before the optimization

starts. The final energy can be obtained by modifying the supervisory control system to provide energy instead of torque and speed. The performance measure function, J, was designed so that its minimization allows to reach the desired final energy and minimize the energy losses. The performance measure function here becomes:

$$J = h_1\left(W_{GEN} - W_{ref}\right)^2 + h_2(W_{loss})^2 \tag{5.1}$$

where h_1 is the weight used to lead the algorithm to reach the desired final energy, and h_2 is the weight used to minimize the energy losses in the system. W_{ref} and W_{GEN} are reference and the output energy of the generator and W_{loss} is the energy loss of the overall system. The equations that describe the dynamics of the system are:

$$J_m \frac{\partial \omega_m}{\partial t} = \tau_{ENG} - \tau_{GEN} - B_m \omega_m \tag{5.2}$$

$$\frac{\partial W_{GEN}}{\partial t} = \tau_{GEN} \omega_m \eta_{GEN} \tag{5.3}$$

$$\begin{aligned} \frac{\partial W_{loss}}{\partial t} &= \tau_{GEN} \omega_m \left(1 - \eta_{GEN}\right) \\ &\quad + \tau_{ENG}\, \omega_m \, \left(1/\eta_{ENG} - 1\right) + B_m \omega_m^2 \end{aligned} \tag{5.4}$$

with the initial conditions:

$$\omega_m\left(t_i\right) = \omega_{m-t0}, \quad W_{GEN}\left(t_i\right) = 0, \quad W_{loss}\ \left(t_i\right) = 0 \tag{5.5}$$

where J_m is the inertia of the system, ω_m is the mechanical speed, τ_{ENG} is the engine torque at the shaft, τ_{GEN} is the counter torque of the generator and B_m is

the viscous friction coefficient. η_{ENG} and η_{GEN} are the efficiencies of engine and and generator respectively. The state equations (5.2) to (5.5) are rearranged as:

$$\begin{aligned}
\frac{\partial x(t)}{\partial t} &= \begin{bmatrix} a_1 \\ a_2 \\ a_3 \end{bmatrix} \\
a_1 &= \frac{\tau_{ENG}}{J_m} - \frac{\tau_{GEN}}{J_m} - \frac{B_m \omega_m}{J_m} \\
a_2 &= \tau_{GEN} \omega_m \eta_{GEN} \\
a_3 &= B_m \omega_m^2 + \tau_{GEN} \omega_m \left(1 - \eta_{GEN}\right) \\
&\quad + \tau_{ENG} \omega_m \left(1/\eta_{ENG} - 1\right)
\end{aligned} \tag{5.6}$$

with the state $x(t) = [\omega_m, W_{GEN}, W_{loss}]^T$ and the control input $u(t) = [\tau_{GEN}, \tau_{ENG}]^T$. The Hamiltonian is:

$$\begin{aligned}
\mathcal{H} &= h_1 \left(W_{GEN} - W_{ref}\right)^2 \\
&\quad + h_2 (W_{loss})^2 + P(t)^T \begin{bmatrix} a_1 \\ a_2 \\ a_3 \end{bmatrix}
\end{aligned} \tag{5.7}$$

The costate function is calculated by solving equation(5.8) with the final condition (5.9):

$$\dot{P}(t) = - \begin{bmatrix} \frac{\partial a_1}{\partial \omega_m} & \frac{\partial a_2}{\partial \omega_m} & \frac{\partial a_3}{\partial \omega_m} \\ 0 & 0 & 0 \\ 0 & 0 & 0 \end{bmatrix} P(t) \tag{5.8}$$

$$
\begin{aligned}
\frac{\partial a_1}{\partial \omega_m} &= -\frac{B_m}{J_m} \\
\frac{\partial a_2}{\partial \omega_m} &= \tau_{GEN}\eta_{GEN} + \tau_{GEN}\omega_m \frac{\partial \eta_{GEN}}{\partial \omega_m} \\
\frac{\partial a_3}{\partial \omega_m} &= \tau_{GEN}\left(1 - \eta_{GEN} - \omega_m \frac{\partial \eta_{GEN}}{\partial \omega_m}\right) + 2B_m\omega_m \\
&\quad + \tau_{ENG}\left(\frac{1}{\eta_{ENG}} - 1 - \frac{\omega_m}{\eta_{ENG}^2}\frac{\partial \eta_{ENG}}{\partial \omega_m}\right)
\end{aligned}
$$

$$
P_{tf} = \begin{bmatrix} 0 \\ 2h_1\left(W_{GEN} - W_{ref}\right) \\ 2h_2 W_{loss} \end{bmatrix} \tag{5.9}
$$

Equation (2.7) becomes:

$$
0 = \begin{bmatrix} \frac{\partial a_1}{\partial \tau_{ENG}} & 0 & \frac{\partial a_3}{\partial \tau_{ENG}} \\ \frac{\partial a_1}{\partial \tau_{GEN}} & \frac{\partial a_2}{\partial \tau_{GEN}} & \frac{\partial a_3}{\partial \tau_{GEN}} \end{bmatrix} P(t)
$$

$$
\begin{aligned}
\frac{\partial a_1}{\partial \tau_{ENG}} &= \frac{1}{J_m} \\
\frac{\partial a_3}{\partial \tau_{ENG}} &= \omega_m\left(\frac{1}{\eta_{ENG}} - 1 - \frac{\tau_{ENG}}{\eta_{ENG}^2}\frac{\partial \eta_{ENG}}{\partial \tau_{ENG}}\right) \\
\frac{\partial a_1}{\partial \tau_{GEN}} &= -\frac{1}{J_m} \\
\frac{\partial a_2}{\partial \tau_{GEN}} &= \omega_m\left(\eta_{GEN} + \tau_{GEN}\frac{\partial \eta_{GEN}}{\partial \tau_{GEN}}\right) \\
\frac{\partial a_3}{\partial \tau_{GEN}} &= \omega_m\left(1 - \eta_{GEN} - \tau_{GEN}\frac{\partial \eta_{GEN}}{\partial \tau_{GEN}}\right)
\end{aligned} \tag{5.10}
$$

5.3.2 Numerical Optimization

Subsection 5.3.1 presented the continuous time optimization. This section presents the solution of the problem in discrete time. Since the information of the engine

losses and generator losses is usually given in lookup tables, this section presents a procedure to implement the numerical differentiation required for some calculations.

First we rewrite equations (5.6) and (5.8) in discrete time as:

$$\begin{bmatrix} \omega_m^{i+1} \\ W_{GEN}^{i+1} \\ W_{loss}^{i+1} \end{bmatrix} = \begin{bmatrix} a_1^i \\ a_2^i \\ a_3^i \end{bmatrix} \Delta t + \begin{bmatrix} \omega_m^i \\ W_{GEN}^i \\ W_{loss}^i \end{bmatrix} \tag{5.11}$$

$$P^{i-1} = \begin{bmatrix} \frac{\partial a_1^i}{\partial \omega_m^i}\Delta t + 1 & \frac{\partial a_2^i}{\partial \omega_m^i}\Delta t & \frac{\partial a_3^i}{\partial \omega_m^i}\Delta t \\ 0 & 1 & 0 \\ 0 & 0 & 1 \end{bmatrix} P^i$$

$$\begin{aligned} \frac{\partial a_1^i}{\partial \omega_m^i} &= -\frac{B_m}{J_m} \\ \frac{\partial a_2^i}{\partial \omega_m^i} &= \tau_{GEN}^i \eta_{GEN}^i + \tau_{GEN}^i \omega_m^i \frac{\partial \eta_{GEN}^i}{\partial \omega_m^i} \\ \frac{\partial a_3^i}{\partial \omega_m^i} &= \tau_{GEN}^i \left(1 - \eta_{GEN}^i - \omega_m^i \frac{\partial \eta_{GEN}^i}{\partial \omega_m^i}\right) + 2B_m \omega_m^i \\ &\quad + \tau_{ENG}^i \left(\frac{1}{\eta_{ENG}^i} - 1 - \frac{\omega_m^i}{\eta_{ENG}^{i,2}} \frac{\partial \eta_{ENG}^i}{\partial \omega_m^i}\right) \end{aligned} \tag{5.12}$$

where Δt is the sampling time, and i is the sample number. When the losses are stored as lookup tables, the values of $\eta_{ENG}^i\left(\omega_m^i, \tau_{ENG}^i\right)$ and $\eta_{GEN}^i\left(\omega_m^i, \tau_{GEN}^i\right)$ are calculated using a bilinear interpolation summarized in equation(5.13):

$$\begin{aligned} \eta(\omega,\tau) \approx & \frac{\eta(\omega_1,\tau_1)}{\Delta\omega\Delta\tau}(\omega_2-\omega)(\tau_2-\tau) + \frac{\eta(\omega_2,\tau_1)}{\Delta\omega\Delta\tau}(\omega-\omega_1)(\tau_2-\tau) \\ & + \frac{\eta(\omega_1,\tau_2)}{\Delta\omega\Delta\tau}(\omega_2-\omega)(\tau-\tau_1) + \frac{\eta(\omega_2,\tau_2)}{\Delta\omega\Delta\tau}(\omega-\omega_1)(\tau-\tau_1) \end{aligned} \tag{5.13}$$

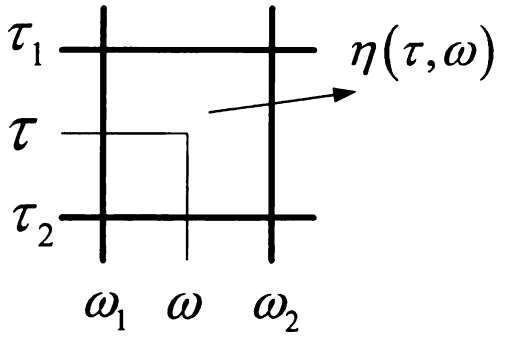

Figure 5.4: Grid data example used to describe the bilinear interpolation

with $\Delta\omega = \omega_2 - \omega_1$ and $\Delta\tau = \tau_2 - \tau_1$. The values of $\partial\eta^i_{ENG}\left(\omega^i_m, \tau^i_{ENG}\right)/\partial\omega^i_m$ and $\partial\eta^i_{GEN}\left(\omega^i_m, \tau^i_{GEN}\right)/\partial\omega^i_m$ are calculated numerically in (5.14):

$$\begin{aligned}
\eta(\omega_1,\tau) &\approx \frac{\eta(\omega_1,\tau_2)-\eta(\omega_1,\tau_1)}{\tau_2-\tau_1}(\tau-\tau_1)+\eta(\omega_1,\tau_1)\\
\eta(\omega_2,\tau) &\approx \frac{\eta(\omega_2,\tau_2)-\eta(\omega_2,\tau_1)}{\tau_2-\tau_1}(\tau-\tau_1)+\eta(\omega_2,\tau_1)\\
\frac{\partial\eta(\omega,\tau)}{\partial\omega} &\approx \frac{\eta(\omega_2,\tau)-\eta(\omega_1,\tau)}{\Delta\omega}
\end{aligned} \tag{5.14}$$

The control function is calculated iteratively, which leads to the iterative minimization of the performance measure function. The steepest descent method [29] determines the updated value of the control function iteratively by modifying condition of equation (2.15):

$$u(t)^{l+1} = u(t)^l - \tau_{adap}\frac{\partial\mathcal{H}(x(t),u(t)^l,P(t))}{\partial u(t)^l} \tag{5.15}$$

where l is the iteration number and τ_{adap} is the adaptation constant that defines the convergence rate of the minimization algorithm. Equation (5.10) can be substituted in (5.15) and discretized as (5.16).

$$\begin{bmatrix} \tau_{ENG}^{i,l+1} \\ \tau_{GEN}^{i,l+1} \end{bmatrix} = -\tau_{adap} \begin{bmatrix} \frac{\partial a_1^i}{\partial \tau_{ENG}^i} & 0 & \frac{\partial a_3^i}{\partial \tau_{ENG}^i} \\ \frac{\partial a_1^i}{\partial \tau_{GEN}^i} & \frac{\partial a_2^i}{\partial \tau_{GEN}^i} & \frac{\partial a_3^i}{\partial \tau_{GEN}^i} \end{bmatrix} P^i + \begin{bmatrix} \tau_{ENG}^{i,l} \\ \tau_{GEN}^{i,l} \end{bmatrix}$$

$$\begin{aligned} \frac{\partial a_1^i}{\partial \tau_{ENG}^i} &= \frac{1}{J_m} \\ \frac{\partial a_3^i}{\partial \tau_{ENG}^i} &= \omega_m^i \left(\frac{1}{\eta_{ENG}^i} - 1 - \frac{\tau_{ENG}^i}{\eta_{ENG}^{i,2}} \frac{\partial \eta_{ENG}^i}{\partial \tau_{ENG}^i} \right) \\ \frac{\partial a_1^i}{\partial \tau_{GEN}^i} &= -\frac{1}{J_m} \\ \frac{\partial a_2^i}{\partial \tau_{GEN}^i} &= \omega_m^i \left(\eta_{ENG}^i + \tau_{GEN}^i \frac{\partial \eta_{ENG}^i}{\partial \tau_{GEN}^i} \right) \\ \frac{\partial a_3^i}{\partial \tau_{GEN}^i} &= \omega_m^i \left(1 - \eta_{GEN}^i - \tau_{GEN}^i \frac{\partial \eta_{GEN}^i}{\partial \tau_{GEN}^i} \right) \end{aligned} \tag{5.16}$$

The values of $\partial \eta_{ENG}^i \left(\omega_m^i, \tau_{ENG}^i \right) / \partial \tau_{ENG}^i$ and $\partial \eta_{GEN}^i \left(\omega_m^i, \tau_{GEN}^i \right) / \partial \tau_{GEN}^i$ are calculated numerically by equation (5.17):

$$\begin{aligned} \eta(\omega, \tau_1) &\approx \frac{\eta(\omega_2, \tau_1) - \eta(\omega_1, \tau_1)}{\omega_2 - \omega_1} (\omega - \omega_1) + \eta(\omega_1, \tau_1) \\ \eta(\omega, \tau_2) &\approx \frac{\eta(\omega_2, \tau_2) - \eta(\omega_1, \tau_2)}{\omega_2 - \omega_1} (\omega - \omega_1) + \eta(\omega_1, \tau_2) \\ \frac{\partial \eta(\omega, \tau)}{\partial \tau} &\approx \frac{\eta(\omega, \tau_2) - \eta(\omega, \tau_1)}{\Delta \tau} \end{aligned} \tag{5.17}$$

The calculation of the updated control function equation (5.16) may produce

values of $\tau_{GEN}^{i,l+1}$ or $\tau_{ENG}^{i,l+1}$ outside the intervals $0 < \tau_{ENG}^{i,l+1} < \tau_{ENG-\max}^{i,l+1}\left(\omega^i\right)$ and $0 < \tau_{GEN}^{i,l+1} < \tau_{GEN-\max}^{i,l+1}\left(\omega^i\right)$ with $i = 1...N_{tf}$. In order to to keep them within these intervals, saturation blocks were used, as shown in equations (5.18) and (5.19). In addition, if (5.11) produces a value of ω_m^{i+1} above the upper limit, $\tau_{ENG}^{i,l}$ is decreased by K_{GEN} and $\tau_{GEN}^{i,l}$ is increased by K_{GEN}. A similar procedure is used if ω_m^{i+1} has a value below the lower limit, but in this case K_{GEN} is replaced by $-K_{GEN}$. Figure 5.5 summarizes the optimization algorithm.

$$\tau_{ENG}^{i} = \begin{cases} If \quad \tau_{ENG}^{i} > \tau_{ENG-\max}\left(\omega_m^i\right) \\ \quad \tau_{ENG}^{i} = \tau_{ENG-\max}\left(\omega_m^i\right) \\ If \quad \tau_{ENG}^{i} < \tau_{ENG-\min}\left(\omega_m^i\right) \\ \quad \tau_{ENG}^{i} = \tau_{ENG-\min}\left(\omega_m^i\right) \\ otherwise \quad \tau_{ENG}^{i} = \tau_{ENG}^{i} \end{cases} \tag{5.18}$$

$$\tau_{GEN}^{i} = \begin{cases} If \quad \tau_{GEN}^{i} > \tau_{GEN-\max}\left(\omega_m^i\right) \\ \quad \tau_{GEN}^{i} = \tau_{GEN-\max}\left(\omega_m^i\right) \\ If \quad \tau_{GEN}^{i} < \tau_{GEN-\min}\left(\omega_m^i\right) \\ \quad \tau_{GEN}^{i} = \tau_{GEN-\min}\left(\omega_m^i\right) \\ otherwise \quad \tau_{GEN}^{i} = \tau_{GEN}^{i} \end{cases} \tag{5.19}$$

$$\begin{aligned} &If \quad \omega_m^i > \omega_{\max} \\ &\tau_{GEN}^{i-1} = \tau_{GEN}^{i-1} + \mathrm{K}_{GEN}, \quad \tau_{ENG}^{i-1} = \tau_{ENG}^{i-1} - \mathrm{K}_{ENG} \\ &If \quad \omega_m^i < \omega_{\min} \\ &\tau_{GEN}^{i-1} = \tau_{GEN}^{i-1} - \mathrm{K}_{GEN}, \quad \tau_{ENG}^{i-1} = \tau_{ENG}^{i-1} + \mathrm{K}_{ENG} \end{aligned} \tag{5.20}$$

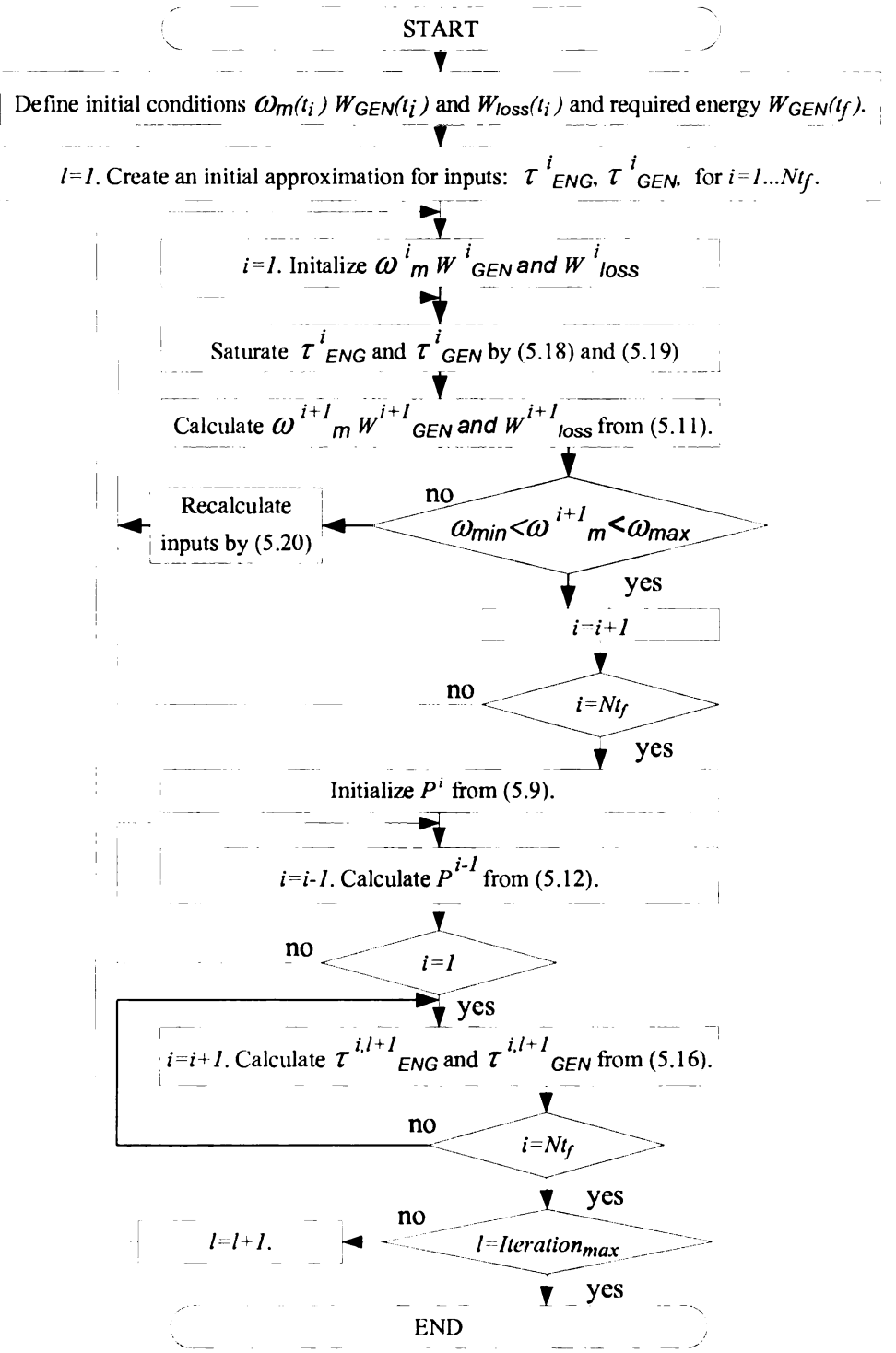

Figure 5.5: Minimization algorithm

5.3.3 Simulation Results

The proposed algorithm was applied for the operational conditions and parameters specified in Table 5.1. The optimal trajectory was calculated iteratively; the cost function was plotted against the iteration number for $\omega_m(t_i) = 1800\ r/min$, Figure 5.6. The calculated cost function of Figure 5.6 shows the convergence of the algorithm.

Table 5.1: Simulation parameters

Parameter	Value	Units
Required energy W_{ref}	4.5e5	$Joules$
Maximum speed ω_{max}	2200	r/min
Minimum speed ω_{min}	1100	r/min
Inertia J_m	3.1	kgm^2
Viscous coefficient B_m	0.0043	Nms
$h1$	1000	
$h2$	30	
Sample time Δt	0.1	s
Final time tf	6	s
$iteration_{max}$	2000	
τ_{adap}	85e-012	

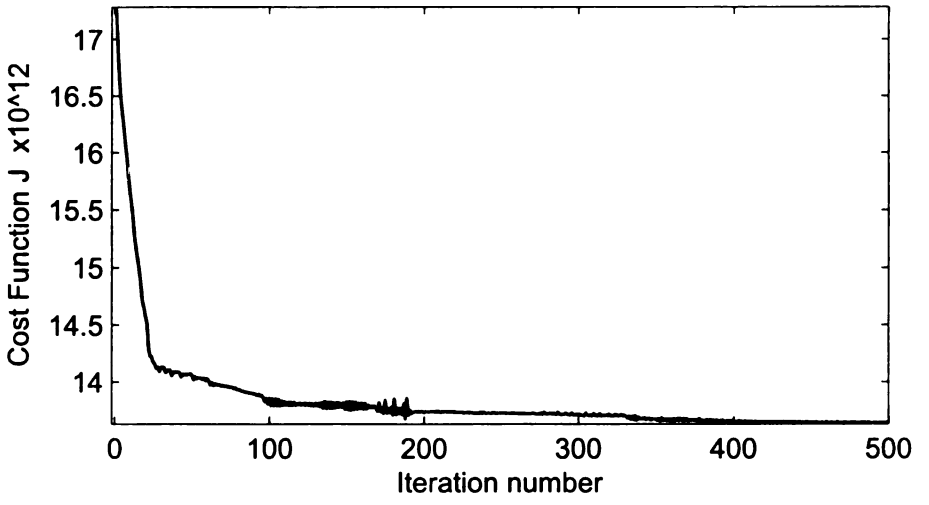

Figure 5.6: Cost Function

The final calculated functions of control inputs τ_{ENG} and τ_{GEN}, and the outputs

ω_m, W_{GEN} and W_{loss} are presented in Figure 5.7, Figure 5.8, Figure 5.9, Figure 5.10 and Figure 5.11. The simulations show the results for two initial conditions $\omega_m(t_i) = 1100\ r/min$ and $\omega_m(t_i) = 1800\ r/min$. The speed was kept within the predefined limits and the generator energy requirement was satisfied.

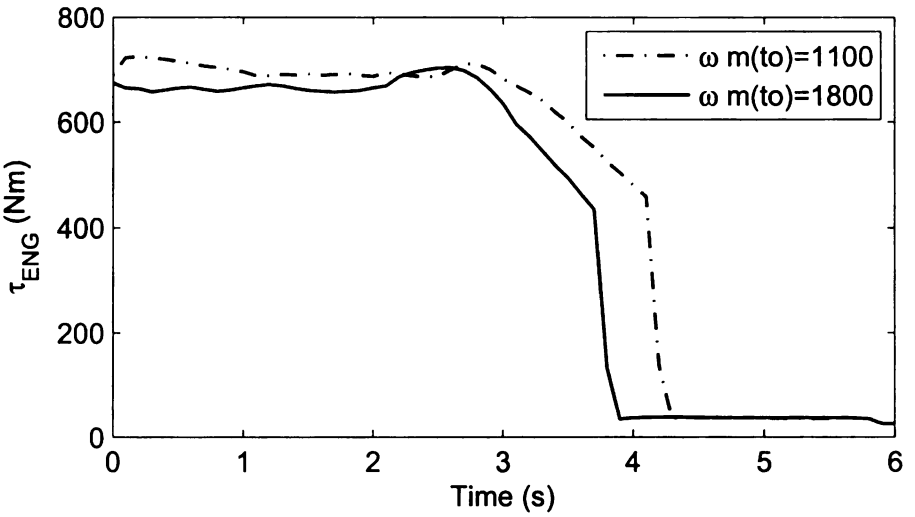

Figure 5.7: Engine torque

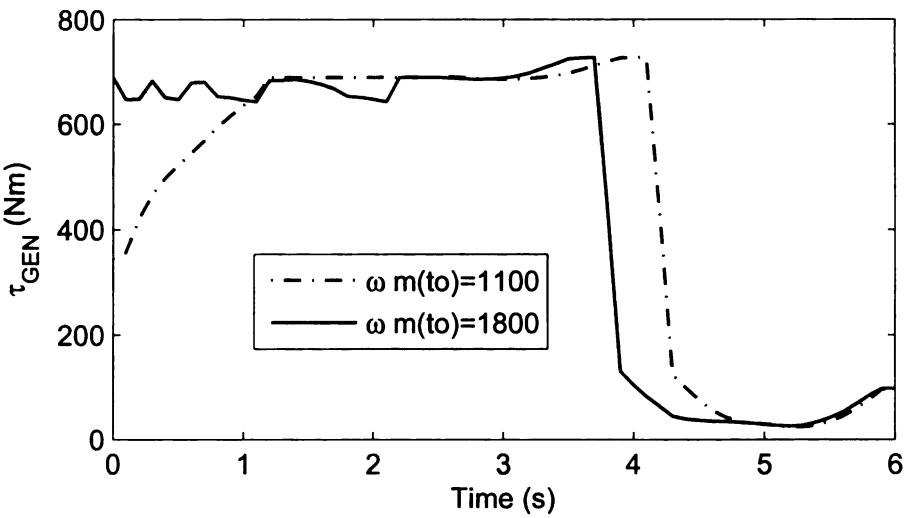

Figure 5.8: Generator torque

The torque and speed points of engine ○ and generator • were plotted over

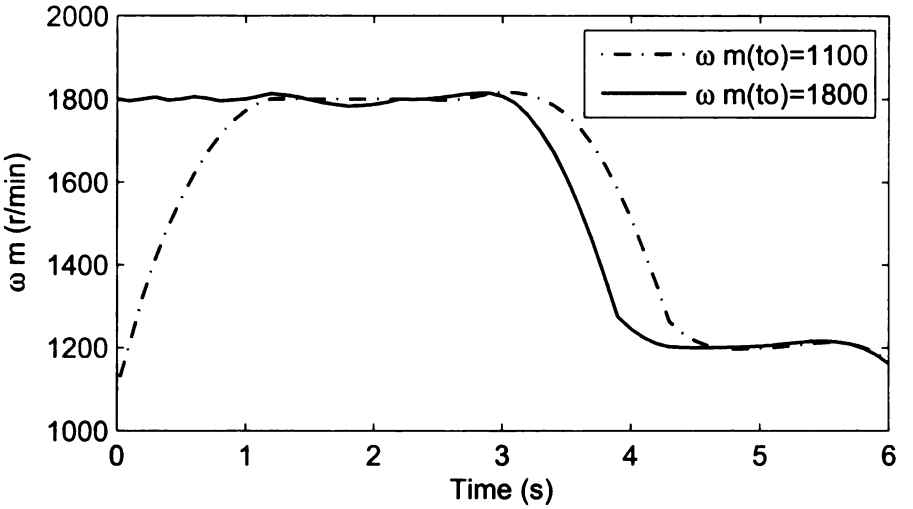

Figure 5.9: Mechanical speed

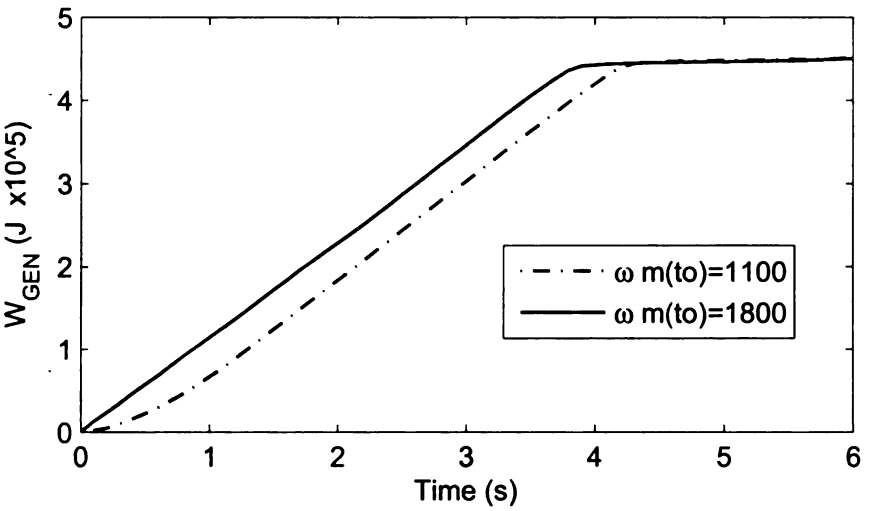

Figure 5.10: Generator output energy

the combined efficiency contours of engine-generator subsystem in Figure 5.12 for $\omega_m(ti) = 1100$. Engine and generator torque were kept within their limits, were the combined maximum torque is presented by a solid bold line. The maximum combined efficiency is $\eta = 38.8\%$ which corresponds to $\tau = 690\ Nm$ and $\omega = 1800\ r/min$. This means when the subsystem operates at its optimal condition, the maximum possible efficiency is 38.8%. As shown in Figures 5.7 to 5.12 the subsystem moves to the point

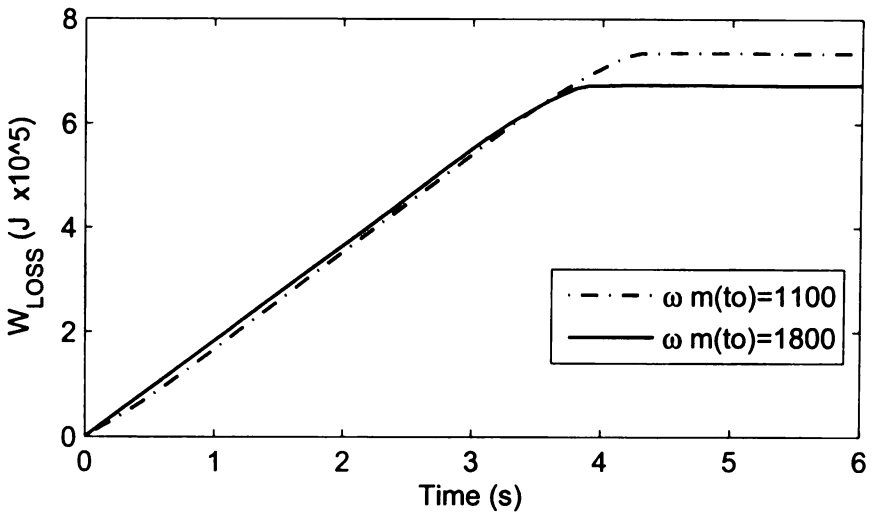

Figure 5.11: Total energy losses

of highest efficiency, and stays there until it satisfies the energy requirement. Then it moves to a point with low torque and speed to minimize the losses in the remaining time.

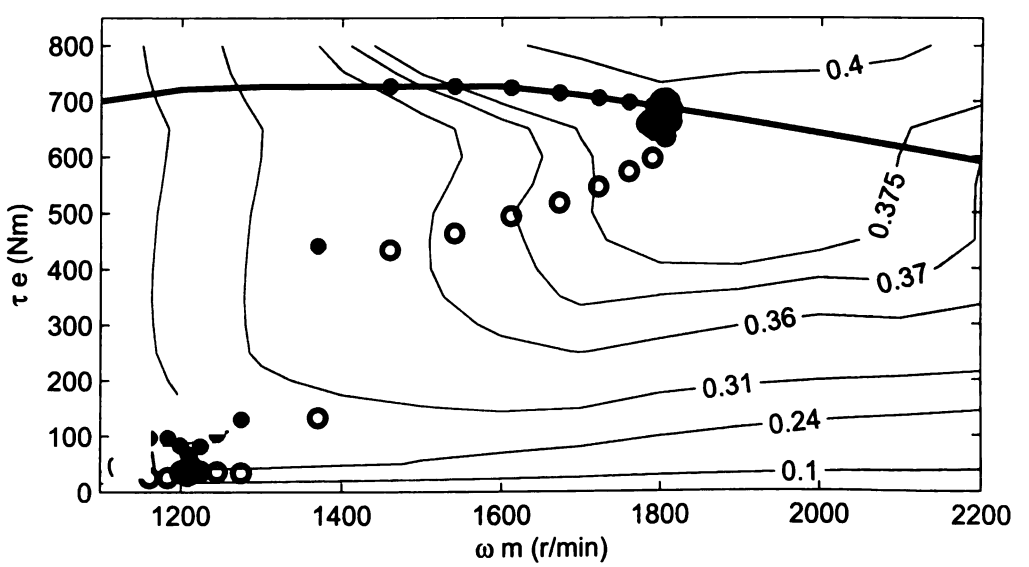

Figure 5.12: Torque-speed points over combined efficiency map contours: engine points o and generator points •

5.4 Approximation to Optimal Trajectory

The previous section described the algorithm to determine the optimal trajectory of the engine-generator subsystem. In this section an approximation to the optimal trajectory is presented that can be used in real time. Three possible operation modes were identified and a controller command for each one is proposed; these three operation modes are defined by the requested energy and time.

- Mode 1: Low energy requirement with enough time to produce it optimally. This operation will be the most common operation. The subsystem has plenty of time to reach the most efficient point $\hat{P} = \hat{\tau} * \hat{\omega}$, produce the requested energy, and then go to a point with minimum speed and torque and hence low losses.

- Mode 2: High energy requirement with enough time to produce it. The system has enough time to produce the requested energy, but not enough to produce it by operating at the most efficient point. A point corresponding to higher power with lower efficiency than the optimal is determined. The system will operate at this point and keep there to produce the requested energy.

- Mode 3: Fast energy production. This operation will be the least common operation, the system is required to produce energy in a short period of time. Under this condition the energy optimization is not the most important criterion to operate the subsystem. The system is free to speed up by imposing maximum torque in engine and generator (when maximum engine torque is higher than the generator torque).

5.4.1 Mode 1: Low Energy Requirement With Enough Time

This common operation mode is based entirely in the trajectory optimization results presented in the previous section. Let us summarize the behavior of the optimization

as follows:

- The trajectory starts from initial speed, the subsystem speeds up until it reaches the point of maximum efficiency.
- The subsystem stays at this most efficient point to supply almost all the required energy.
- The subsystem slows down to produce minimal losses.
- Torque of the generator follows the speed profile to produce the required energy.
- Torque of the engine is varied to allow the subsystem to speed up, keep the system at the optimal point, and then slow down.
- Acceleration and deceleration times are kept constant, moreover torque and speed trajectory during the transients are the same for different energy requirements and final time values.

These conditions were used to develop an approximation to the optimal trajectory. For the system presented in the previous section, the final time and energy requirement should satisfy the following conditions:

1. $t_f \geq 2\ s$: final time should be greater than the time required to accelerate from any initial speed to the most efficient point plus the time required to decelerate from the most efficient point to a point with minimum speed and torque.
2. $W_{ref} \geq 1e5\ J$: final energy should be greater than the energy produced during the acceleration and deceleration described in the previous item.
3. $t_f \geq (W_{ref} - 2e5)/\hat{P} + 1\ s$. This condition ensures that the system can provide the energy while operating at the most efficient power point "$\hat{P} = \hat{\tau}\hat{\omega}$", where $\hat{\tau} = 690\ Nm$, $\hat{\omega} = 1800\ r/min$ and $\hat{P} = 130\ kW$.

When the previous conditions are satisfied, engine-generator speed and generator torque can be approximated by trapezoidal functions as shown in Figures 5.7 to 5.9. The trapezoidal function and its time dependence is shown in equation (5.21). A low pass filter is used to smooth the trapezoidal function as shown in equation (5.22).

$$x_{trap}(t) = \begin{cases} 0 \le t \le t_1 & \frac{x_{opt}-x_0}{t_1} t \\ t_1 \le t \le t_2 & x_{opt} \\ t_2 \le t \le t_3 & \frac{x_{opt}-x_0}{t_2-t_3}(t-t_2) + x_{opt} \\ t_3 \le t \le t_f & x_{\min} \end{cases} \tag{5.21}$$

$$H(s) = \frac{1}{k_{fil}s + 1} \tag{5.22}$$

The time intervals and the gains for the trapezoidal functions and filters are summarized in table 5.2. The block diagram of the approximated optimal trajectory is shown in Figure 5.13.

Table 5.2: Parameters of the approximated optimal trajectory

Parameter	$\omega_{ref}(t)$	$\tau_{ref}(t)$
t_1	$0.3\ s$	$0.7\ s$
$t_2 - t_1$	$3.3 + 1.7\left(\frac{W_{ref}}{2e5} - 2.25\right)$	$3.1 + 1.7\left(\frac{W_{ref}}{2e5} - 2.25\right)$
$t_3 - t_2$	$0.9\ s$	$0.7\ s$
x_{opt}	$1800\ r/min$	$690\ Nm$
x_{min}	$1100\ r/min$	$0\ Nm$
k_{fil}	0.0429	0.0538

5.4.2 Mode 2: High Energy Requirement With Enough Time

This mode occurs when the first two conditions of Mode 1 of subsection 5.4.1 are satisfied, but the last one is not, i.e. $t_f \ge 2\ s$, $W_{ref} \ge 10^5\ J$ and $t_f \le (W_{ref} - 2 \cdot 10^5)/P^* + 1\ s$. We assume that the requested energy can be produced by operating

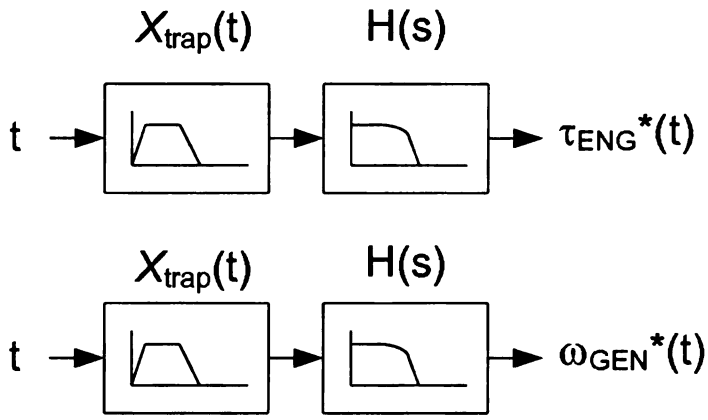

Figure 5.13: Block diagram of approximated optimal trajectory

the subsystem at one point ($\bar{P} \neq \hat{P}$) for the specified time (otherwise the energy command is wrong and it should be adjusted as $W_{ref} = P_{max} * t_f$). The power point $\bar{P}$ of operation can be determined by a local optimization as described in [40]. The procedure to determine $\bar{P}$ and the torque and speed commands is summarized below.

- The energy command and final time allowed to determine the required power as $\bar{P} = W_{ref}/t_f$.
- The values of $\bar{\tau}$ and $\bar{\omega}$ ($\bar{P} = \bar{\tau} * \bar{\omega}$) are determined by searching among the torque-speed points that satisfy the power requirement $\bar{P}$ and selecting the combination that produces the lowest losses.
- $\bar{\tau}$ and $\bar{\omega}$ are used as a references for torque and speed controller in the engine-generator subsystem.

5.4.3 Mode 3: Fast Energy Production

This mode of operation is the least common; it occurs when the first two conditions Mode 1 are not satisfied, i.e. the energy needs to be produced in a short period of time, and hence the efficiency is not the main criterion to determine the controller

references. This operation model is difficult to determine because the energy vs time relationship is more complex than in modes 1 or 2. The transients in engine and generator should be synchronized to properly follow a specified profile. A simple controller is proposed:

- When the maximum torque that the engine can provide is higher than the maximum counter torque of the generator, torques are commanded to their maximum values, allowing the production of power from the beginning. This allows the system to speed up.

- When the maximum engine torque is lower than the maximum torque of the generator, the engine torque is commanded to its maximum value and the generator torque is commanded to a value 10% less than the one from the engine. This strategy allows production of power from the beginning, and allows the system to speed up.

- When the maximum speed is achieved, engine and generator torque commands are set to be equal. Both torque commands are set to the minimum of the maximum engine torque and the maximum generator torque.

5.5 Comparison

This section presents a comparison between two classical control strategies [40, 41] and the optimal trajectory and the approximated optimal trajectory proposed here.

The main purpose of the optimization algorithm is to provide the requested energy while maximizing efficiency. Generally, initial and final speeds are not the same, therefore the kinetic energy stored in the engine-generator rotational inertia changes, which affects the efficiency calculation. The efficiency formula used in this paper

compensates for this change in speed as follows:

$$\eta = \frac{W_{GEN} - 0.5Jm\left(\omega_{m-t0}^2 - \omega_{m-tf}^2\right)}{W_{GEN} - 0.5Jm\left(\omega_{m-t0}^2 - \omega_{m-tf}^2\right) + W_{loss}} \tag{5.23}$$

The two classical control strategies are summarized below:

- The first control strategy of "constant power" proposed by Ceraolo *et al.* [40] determines the torque and speed references by the procedure summarized in "Mode 2" but it is used for all power values (higher and lower than the power at the most efficient point).

- The second control strategy ,"ON-OFF" proposed by Barsali *et al.* [41], proposes to turn on and off the engine-generator subsystem according to the energy and/or power requirement. This control method requires to speed up and down the subsystem in zero time, which is not possible. This concept is adapted here to analyze the losses during the transient. To achieve the "ON-OFF" operation, the system will be kept at constant speed with a value equal to $\omega = \omega_{opt}$. The generator will operate at $\tau_{hi} = \tau_{opt}$ for time t_{hi} to produce the requested energy, and for the remaining time, t_{lo}, it operates at $\tau_{lo} = 40Nm$ to produce low losses.

Four control methods were compared. Tables 5.3 and 5.4 summarize the simulation results of the controllers with the same initial speeds $\omega_{m-t0} = 1100\ r/min$ and $\omega_{m-t0} = 1800\ r/min$ and final fixed time $t_f = 6\ s$. The engine was operated in speed mode and the generator in torque mode. The PI speed controller of the engine had $K_p = 45$ and $K_i = 100$. The approximate optimal trajectory operates in mode 1 for the first 6 cases and in mode 2 for the last case. Neither of the controllers were tested in mode 3 due to the fact that there are not an adequate criteria to make a fair comparison between them.

The proposed optimal trajectory shows better efficiency than the other methods in almost all conditions, Table 5.3. For $\omega_{m-t0} = 1800\ r/min$ and $W_{ref} = 7.4e5\ J$ the proposed method had a lower efficiency, but this was due to the fact that the non-optimized methods produced less energy. The approximate optimal trajectory has an efficiency comparable to the efficiency of the optimal trajectory and better that the two classical control strategies. The two proposed controllers satisfy the energy requirements as shown in Table 5.4, which is the main objective of the optimization.

Table 5.3: Controllers comparison, Efficiency

ω_{m-t0}	W_{ref}	Control Strategy			
		ON OFF	Const. Power	Proposed Method	Proposed Approx. Method
1100	2.50E+05	0.342	0.364	0.379	0.377
	4.50E+05	0.350	0.374	0.382	0.382
	6.50E+05	0.350	0.364	0.384	0.384
1800	2.50E+05	0.347	0.360	0.381	0.377
	4.50E+05	0.375	0.376	0.384	0.380
	6.50E+05	0.384	0.381	0.385	0.383
	7.40E+05	0.385	0.388	0.378	0.388

Table 5.4: Controller comparison, normalized final energy W_{tf}/W_{ref}

ω_{m-t0}	W_{ref}	Control Strategy			
		ON OFF	Const. Power	Proposed Method	Proposed Approx. Method
1100	2.50E+05	1.730	0.998	0.998	0.988
	4.50E+05	1.257	1.001	1.003	1.002
	6.50E+05	0.880	0.944	0.991	1.000
1800	2.50E+05	1.078	1.005	1.004	0.996
	4.50E+05	0.986	1.009	1.005	1.004
	6.50E+05	0.950	0.996	1.002	1.003
	7.40E+05	0.908	0.962	0.980	0.962

Chapter 6

High Performance Low Speed Sensorless Control of Interior Permanent Magnet Synchronous Motor

The work presented in this chapter deals with the issues in practical implementation of high-frequency injection methods to control IPMSM's without shaft position sensors. Implementing a high-frequency injection technique for rotor position estimation requires intense signal processing of the measured currents, as well as filtering of the signals to extract the rotor position information. These tasks complicate the control algorithm, but more importantly degrade the overall system performance by introducing delays, increasing response times and decreasing the bandwidth of the controller. Moreover, some specific filtering techniques limit the operation of the machine to a very narrow range. These issues and their specific effects are discussed in this chapter, and mitigation procedures are proposed, implemented and verified through the experimental setups. Experimental results of a new high-performance

controller without rotor position sensors are presented as well. The major contribution of this chapter is a new controller based on the high-frequency injection method that eliminates the need for low-pass filtering and improves the performance of the machine.

6.1 Introduction

Rotor position information is necessary for Field Oriented Control (FOC) of Permanent Magnet Synchronous Machines. Rotor position sensing requires resolvers or encoders, an alternative is to operate the machine without shaft sensors. Back EMF methods are preferred at higher speed operation [42, 43, 44], while Pulse Width Modulation(PWM) analysis [45, 46] and high frequency injection methods [47, 48, 49] have been used for low speed operation.

Juliet and Holtz [45] investigated measuring the di/dt in the phase currents resulting from the PWM modulation so no additional signal injection is required, however, as they noted, measuring the di/dt is very difficult and almost unfeasible for the implementation beyond laboratory setup.

High frequency injection of current or voltage has inherent problems related to decoupling the injected signals and the power component signals, one used for the rotor position estimation and the other to control the machine torque respectively. The selection of filters and their parameter change significantly the motor performance [50]. The most common method of post-processing the signal obtained through the high-frequency injection is by using Synchronous Reference Frame Filters (SRFF's) [50]. They can remove a specific frequency, such as the injected frequency. The spectrum location of the resultant high frequency current (or voltage) depends on the frequency of the applied high frequency voltage (or current) and the electrical speed, which is unknown. Then, in the synchronous frame of reference the spectrum of the

resultant current (or voltage) is located at low frequency, requiring a low pass filter to remove it.

A low-pass filter can be also used to isolate a given signal, but signals beyond the filter bandwidth will only be attenuated [51]. In addition, both methods will lower the overall system bandwidth. Vadstrup [52] used two cascaded Band Stop Filters (BSF's); one to remove the positive and the other to remove the negative sequence currents, which would allow the fundamental component to pass with no phase-lag if the filters have the same bandwidth. Some attenuation however is introduced, depending on the required bandwidth of the filters and the spectral separation of the carrier signal components [53]. Moreover, it is not always possible to tune the two cascaded BSF's to the same bandwidth, resulting in both phase error and attenuation at the fundamental frequency. Young-doo [54] used a square wave injection voltage to remove the Low Pass Filters (LPF's) from the rotor position estimator path, improving the observer performance, however, this methodology still requires a low pass filter in the current controller, which decreases the bandwidth of the current controller. Shinnaka [55] proposed a new injection method that includes injection in direct and quadrature axis, where the quadrature axis voltage magnitude is proportional to the speed. This modification allows the controller to increase the speed range of the controller, but BSF's and BPF's are used in the observer and controller to separate power and high frequency signals.

The issues of cross-magnetic saturation in high frequency injection methods have been presented by Zhu *et al.*[56]. They proposed mitigating the rotor position error due to saturation by calculating the value of the error angle and its dependence on the current. It is well documented that the error in the estimate of rotor position increases as a function of the load current [47]. Guglielmi *et al.* showed in [57] that an error exists in rotor position estimation due to cross-magnetic saturation between d- and q-axes. Stumberger *et al.* in [58] evaluated the effect of saturation and cross-

magnetization for IPMSM's, but offered no method for compensating for the resulting error. Boldea [59] proposed the concept of active flux, which changes the controller frame of reference and no high frequency injection is required for sensorless control at low speed. The active flux is convenient for control purposes because the machines can be controlled as if they have no saliency. The response at low speed is validated by simulations.

This chapter presents a new methodology to design a rotor position observer using high frequency injection with no filters in the current feedback loop. This simplification allows better performance of the current controller. The rotor position estimation is improved by removing the power frequency components of the signals due to the power-current control, from the high frequency signals due to injection. Experimental results are used to validate the proposed rotor position estimator and the cross saturation effect in the rotor position estimation is presented.

This chapter is organized as follows: section 6.2 is divided in two subsections. Subsection 6.2.1 shows the classical approach where low pass and high pass filters are used for current control and rotor position estimation respectively. Subsection 6.2.2 describes the proposed methodology. Section 6.3 presents and discusses experimental results, where the filtered demodulation and the proposed controller are compared.

6.2 High Frequency Injection Architectures

In this section two methodologies for rotor position estimation based on signal injection along with the required demodulation are discussed. The first methodology uses Low Pass Filters (LPF's) and High Pass Filters (HPF's) to separate power component and high frequency injected signals [60, 61]. The second methodology, proposed here, uses a high gain current observer to indirectly extract the signal components due to high frequency injection. A transfer function to analyze the effect of the high

frequency injection over the power component is presented. This transfer function and a high gain observer are used instead of adding filters in the current control loop, this modification leads to a higher performance of the current controller.

6.2.1 Filtered Controller

Several methods have been proposed for high frequency injection [62, 63]. For voltage injection, superposition is used to analyze the effect of the high frequency in the machine. High frequency and power frequency are separated with Low Pass Filters and High Pass Filters as shown in Figure 6.1.

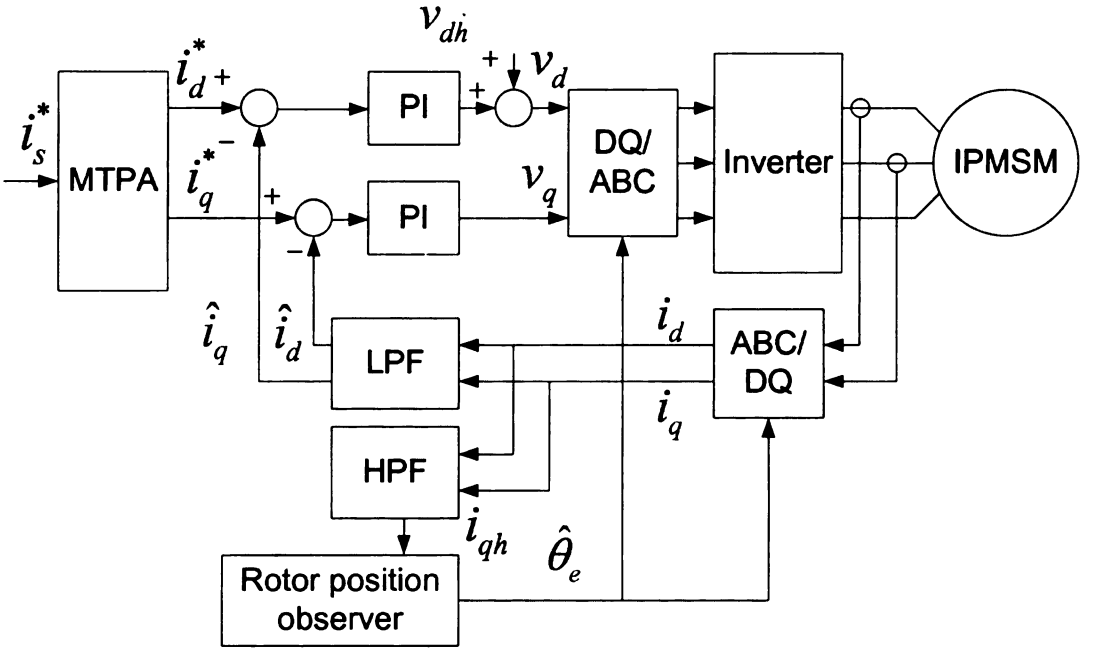

Figure 6.1: Filtered rotor position estimation block diagram

The block diagram in Figure 6.1 is composed of two basic subsystems: The power loop for the machine control, and the rotor position estimation loop. The power loop consists of two PI controllers in cascade with two low pass filters and the machine. In the power loop the low pass filter removes the high frequency content of the measured current, so that the inputs and outputs of the PI controllers are free of high frequency

content. The high frequency loop used to estimate the rotor position is described below:

Consider the simplified machine model in the rotor frame of reference as shown in equation (6.1).

$$\begin{bmatrix} v_{ds}^r \\ v_{qs}^r \end{bmatrix} = \begin{bmatrix} R_s + L_d p & -\omega_e L_q \\ \omega_e L_d & R_s + L_q p \end{bmatrix} \begin{bmatrix} i_{ds}^r \\ i_{qs}^r \end{bmatrix} + \begin{bmatrix} 0 \\ \omega_e \lambda_{d-PM} \end{bmatrix} \tag{6.1}$$

where v_{ds}^r and v_{qs}^r are the direct and quadrature axis voltages, i_{ds}^r and i_{qs}^r are the currents, L_d and L_q are the inductances, R_s is the stator resistance, λ_{d-PM} is the flux linkages due to the PM rotor flux and ω_e is the electrical speed. Based on superposition, the machine model can be simplified to analyze the effect of the injected high frequency signals as shown in equation (6.2).

$$\begin{bmatrix} v_{dsh}^r \\ v_{qsh}^r \end{bmatrix} = \begin{bmatrix} R_s + L_d p & 0 \\ 0 & R_s + L_q p \end{bmatrix} \begin{bmatrix} i_{dsh}^r \\ i_{qsh}^r \end{bmatrix} \tag{6.2}$$

For $\omega_h >> \omega_e$ the contribution of λ_{d-PM} to the voltages and currents at the injected high frequency is zero. Equation (6.2) becomes simpler for an injected signal of constant magnitude and frequency. For slower changes in the motor speed with respect to the current changes, the machine model can be approximated by a linear system with the following state space representation:

$$\begin{bmatrix} v^r_{dsh} \\ v^r_{qsh} \end{bmatrix} = \begin{bmatrix} R_s + jL_d\omega_h & 0 \\ 0 & R_s + jL_q\omega_h \end{bmatrix} \begin{bmatrix} i^r_{dsh} \\ i^r_{qsh} \end{bmatrix} \equiv \begin{bmatrix} Z_{dh} & 0 \\ 0 & Z_{qh} \end{bmatrix} \begin{bmatrix} i^r_{dsh} \\ i^r_{qsh} \end{bmatrix} \tag{6.3}$$

In operation without rotor position sensor the mechanical rotor position is not known, instead the controller uses the estimated rotor position $\hat{\theta}_e$. To analyze this operation, the motor model is rewritten in the estimated rotor frame of reference $\hat{r}$. Equation (6.3) is rewritten in this estimated rotor position frame of reference, and the transformation matrix of equation (6.4) as function of $\tilde{\theta}_e = \theta_e - \hat{\theta}_e$ is used to transfer the motor model from θ_e frame of reference to $\hat{\theta}_e$ frame of reference as shown in equation(6.5).

$$R(\tilde{\theta}_e) = \begin{bmatrix} \cos(\tilde{\theta}_e) & \sin(\tilde{\theta}_e) \\ -\sin(\tilde{\theta}_e) & \cos(\tilde{\theta}_e) \end{bmatrix} \tag{6.4}$$

$$\begin{bmatrix} v^{\hat{r}}_{dsh} \\ v^{\hat{r}}_{qsh} \end{bmatrix} = R^{-1}(\tilde{\theta}_e) \begin{bmatrix} Z_{dh} & 0 \\ 0 & Z_{qh} \end{bmatrix} R(\tilde{\theta}_e) \begin{bmatrix} i^{\hat{r}}_{dsh} \\ i^{\hat{r}}_{qsh} \end{bmatrix} = \begin{bmatrix} \bar{Z} + Z_\Delta \cos(2\tilde{\theta}_e) & Z_\Delta \sin(2\tilde{\theta}_e) \\ Z_\Delta \sin(2\tilde{\theta}_e) & \bar{Z} - Z_\Delta \cos(2\tilde{\theta}_e) \end{bmatrix} \begin{bmatrix} i^{\hat{r}}_{dsh} \\ i^{\hat{r}}_{qsh} \end{bmatrix} \tag{6.5}$$

where $Z = R_s + jL\omega_h$ and

$$\bar{Z} = \frac{Z_{dh} + Z_{qh}}{2}, Z_\Delta = \frac{Z_{dh} - Z_{qh}}{2} \tag{6.6}$$

Equation 6.6 shows that by eliminating the cross coupling terms, the error between

the estimated and the mechanical rotor position becomes zero. Voltage can be injected in the direct or in the quadrature flux axis. Direct axis voltage injection is preferred, because it produces less torque pulsations than quadrature axis voltage injection. For direct axis voltage injection the high frequency component of the voltage is:

$$\begin{bmatrix} v_{dsh}^{\hat{r}} \\ v_{qsh}^{\hat{r}} \end{bmatrix} = \begin{bmatrix} V_h \cos(\omega_h t) \\ 0 \end{bmatrix} \tag{6.7}$$

where V_h is the amplitude of the injected voltage and ω_h is the frequency of the injected signal. By substituting equation (6.7) in equation (6.6), and by neglecting the resistive component of the impedances, the quadrature axis current is written as in equation (6.8).

$$i_{qsh}^{\hat{r}} = -\frac{V_h L_\Delta \sin(\omega_h t)}{\omega_h L_d L_q} \sin(2\tilde{\theta}_e) \tag{6.8}$$

The high frequency quadrature axis current is demodulated to obtain the rotor position information as shown in Figure 6.2. A PI regulator and an integrator are used to minimize the error function $f(\tilde{\theta}_e)$ of equation (6.9), where, for smaller values of $\tilde{\theta}_e$, $sin(2\tilde{\theta}_e)$ can be approximated as $2\tilde{\theta}_e$. The minimization of $f(\tilde{\theta}_e)$ leads to the minimization of the error in the rotor position.

$$f(\tilde{\theta}_e) = \frac{V_h L_\Delta}{2\omega_h L_d L_q} \sin(2\tilde{\theta}_e) \approx K_{err} \tilde{\theta}_e \tag{6.9}$$

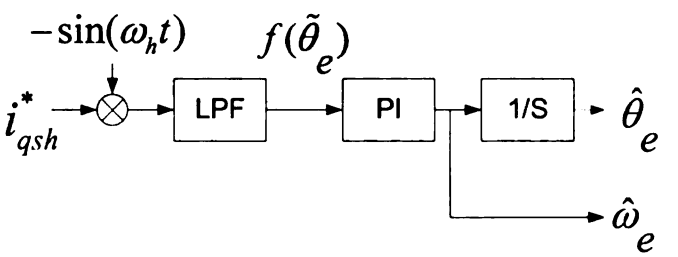

Figure 6.2: Block diagram of rotor position estimation by synchronous frame of reference filters

6.2.2 High Performance Controller

In Figure 6.1, the power component of the measured current signal is obtained by removing the high frequency by LPF's which have some inherent disadvantages: LPF's isolate a given signal, but signals outside the filter bandwidth are attenuated, i.e. the LPF's do not eliminate completely the high frequency signal. In the same manner, if the given signal has a high frequency component, these components will be attenuated and their phase will be shifted, which is undesirable. Current commands usually are composed by ramps or steps, which have high frequency content; in order to track these current commands properly, the LPF's should have a bandwidth high enough so that the signals are not attenuated, but low enough to reject the injected high frequency. To properly filter the signals, the injected frequency is selected high enough, so that the stop band of the filter does not interfere with the power component. The required voltage to produce a desired high frequency current is proportional to the injected frequency, that means that higher the frequency for injection the higher the magnitude of the injected voltage. High magnitude of voltage produces higher losses and less available voltage to manage the transients of the current controller.

In this subsection a new structure for rotor position estimation is presented. Power components and injected components are separated without the use of a LPF's and HPF's. In the current loop the LPF's are removed; that is done by designing the demodulation scheme based on the commanded high frequency voltage, which is known, rather than on the high frequency voltages and currents components at the machine terminals. This modification requires the calculation of the transfer function between commanded and applied high frequency components of the voltage. This transfer function is used to calculate the input voltage and to operate the motor within its voltage limits. For the extraction of the injected frequency components of the signals, the machine model is used to remove the power frequency components by the use of

a high gain current observer.

In the first part of the analysis the relation between the applied and the commanded high frequency voltage components is determined. Let us consider the high frequency model of the motor in steady state as shown in Figure 6.3. For direct axis voltage injection, the transfer function between the commanded high frequency voltage and the applied high frequency voltage is calculated in equation (6.10).

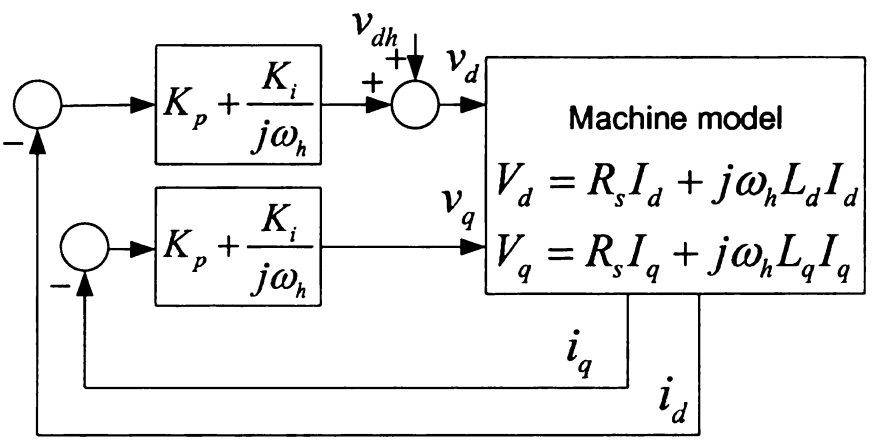

Figure 6.3: High frequency equivalent model of the motor and controller

$$\frac{v_d(\omega_h)}{v_{dh}(\omega_h)} = \frac{-\omega_h^2 L_d + j\omega_h R_s}{\left(K_i - \omega_h^2 L_d\right) + j\left(\omega_h R_s + \omega_h K_p\right)} \tag{6.10}$$

In the second part of the rotor position estimation the high frequency component of the signals due to the injection is extracted. The rotor position estimation is based on the commanded high frequency voltage v_{dh}. A high gain observer is used indirectly to determine the effect of v_{dh} on the machine signals. The high gain current observer is described below.

For a low and almost constant speed operation, the state space machine model of

equation (6.1) can be rewritten as:

$$\begin{bmatrix} \dot{i}^r_{ds} \\ \dot{i}^r_{qs} \end{bmatrix} = \begin{bmatrix} -\frac{R_s}{L_d} & \frac{\omega_e L_q}{L_d} \\ -\frac{\omega_e L_d}{L_q} & -\frac{R_s}{L_q} \end{bmatrix} \begin{bmatrix} i^r_{ds} \\ i^r_{qs} \end{bmatrix} + \begin{bmatrix} \frac{1}{L_d} & 0 & 0 \\ 0 & \frac{1}{L_q} & \frac{-\lambda_{d-PM}}{L_q} \end{bmatrix} \begin{bmatrix} v^r_{ds} \\ v^r_{qs} \\ \omega_e \end{bmatrix} \tag{6.11}$$

For rotor position detection, the high frequency commanded voltage is superimposed on the main power voltage component t give $v = v_p + v_h$, where v is the input voltage to the machine, v_p is the voltage due to the power frequency and v_h is the high frequency commanded voltage. For an injected frequency relatively close to the fundamental, the inductances L_d and L_q do not change in this operation range, and can be assumed constant. By substituting $v = v_p + v_h$, the model of equation (6.11) can be expanded as equation (6.12).

$$\begin{bmatrix} \dot{i}^r_{ds} \\ \dot{i}^r_{qs} \end{bmatrix} = \begin{bmatrix} -\frac{R_s}{L_d} & \frac{\omega_e L_q}{L_d} \\ -\frac{\omega_e L_d}{L_q} & -\frac{R_s}{L_q} \end{bmatrix} \begin{bmatrix} i^r_{ds} \\ i^r_{qs} \end{bmatrix} + \begin{bmatrix} \frac{1}{L_d} & 0 & 0 \\ 0 & \frac{1}{L_q} & \frac{-\lambda_{d-PM}}{L_q} \end{bmatrix} \begin{bmatrix} v^r_{ds-p} \\ v^r_{qs-p} \\ \omega_e \end{bmatrix} + \begin{bmatrix} \frac{1}{L_d} & 0 \\ 0 & \frac{1}{L_q} \end{bmatrix} \begin{bmatrix} v^r_{ds-h} \\ v^r_{qs-h} \end{bmatrix} \tag{6.12}$$

The system can be considered as a linear system with a disturbance, of the form:

$$\dot{x} = Ax + Bu + \delta_h \tag{6.13}$$

where $x = i_s^r$, $u = \left[v_{ds}^r, v_{qs}^r, \omega_e\right]$ and $\delta_h = v_h/L$. The disturbance will be indirectly estimated by a high gain current observer. This disturbance, δ_h, contains the information of the injected signal modulated by the rotor position. This term can be used to estimate the rotor position by the procedure described below.

The high gain current observer is of the form:

$$\begin{aligned} L(\tilde{x}) = \begin{bmatrix} l_1 \\ l_2 \end{bmatrix} = ksgn(\tilde{x}) = \begin{bmatrix} k_1 sgn(\tilde{x}_1) \\ k_2 sgn(\tilde{x}_2) \end{bmatrix} \\ where \quad \begin{aligned} \tilde{x}_1 &= (i_d - \hat{i}_d) \\ \tilde{x}_2 &= (i_q - \hat{i}_q) \end{aligned} \end{aligned} \tag{6.14}$$

where i_d and i_d are the measured values of the current and $\hat{i}_d$ and $\hat{i}_q$ are the estimated values of the current. The estimated state becomes:

$$\dot{\hat{x}} = A\hat{x} + Bu + L(\tilde{x}) \tag{6.15}$$

with

$$\dot{\tilde{x}} = A\tilde{x} + (\delta(x) - L(\tilde{x})) \tag{6.16}$$

The stability of the observer is analyzed as follows. For a positive definite function:

$$V = \frac{1}{2}\tilde{x}^T M \tilde{x} \tag{6.17}$$

with

$$M = \begin{bmatrix} \frac{1}{L_q^2} & 0 \\ 0 & \frac{1}{L_d^2} \end{bmatrix}$$

the derivative becomes

$$
\begin{aligned}
\dot{V} &= \dot{\tilde{x}}^T M \tilde{x} \\
&= \tilde{x}^T M A \tilde{x} + \tilde{x}^T M \left(\delta(x) - L(\tilde{x})\right) \\
&= \begin{bmatrix} \tilde{x}_1 & \tilde{x}_2 \end{bmatrix} \begin{bmatrix} \frac{1}{L_q^2} & 0 \\ 0 & \frac{1}{L_d^2} \end{bmatrix} \begin{bmatrix} -\frac{R_s}{L_d} & \frac{\omega_e L_q}{L_d} \\ -\frac{\omega_e L_d}{L_q} & -\frac{R_s}{L_q} \end{bmatrix} \begin{bmatrix} \tilde{x}_1 \\ \tilde{x}_2 \end{bmatrix} \\
&+ \begin{bmatrix} \tilde{x}_1 & \tilde{x}_2 \end{bmatrix} \begin{bmatrix} \frac{1}{L_q^2} & 0 \\ 0 & \frac{1}{L_d^2} \end{bmatrix} \begin{bmatrix} \delta_1 - l_1 \\ \delta_2 - l_2 \end{bmatrix} \\
&= \begin{bmatrix} \tilde{x}_1 & \tilde{x}_2 \end{bmatrix} \begin{bmatrix} -\frac{R_s}{L_d L_q^2} & \frac{\omega_e L_q}{L_d L_q^2} \\ -\frac{\omega_e L_d}{L_q L_d^2} & -\frac{R_s}{L_q L_d^2} \end{bmatrix} \begin{bmatrix} \tilde{x}_1 \\ \tilde{x}_2 \end{bmatrix} \\
&+ \frac{1}{L_q^2} \tilde{x}_1 \left(\delta_1 - l_1\right) + \frac{1}{L_d^2} \tilde{x}_2 \left(\delta_2 - l_2\right) \\
&= \begin{bmatrix} \tilde{x}_1 & \tilde{x}_2 \end{bmatrix} \begin{bmatrix} -\frac{R_s}{L_d L_q^2} & \frac{\omega_e}{L_d L_q} \\ -\frac{\omega_e}{L_q L_d} & -\frac{R_s}{L_q L_d^2} \end{bmatrix} \begin{bmatrix} \tilde{x}_1 \\ \tilde{x}_2 \end{bmatrix} \\
&+ \frac{1}{L_q^2} \tilde{x}_1 \left(\delta_1 - l_1\right) + \frac{1}{L_d^2} \tilde{x}_2 \left(\delta_2 - l_2\right) \\
&= -\frac{\tilde{x}_1^2 R_s}{L_d L_q^2} - \frac{\tilde{x}_2^2 R_s}{L_q L_d^2} + \frac{1}{L_q^2} \tilde{x}_1 \left(\delta_1 - l_1\right) + \frac{1}{L_d^2} \tilde{x}_2 \left(\delta_2 - l_2\right)
\end{aligned}
\tag{6.18}
$$

Equation 6.14 defines $l_1 = k_1 \mathrm{sgn}\left(\tilde{x}_1\right)$ and $l_2 = k_2 \mathrm{sgn}\left(\tilde{x}_2\right)$. By the selection of the gains $k_1 = l_{11} + k_{12}$ and $k_2 = k_{21} + k_{22}$ with $k_{11} > \delta_1$, $k_{21} > \delta_2$, and $k_1, k_2, k_{11}, k_{12}, k_{21}, k_{22} > 0$ the derivative of the Lyapunov function becomes:

$$\begin{aligned}\dot{V} &= -\frac{\tilde{x}_1^2 R_s}{L_d L_q^2} - \frac{\tilde{x}_2^2 R_s}{L_q L_d^2} - \frac{1}{L_q^2}\left(k_1 \left|\tilde{x}_1\right| - \delta_1 \tilde{x}_1\right) - \frac{1}{L_d^2}\left(k_2 \left|\tilde{x}_2\right| - \delta_2 \tilde{x}_2\right) \\ &\leq -\frac{\tilde{x}_1^2 R_s}{L_d L_q^2} - \frac{\tilde{x}_2^2 R_s}{L_q L_d^2} - \frac{k_{12}\left|\tilde{x}_1\right|}{L_q^2} - \frac{k_{22}\left|\tilde{x}_2\right|}{L_d^2}\end{aligned} \tag{6.19}$$

This derivative function becomes negative definite proving the stability of the observer. This condition ensures that the observer will converge to the sliding surface in finite time. The low frequency component associated to the high gain observer compensates for the disturbance. In order to obtain the information of the disturbance it is necessary to filter the signal from the high gain observer. From (6.16) it is clear that when $\tilde{x}^T = 0$ then $\delta(x) = LPF(L(\tilde{x}))$. That is:

$$\begin{aligned} LPF\left(k_1 \mathrm{sgn}(\tilde{x}_1)\right) &= \frac{v_{ds-h}^r}{L_d} \\ LPF\left(k_2 \mathrm{sgn}(\tilde{x}_2)\right) &= \frac{v_{qs-h}^r}{L_q} \end{aligned} \tag{6.20}$$

where a LPF's is used to remove the undesired components of $L(\tilde{x})$ produced by the *sgn* function, these frequency components are located at frequencies higher than the switching frequency. These low pass filters have a bandwith significantly wider than the SRFF's, because their purpose is to remove the frequency components located at least one order of magnitude further than the injected high frequency signals. Using this observer, the power frequency can be removed entirely from the high frequency signal, moreover no assumptions are needed with respect to the stator resistance. The rotor position estimation can be done by a similar approach as described in the subsection 6.2.1. The disturbance can be written as:

$$\begin{aligned}\delta(x) &= \begin{bmatrix} \delta^r_{dsh} \\ \delta^r_{qsh} \end{bmatrix} \\ &= \begin{bmatrix} \frac{1}{L_d} & 0 \\ 0 & \frac{1}{L_q} \end{bmatrix} \begin{bmatrix} v^r_{dsh} \\ v^r_{qsh} \end{bmatrix}\end{aligned} \tag{6.21}$$

For injected voltage in the estimated rotor frame of reference, it is possible to get an equivalent expression for the rotor position error.

$$\begin{aligned}\begin{bmatrix} v^{\hat{r}}_{dsh} \\ v^{\hat{r}}_{qsh} \end{bmatrix} &= R^{-1}\left(\tilde{\theta}_e\right) \begin{bmatrix} L_{dh} & 0 \\ 0 & L_{qh} \end{bmatrix} R\left(\tilde{\theta}_e\right) \begin{bmatrix} \delta^r_{dsh} \\ \delta^r_{qsh} \end{bmatrix} \\ &= \begin{bmatrix} \bar{L} + L_\Delta \cos(2\theta_e) & L_\Delta \sin(2\theta_e) \\ L_\Delta \sin(2\theta_e) & \bar{L} - L_\Delta \cos(2\theta_e) \end{bmatrix} \begin{bmatrix} \delta^r_{dsh} \\ \delta^r_{qsh} \end{bmatrix}\end{aligned} \tag{6.22}$$

where

$$\bar{L} = \frac{L_{dh} + L_{qh}}{2}, \quad L_\Delta = \frac{L_{dh} - L_{qh}}{2} \tag{6.23}$$

For direct axis voltage injection of equation(6.7) and by substituting equation (6.21) in equation (6.22), the quadrature axis disturbance can be written as:

$$LPF\left(L_2\left(\tilde{x}_2\right)\right) = \delta^r_{qsh} = -\frac{V_h L_\Delta \cos\left(\omega_h t\right)}{L_d L_q} \sin(2\tilde{\theta}_e) \tag{6.24}$$

The high frequency quadrature axis disturbance is demodulated to get the rotor position information as shown in Figure 6.4. A PI regulator and an integrator are used to minimize the error function $f\left(\tilde{\theta}_e\right)$ as shown in equation (6.25). The minimization of $f\left(\tilde{\theta}_e\right)$ leads to the minimization of the error in the rotor position.

$$f\left(\tilde{\theta}_e\right) = \frac{V_h L_\Delta}{2\omega_h L_d L_q} \sin(2\tilde{\theta}_e) \approx K_{err}\tilde{\theta}_e \tag{6.25}$$

The overall system is shown in Figure 6.5.

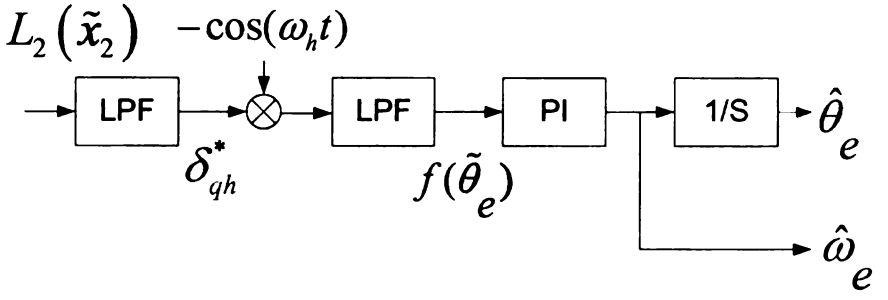

Figure 6.4: Block diagram of rotor position estimation by the use of a high current observer

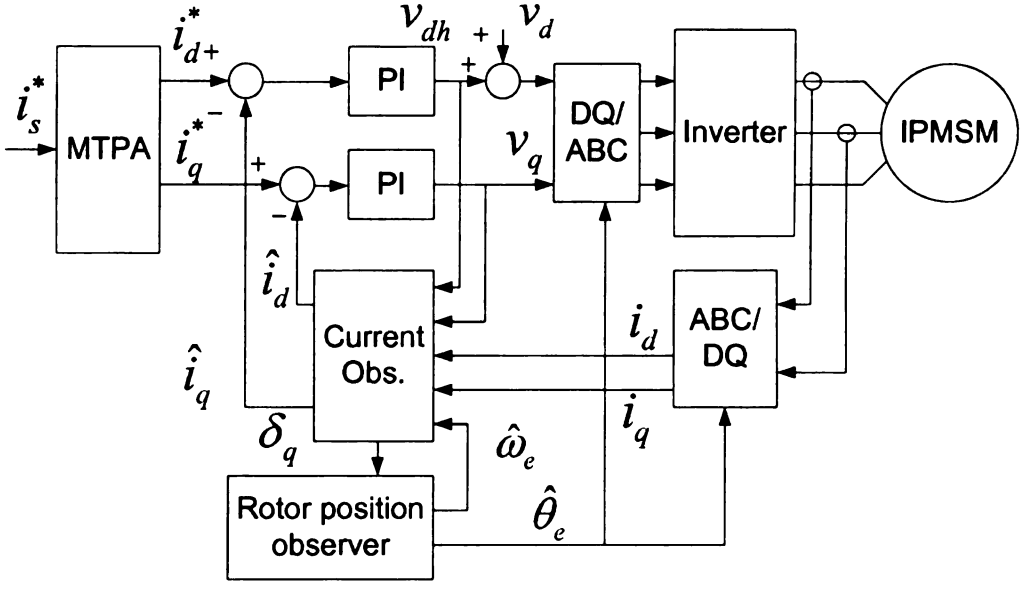

Figure 6.5: Proposed rotor position estimation block diagram

6.3 Experimental Results

The proposed rotor position estimator was validated experimentally and compared with the filtered controller. The experimental setup is shown and described in

Apendix A, for reference, the schematic of the experimental setup is shown in Figure 6.6. The dynamometer is set to operate in constant speed $\omega_m = 100\ r/min.$ and the PMAC is operated in current/torque control. The motor and the injection parameters are listed on Table 6.1. To operate the machine under the same conditions, the input high frequency voltage component should be the same for both topologies. As listed above for the proposed controller, the commanded high frequency voltage differs from the input high frequency voltage component. For a fixed input high frequency voltage component $v_d = 20\ V$, equation (6.10) is used to calculate v_{dh}, the required commanded voltage v_{dh} is equal to 27 V.

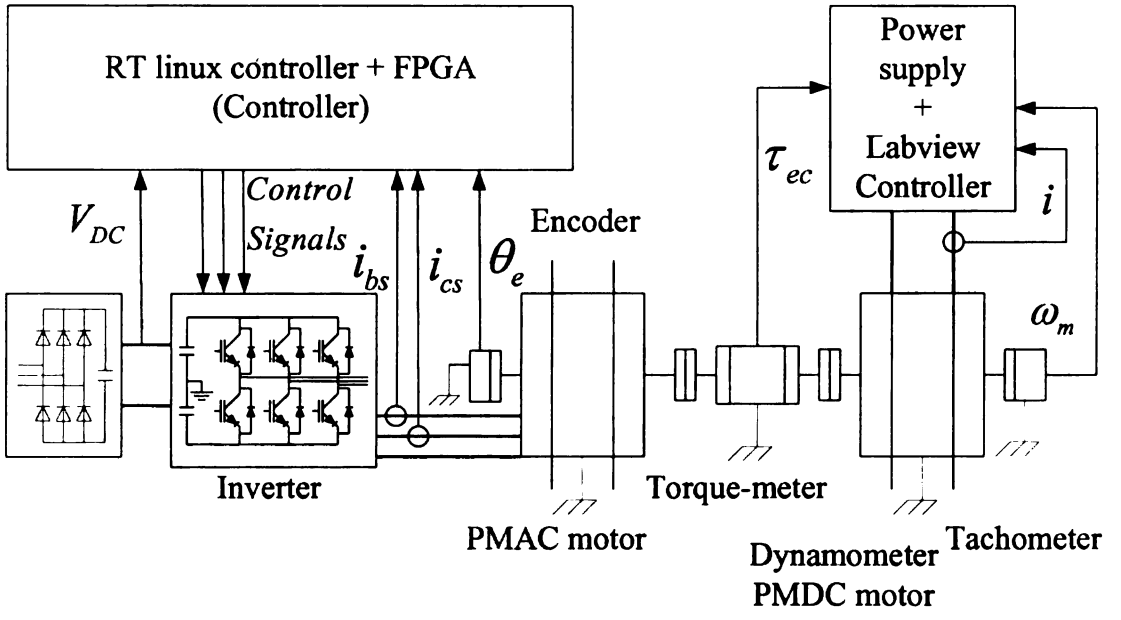

Figure 6.6: Experimental Setup

The proposed methodology subsection 6.2.2 was compared with the one of subsection 6.2.1 for two operating conditions: steady state and for a current ramp with rise time of $t_{rise} = 0.1\ s$. Filter parameters were kept constant. Tables 6.2 and 6.3 summarize the comparison of the two methodologies, for steady state error and transient respectively. The current commands are applied either in the quadrature axis, $I_S = I_q$, or in the current angle for maximum torque per ampere, $I_S = I_O$, and

Table 6.1: Experiment setup parameters

Parameter	Value	Units
Number of pole pairs	2	
Stator resistance	0.4	Ω
Rotor flux linkages	0.4652	Wb
Direct axis inductance L_d	0.01462	H
Quadrature axis inductance L_q	0.04810	H
Rated peak voltage per phase	120	V
Rated peak current	20	A
Injected frequency ω_h	250	Hz
Mechanical speed ω_m	100	r/min
Injected Voltage V_h	20	V
Proportional gain k_p	20	
Integral gain k_i	80	

with current increments every 25%.

Table 6.2: Steady state error in the rotor position estimation

Current	Error in the rotor position estimation in electrical degrees							
	Controller with filters				High performance controller			
(A)	Max	Min	P-P	Mean	Max	Min	P-P	Mean
$I_q = 0$	2.2	-3.1	5.3	0.0	2.5	-3.6	6.0	0.0
$I_q = 5$	1.0	-3.9	4.9	-1.6	0.6	-3.1	3.7	-1.4
$I_q = 10$	-3.6	-8.9	5.3	-6.5	-3.2	-7.9	4.7	-5.8
$I_q = 15$	-12.0	-17.7	5.7	-15.0	-11.2	-16.2	5.0	-13.9
$I_o = 0$	2.2	-3.1	5.3	0.0	2.5	-3.6	6.0	0.0
$I_o = 5$	1.4	-3.1	4.5	-1.0	2.4	-2.5	4.9	0.1
$I_o = 10$	1.5	-4.6	6.0	-1.9	1.4	-3.3	4.7	-0.9
$I_o = 15$	-2.1	-8.2	6.1	-4.5	-0.5	-5.2	4.7	-3.2

Practical implementation of the proposed observer requires that the voltage in the machine terminals and the commanded voltage to be equals. The observer proposed here uses the commanded voltage to extract injected signal from measured currents making important to match commanded and applied voltage. Dead time compensation were used to reduce the error difference between both voltages [64]. Several approaches have been proposed to compensate for dead time [13, 14, 15], where dead time, on-time off-time of the power devices and their associated drop-off voltage where

Table 6.3: Rotor position error for a current ramp

Current	Error in the rotor position estimation in electrical degrees					
	Controller with filters			High performance controller		
(A)	Min	Max	P-P	Min	Max	P-P
$I_q = 0$	-3.1	2.9	6.0	-3.6	2.5	6.0
$I_q = 5$	-6.2	6.7	12.9	-6.0	8.6	14.6
$I_q = 10$	-11.0	10.9	21.9	-12.9	8.7	21.6
$I_q = 15$	-25.8	13.6	39.4	-24.7	7.5	32.2
$I_o = 0$	-3.1	2.9	6.0	-3.6	2.5	6.0
$I_o = 5$	-4.2	6.6	10.8	-5.6	6.2	11.8
$I_o = 10$	-11.8	13.6	25.4	-10.6	13.8	24.4
$I_o = 15$	-18.1	17.1	35.2	-15.2	17.5	32.7

included to corrected to for this effect. A simple approach is used to correct for dead time, where the drop of voltage in the power electronics devices where neglected. The commanded voltages were corrected as follows:

$$\begin{aligned} v_{a-INV} &= v_a^* + \frac{T_d}{T_{sw}} \frac{V_{DC}}{3} \left[2sign(i_a) - sign(i_b) - 2sign(i_c)\right] \\ v_{b-INV} &= v_b^* + \frac{T_d}{T_{sw}} \frac{V_{DC}}{3} \left[2sign(i_b) - sign(i_a) - 2sign(i_c)\right] \\ v_{c-INV} &= v_c^* + \frac{T_d}{T_{sw}} \frac{V_{DC}}{3} \left[2sign(i_c) - sign(i_a) - 2sign(i_b)\right] \end{aligned} \tag{6.26}$$

where v_{a-INV}, v_{b-INV} and v_{b-INV} are the voltage used to calculate the switching times in the inverters, T_{sw} is the period associated to the switching frequency and T_d is the dead time. The methodology of subsection 6.2.1 was compared with the proposed estimator with and without dead time compensation for the following operating conditions: steady state and for a current ramp with rise time of $t_{rise} = 0.1$ s. Tables 6.4 and 6.5 summarize the comparison, for steady state and transient error respectively.

Figures 6.7, 6.8, 6.9 and 6.10 show the transient response of the rotor position estimation and speed estimation and Figures 6.11 and 6.12 show the reference and measured currents in the motor for a ramp in the current reference of 75%.

Table 6.4: Steady state error in the rotor position

Current (A)	Error in the rotor position estimation in electrical degrees					
	Controller with filters		Proposed observer		Proposed observer with T_d compensation	
	P-P	Mean	P-P	Mean	P-P	Mean
$I_o = 0$	5.30	0.00	6.00	0.00	4.81	-0.02
$I_o = 5$	4.50	-1.00	4.90	0.10	2.50	-1.03
$I_o = 10$	6.00	-1.90	4.70	-0.90	3.98	-1.74
$I_o = 15$	6.10	-4.50	4.70	-3.20	6.10	-3.16

Table 6.5: Rotor position error for a current ramp

Current (A)	Error in the rotor position estimation in electrical degrees								
	Controller with filters			Proposed observer			Proposed observer with T_d compensation		
	Min	Max	P-P	Min	Max	P-P	Min	Max	P-P
$I_o = 0$	-3.10	2.90	6.00	-3.60	2.50	6.00	-1.85	2.24	4.09
$I_o = 5$	-4.20	6.60	10.80	-5.60	6.20	11.80	-5.40	5.35	10.75
$I_o = 10$	-11.80	13.60	25.40	-10.60	13.80	24.40	-9.27	8.07	17.34
$I_o = 15$	-18.10	17.10	35.20	-15.20	17.50	32.70	-16.44	11.20	27.64

The performance of the two estimators were evaluated, by comparing the estimated torque during the transient specified above, as shown in Figure 6.13. The proposed rotor position estimator has a faster response Figure 6.13-a and comes to steady state faster than the one that used SRFF Figure 6.13-b.

The experimental results show uniform improvement in the steady state error and in the variation of the rotor position error. The proposed methodology works significantly better under high load conditions as shown in Tables 6.2 to 6.5. The cross saturation has significant effect in the rotor position estimation [65, 57], which is demonstrated by the experimental results, where the error in the rotor position is different for the same magnitude of the Current Space Vector (CSV) but for different values of δ. The cross saturation effect in the main torque has been described in [28]. Further analysis requires the inclusion of the cross saturation effect in the current observer or add techniques to correct the effect of cross saturation in the rotor position

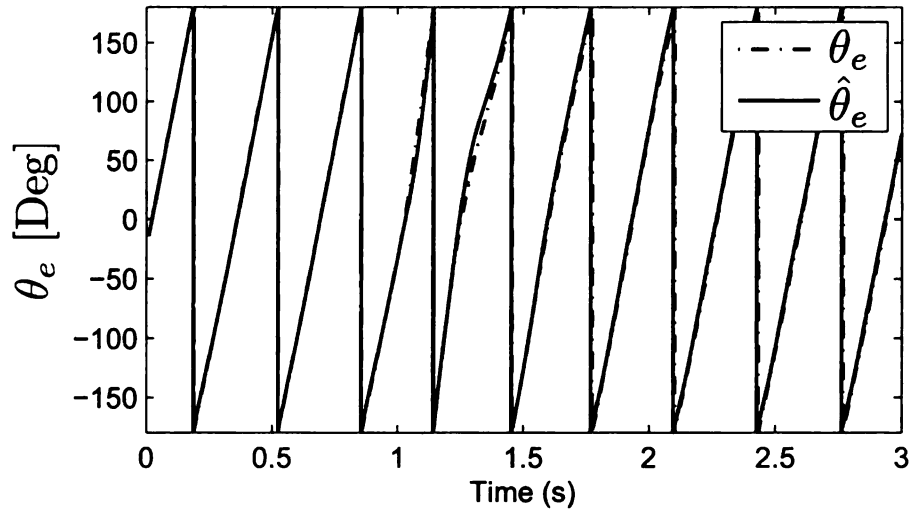

(a) Estimated rotor position

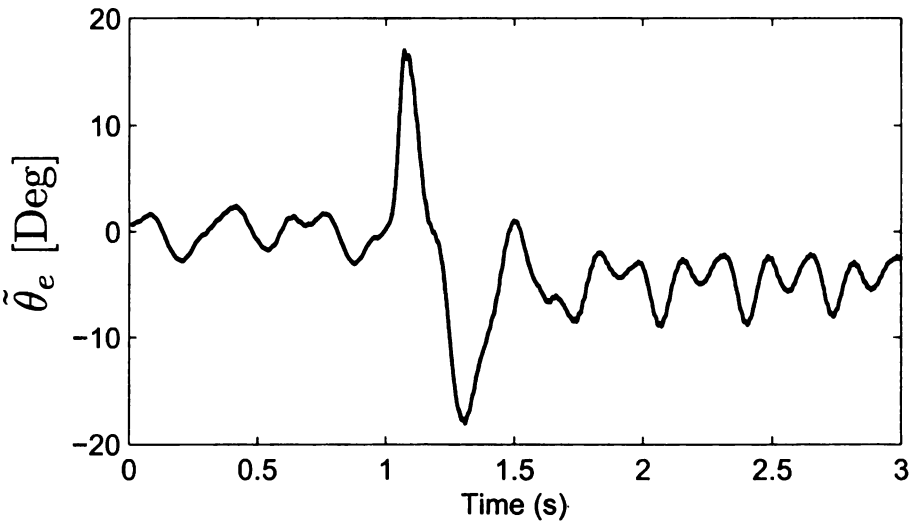

(b) Error in the rotor position estimation

Figure 6.7: Rotor position estimation for controller with filters

estimation [66]. Similarly the speed dependance of the controller-observer needs to be further explored. The main focus of the the work presented in this chapter was to present an alternative to the BSFs and the BPFs, and improving the dynamic performance of the controller, [66, 55] can be used to correct the rotor position error due cross-saturation and speed change.

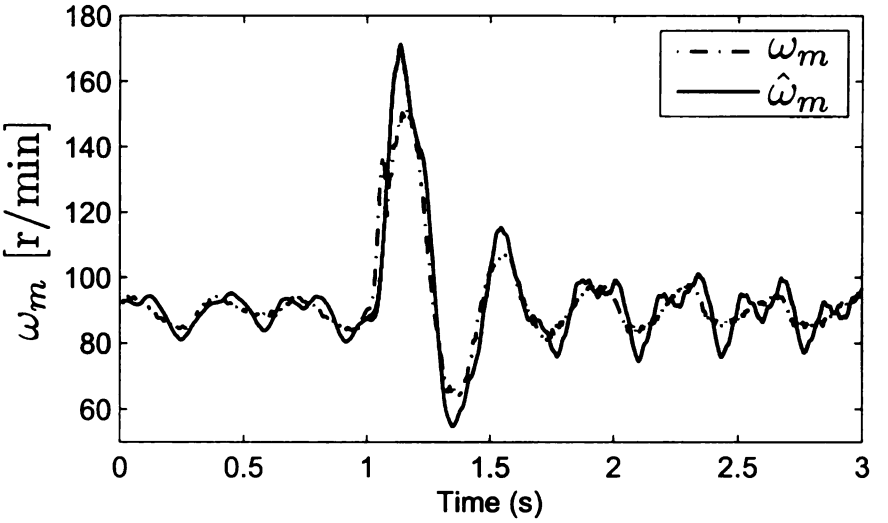

(a) Estimated speed

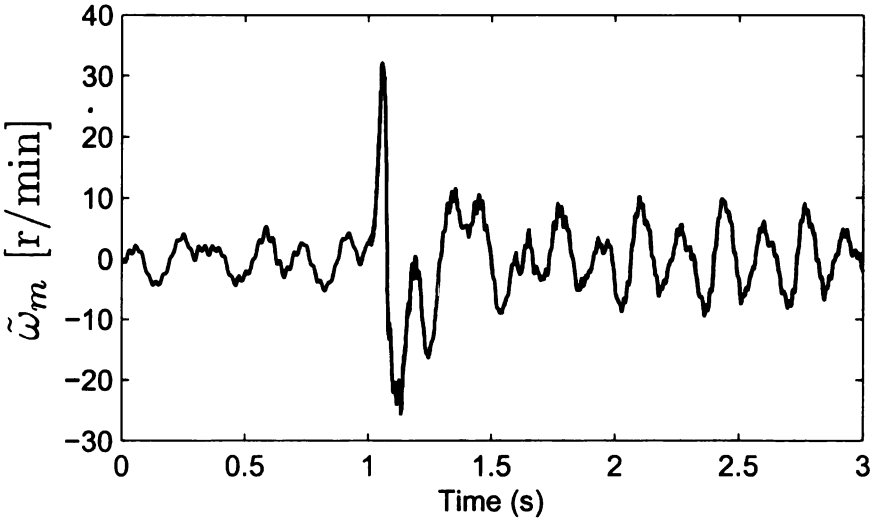

(b) Error in the speed estimation

Figure 6.8: Speed estimation for controller with filters

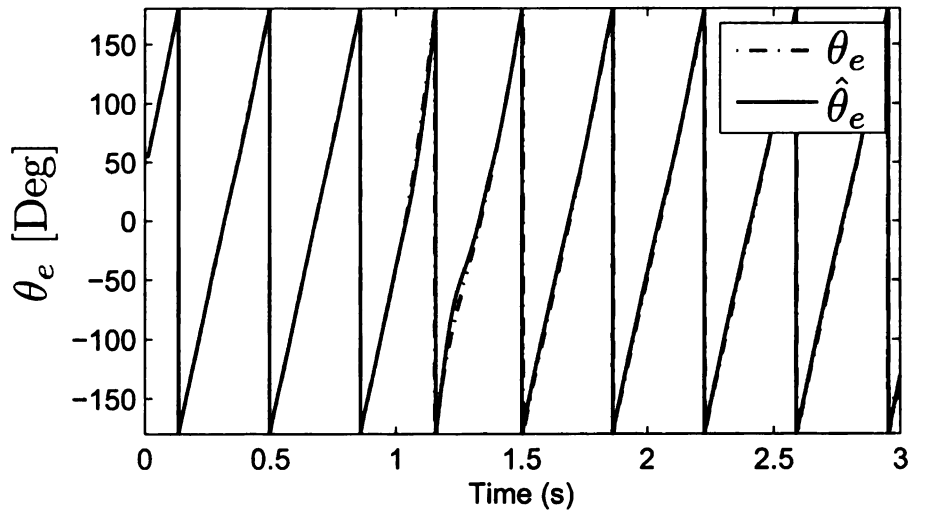

(a) Estimated rotor position

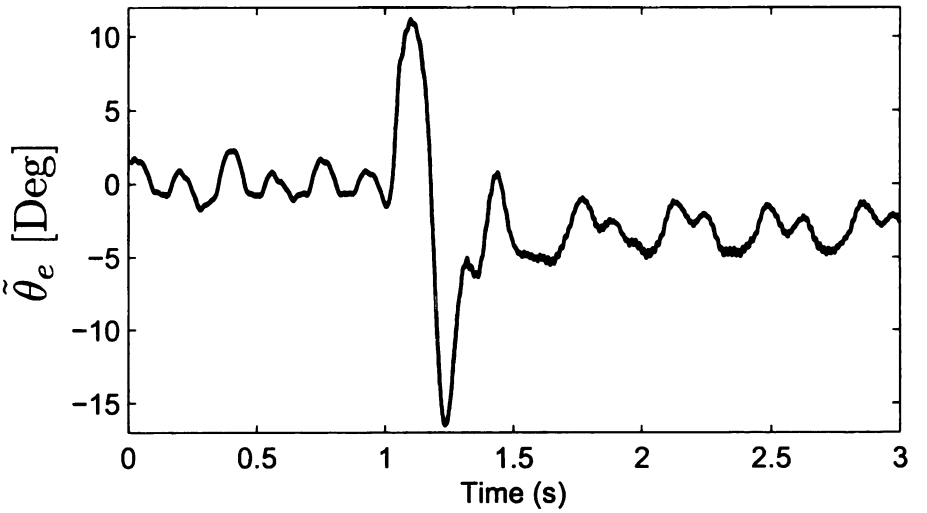

(b) Error in the rotor position estimation

Figure 6.9: Rotor position estimation for the high performance controller

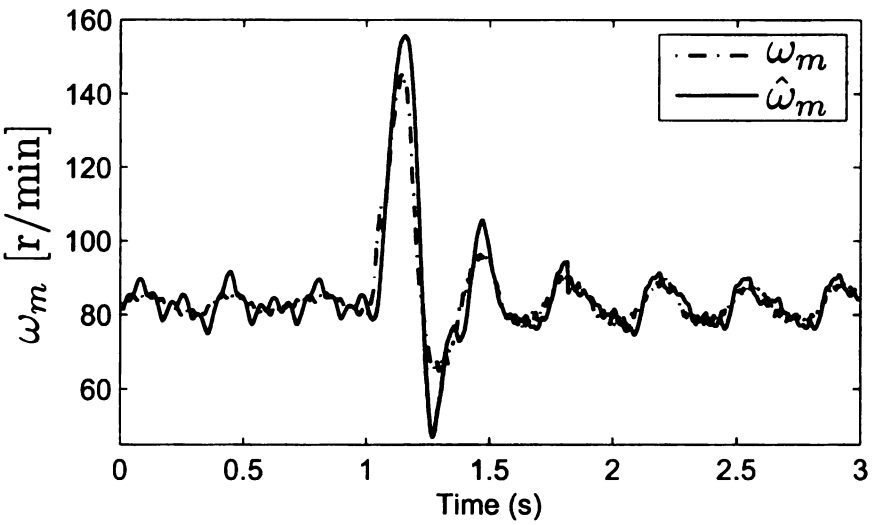

(a) Estimated speed

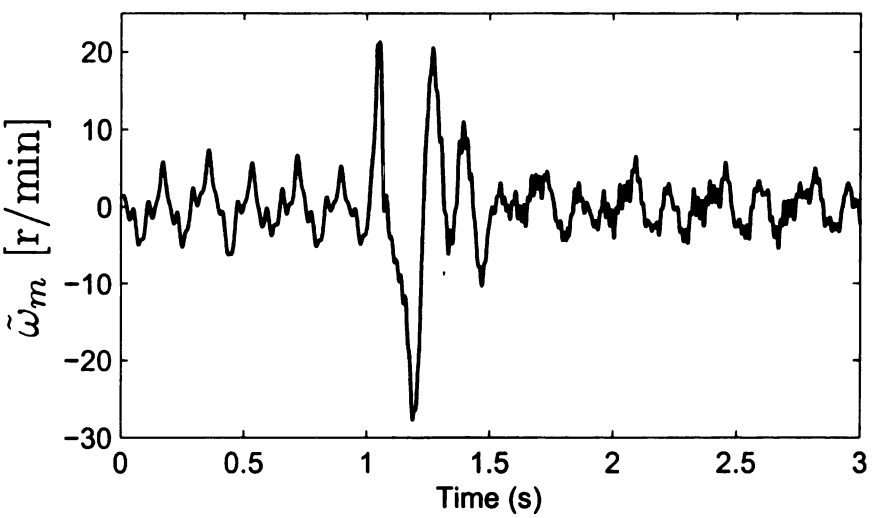

(b) Error in the speed estimation

Figure 6.10: Speed estimation for the high performance controller

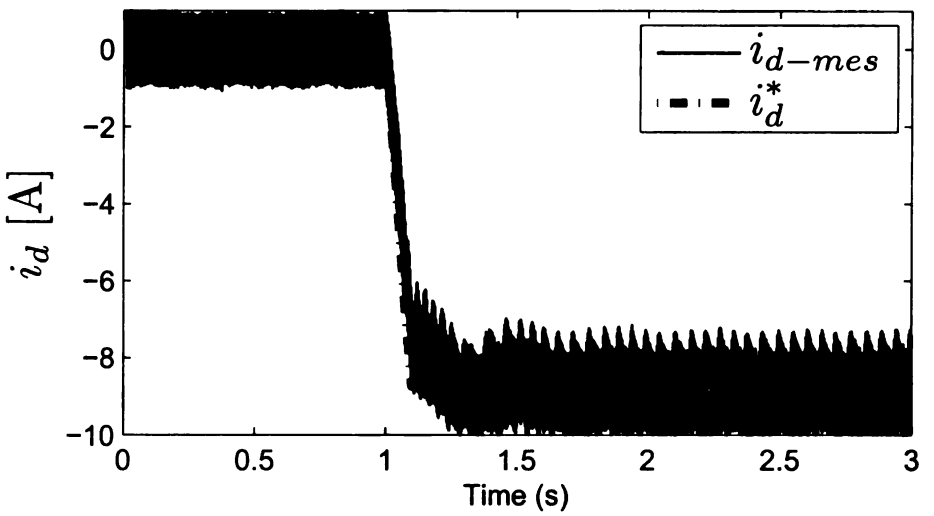

(a) i_d

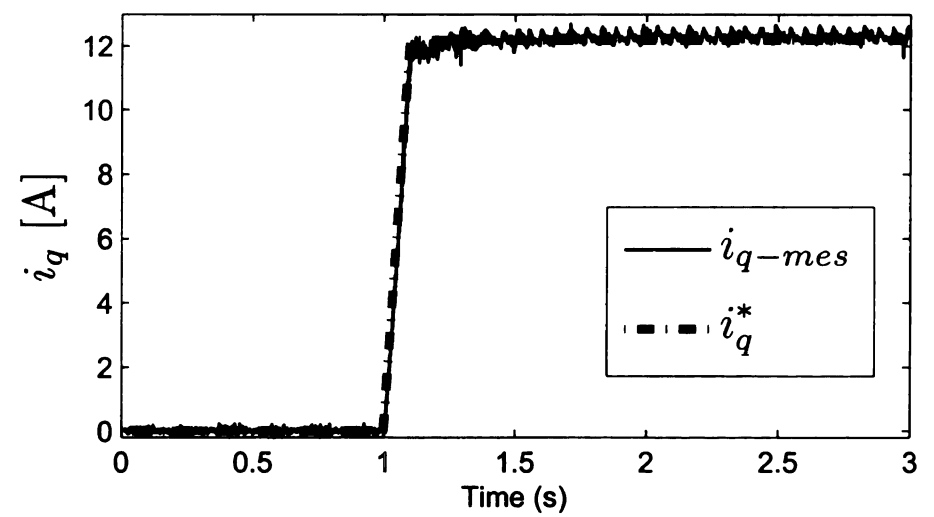

(b) i_q

Figure 6.11: Machine current for the controller with filters

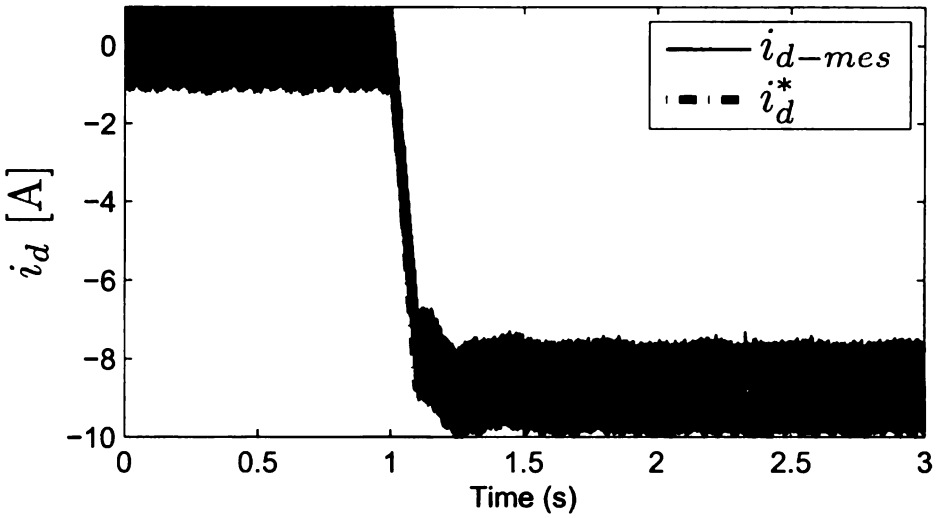

(a) i_d

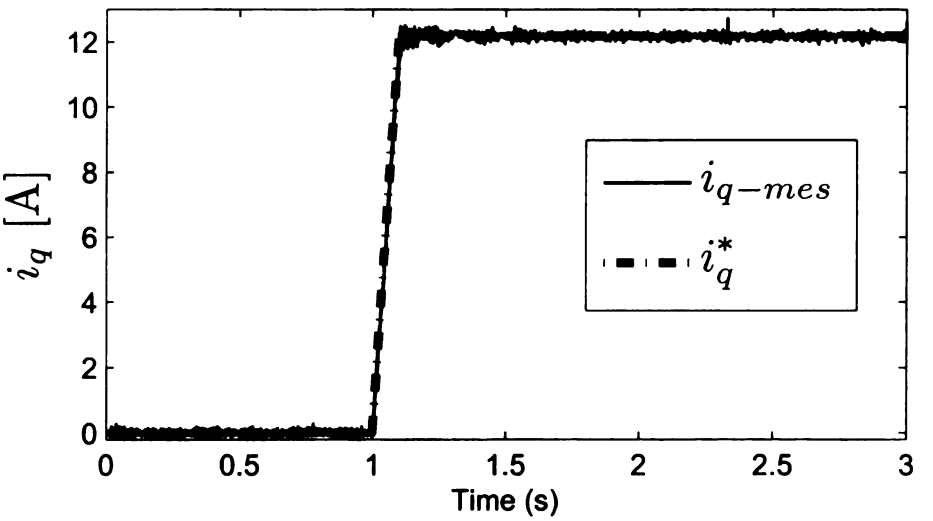

(b) i_q

Figure 6.12: Machine current for the high performance controller

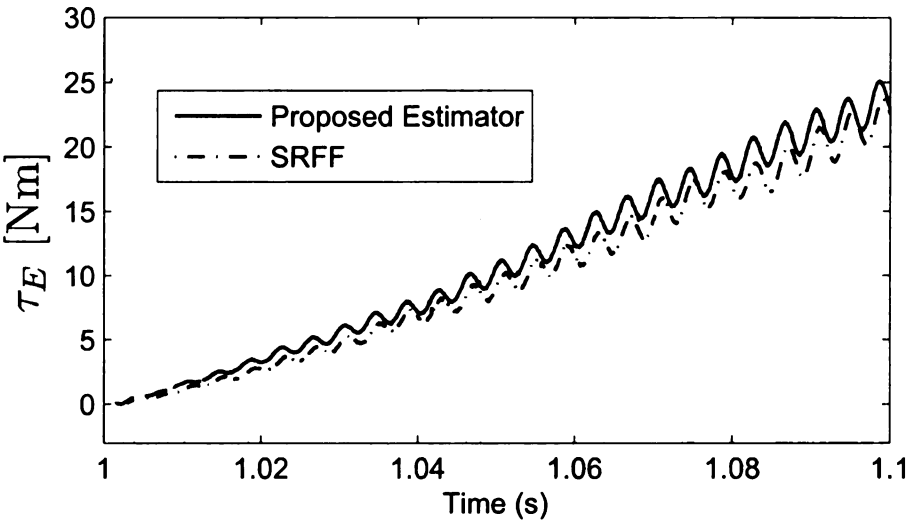

(a) τ_e

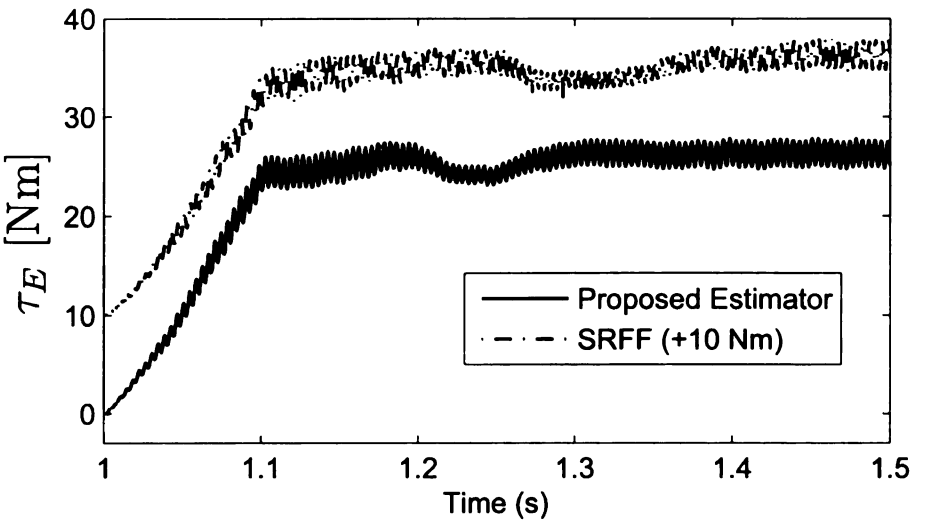

(b) τ_e

Figure 6.13: Dynamic performance comparison of the estimator

Chapter 7

Conclusions and Anticipated Future Work

This chapter presents the concluding remarks and future work as follows:

7.1 Cross Saturation Analysis

The cross magnetization was described, characterized and its effect in the torque was calculated. The cross magnetization was included in the machine model by two quasi-mutual inductances. Torque and voltage equations including mutual inductances were used to determine torque and speed profile. FEA simulations in four machines with different stator configuration and experimental results in a prototype motor were used to validate the proposed analysis.

7.2 Trajectory Optimization for the Operation of Traction Motors

A methodology for the optimal control of an interior permanent magnet motor for traction applications was presented. The methodology to calculate the optimal current command for a given torque and speed point considering cross saturation was described, and the optimal trajectory calculation was presented. The use of cross saturation and optimal trajectory calculation in the control algorithm leads to the operation of the motor with minimal energy losses. This work included the modification of the algorithm to calculate the optimal trajectory online. This approximation significatively reduces the computational time, however the solution was not optimal. The use of the approximated curves as an initial guest was also explored. It allows the reduction of the iteration number and achieves an optimal trajectory control. Simulated and experimental results validated the proposed methodology.

7.3 Trajectory Optimization for the Operation of Engine-generator Subsystem

A torque and speed optimization scheme of the engine-generator subsystem of a series hybrid electric vehicle was presented. The optimal methodology allows the calculation of the torque and speed references of the engine-generator subsystem that minimize the energy loss for a given target energy. An approximate optimal trajectory was proposed to implement this controller in real time. The developed algorithms were evaluated under different energy requirements and initial engine speeds through simulations. The simulation results demonstrated that the proposed optimal trajectory and its approximation improved the subsystem efficiency over conventional control techniques. Future work will consider the integration of the proposed optimization in

the overall optimization of the entire powertrain system.

7.4 Sensorless Control

Two methodologies for rotor position estimation based on voltage injection were presented. A high performance controller was described and a methodology for rotor position estimation was explained. A high gain current observer was described and its stability was proved. This observer was used to extract the high frequency components of the signals required for the rotor position estimation. The rotor position estimator with high gain current observer approach showed improvements over the classical estimator, where transient and steady state error in the rotor position estimation where analyzed. Further development would include the analysis of the cross saturation effect on the rotor position estimation.

APPENDICES

APPENDIX A

Experimental Setup

The experimental setup used to validate the proposed control techniques is described in this Appendix. Figures A.1 and A.2 shows the experimental setup and Figure A.3 shows the schematic.

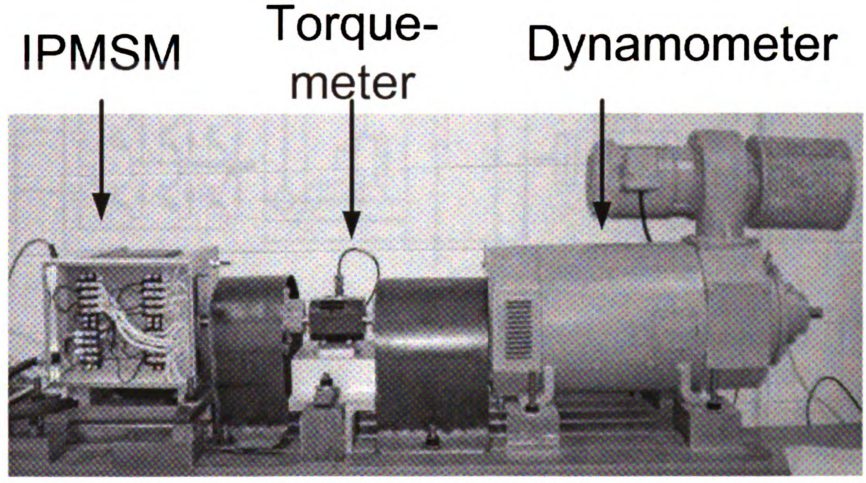

Figure A.1: Motor and dynamometer

The setup developed for this thesis is composed of the following devices:

- Real Time Controller: Rt-Linux and Field-Programmable Gate Array (FPGA).
- National Instrument based Data Acquisition System.
- Sensors: voltage, current, rotor position and torque.

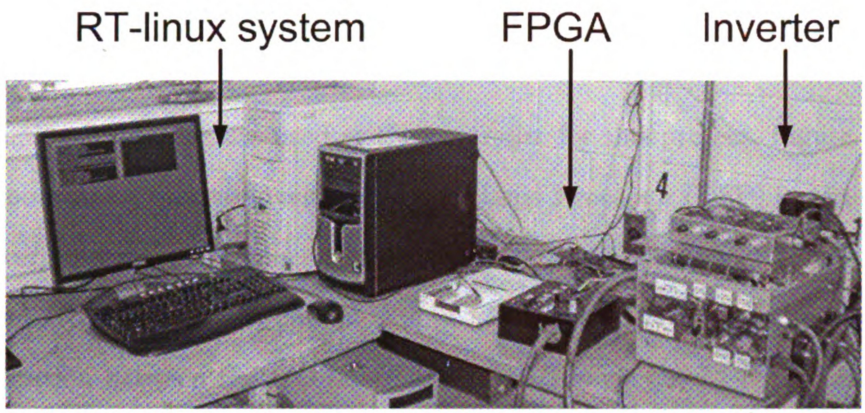

Figure A.2: Controller and inverter

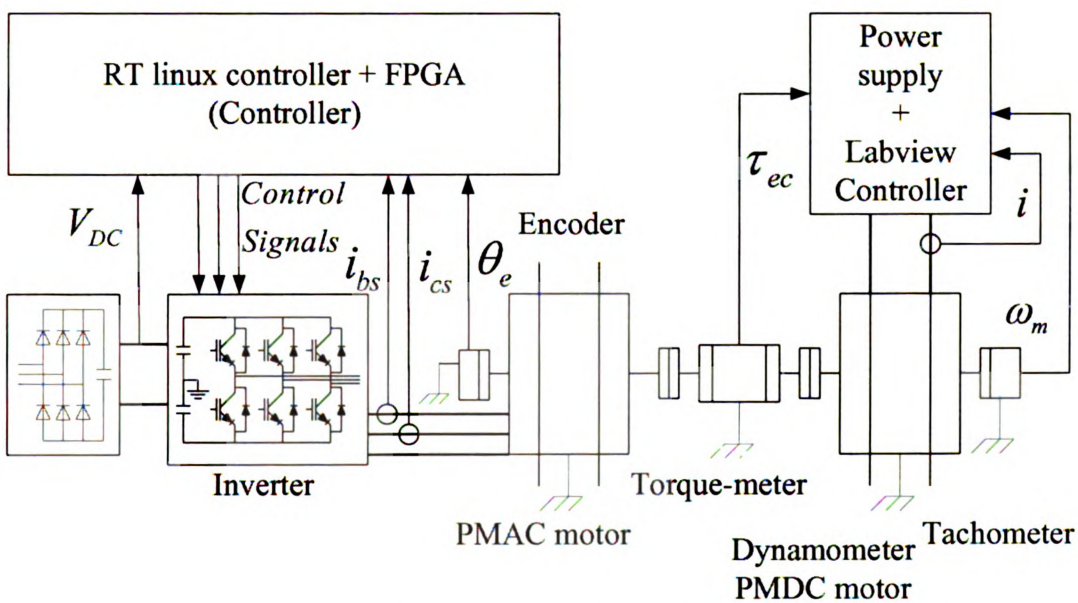

Figure A.3: Schematic of the experimental setup

- Interior Permanent Magnet Synchronous Motor.

- Inverter.

- Dynamometer.

A.1 Real Time Controller: Rt-Linux and FPGA

A PC running RT-Linux was used as the controller for this project, Figure A.4. The PC is a good choice compared with a Digital Signal Processor (DSP) in terms of cost, CPU power, and memory capacity. A fundamental limitation of the PC, however, is the limited I/O capability. A custom Xilinx FPGA based I/O board was developed. Communication between the I/O board and the PC is via the EPP parallel port.

The I/O-FPGA board has one encoder input, four D/A outputs, twelve PWM outputs and twelve A/D input channels. The encoder inputs accept dual quadrature channels and an index pulse in either differential or single-ended configurations. The board processes the encoder counts and stores absolute position in a twelve-bit counter. There are twelve digital outputs which can be configured for PWM (2500 counts at 20kHz), four D/A outputs (12-bit, +/-5V range) and twelve analog inputs (12-bit, +/-10V range). The list of the measured and output signals are presented below:

- Measure: DC-link voltage.
- Measure: two phase currents.
- Measure: one phase voltage.
- Measure: rotor position.
- Output: six PWM outputs.

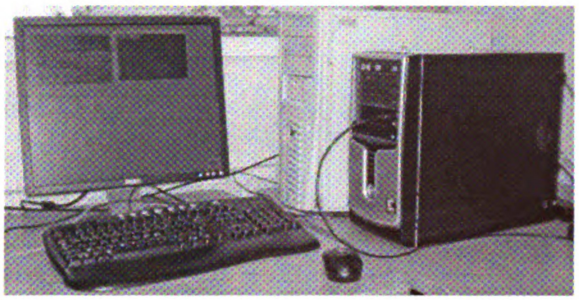

Figure A.4: RT-Linux

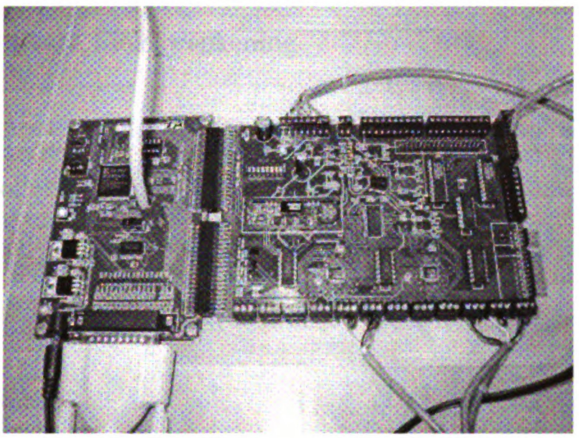

Figure A.5: FPGA and I/O

A.2 National Instrument Based Data Acquisition System

Two data acquisition boards were used with Labview. The first one (NI USB-6009) was used to develop a supervisory control for the dynamometer and the second one (NI USB-6259) was used to acquire and store voltage, current, torque and position.

In the supervisory control Labview were used to give the setpoints to de dynamometer an measure its signals. The analog to digital converters and the digital to analog converters have a resolution of 14-Bit, with a maximum sampling rate of 48 KiloSamples per second (kS/s). The measured and commanded signals are listed below:

- Measure: speed.
- Command: speed.
- Measure: armature current.
- Command: current.
- Command: torque or speed operation.
- Command: Activate Field weakening.

The second data acquisition card was used to collect data for analysis (not required for the online controller). Due to the sampling rate limitations two signals and the encoder were collected at the same time. The minimum sampling rate obtained was $5\mu s$ with a resolution of 16 bits. The measured signals are presented below:

- DC-link Voltage.
- DC-link Current.
- Phase Voltages.
- Torque.
- Rotor position.
- Speed.

A.3 Sensors: Voltage, Current, Rotor Position and Torque

A set of sensors were used to acquire signals for control and analysis. The following sensor were used:

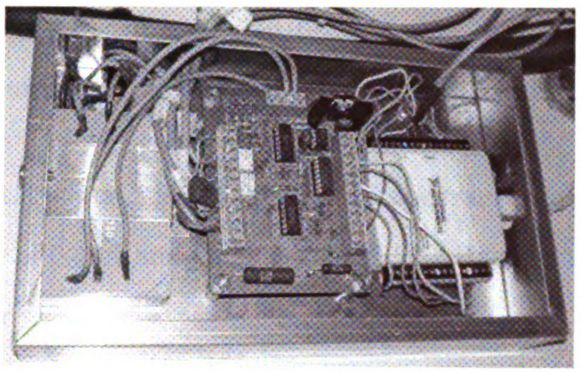

Figure A.6: NI USB-6009

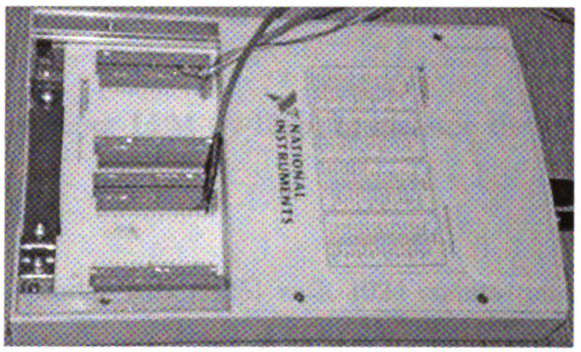

Figure A.7: NI USB-6259

Figure A.8: Labview with the virtual instrument

- Two phase currents were measured using current transducers LEM (la-100p) with rated accuracy of 0.45% and bandwidth of 0-200kHz.

- Two phase voltages were measured using voltage transducers LEM (lv-25p) with rated accuracy of 0.45% and bandwidth of 0-200kHz used to calibrate the rotor position sensor.

- A single current sensor LEM (la-100p) to measure the DC link current in the inverter.

- A single voltage sensor LEM (lv-100p) to measure the DC link voltage in the inverter.

- A quadrature encoder BEI (H25) with 1024 counts per revolution (4096 for quadrature) and an index pulse, this encoder was used to measure the rotor position.

- Torque sensor PCB (STS 5100) with a peak torque of 110 Nm with an amplifier PCB (SERIES 8159).

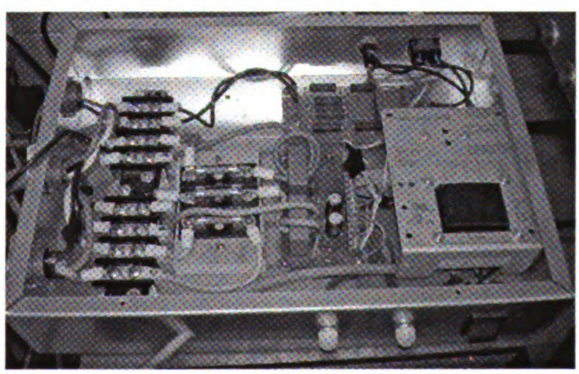

Figure A.9: Current and voltage sensors

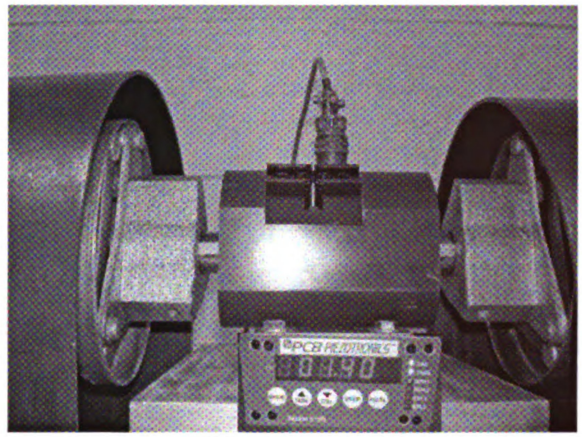

Figure A.10: Torque sensor

A.4 IPMSM

An IPMSM was designed and assembled to validate the proposed control. The machine has the following characteristics:

- Four poles.
- Two slots per pole per phase.
- Three phase.
- Winding pitch of 120^0.
- Double layer winding with 30 turns per coil and 60 turns per slot of copper conductor AWG 14.
- Neodymium iron boron magnets.

Figure A.11 shows the rotor, stator and windings configuration.

A.5 Inverter

An inverter was designed and assembled to operate the IPMSM. The Integrated Power Module (IPM) selected was a powerex (pm75cla120) with a rated voltage of 1200 V

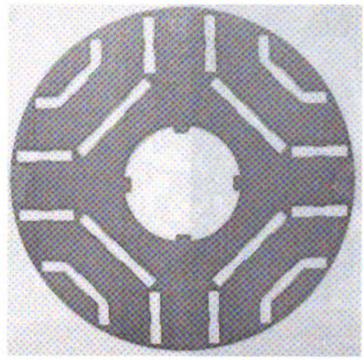

(a) Rotor

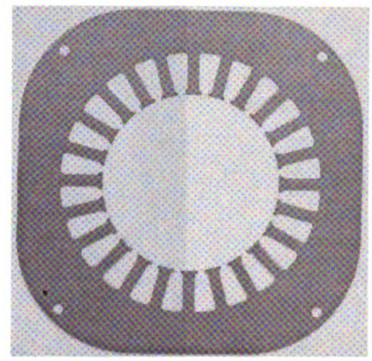

(b) Stator

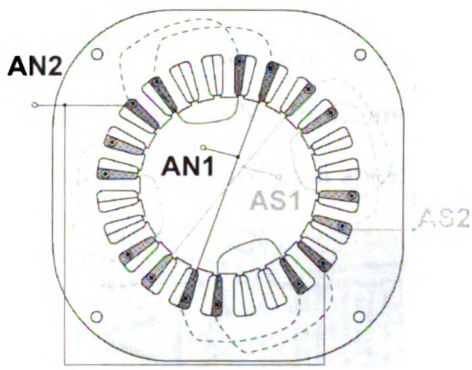

(c) Windings

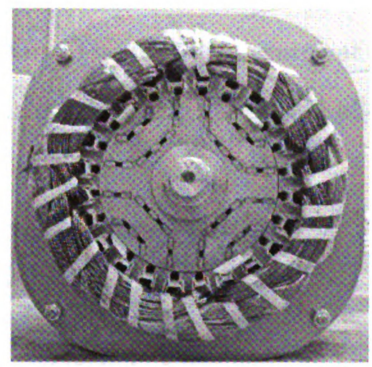

(d) Assembly

Figure A.11: IPMSM

DC and a rated current of 75 A. The gate drive used was a powerex BP7B. A bank of capacitor of $240\mu f$ was used for the DC-link. Figure A.12 shows the setup of the inverter used.

A.6 Dynamometer

A EMERSON dynamometer with a PMDC motor of $20HP$ was used in this work to control the speed (or torque) of the test machine. It is controlled by an analog command sent from the Labview. The analog signal can be configured to be proportional to either torque or speed. The motor has a maximum current of $60A$ DC, maximum

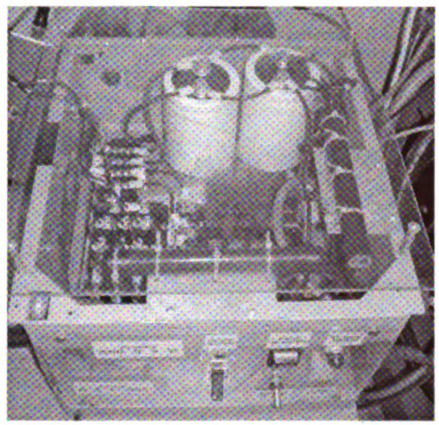

Figure A.12: Inverter

voltage of $220V$ DC and maximum torque of $80Nm$. The motor operates at a rated speed with full field of $1750r/min$, and optional field weakening command allows the motor to operate at a maximum speed od $2200r/min$.

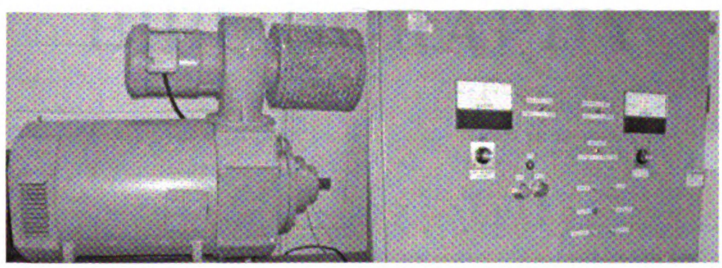

Figure A.13: Dynamometer

BIBLIOGRAPHY

BIBLIOGRAPHY

[1] J. Gieras, E. Santini, and M. Wing, "Calculation of synchronous reactances of small permanent-magnet alternating-current motors: comparison of analytical approach and finite element method with measurements," *IEEE Transactions on Magnetics*, vol. 34, no. 5, pp. 3712–3720, Sep. 1998.

[2] G.-H. Kang, J.-P. Hong, G.-T. Kim, and J.-W. Park, "Improved parameter modeling of interior permanent magnet synchronous motor based on finite element analysis," *IEEE Transactions on Magnetics*, vol. 36, no. 4, pp. 1867–1870, Jul. 2000.

[3] Z. Zhu, Z. Xia, Y. Shi, D. Howe, A. Pride, and X. Chen, "Performance of halbach magnetized brushless ac motors," *IEEE Transactions on Magnetics*, vol. 39, no. 5, pp. 2992–2994, Sep. 2003.

[4] Y. Yan, J. Zhu, H. Lu, Y. Guo, and S. Wang, "A pmsm model incorporating structural and saturation saliencies," *Proceedings of the Eighth International Conference on Electrical Machines and Systems, 2005. ICEMS 2005*, vol. 1, pp. 194–199 Vol. 1, Sep. 2005.

[5] E. Lovelace, T. Jahns, and J. Lang, "A saturating lumped-parameter model for an interior pm synchronous machine," *IEEE Transactions on Industry Applications*, vol. 38, no. 3, pp. 645–650, May.-Jun. 2002.

[6] S.-Y. Kwak, J.-K. Kim, and H.-K. Jung, "Characteristic analysis of multilayer-buried magnet synchronous motor using fixed permeability method," *IEEE Transaction on Energy Conversion*, vol. 20, no. 3, pp. 549–555, Sep. 2005.

[7] Y. Li, Z. Zhu, D. Howe, and C. Bingham, "Modeling of cross-coupling magnetic saturation in signal-injection-based sensorless control of permanent-magnet brushless ac motors," *IEEE Transactions on Magnetics*, vol. 43, no. 6, pp. 2552–2554, Jun. 2007.

[8] N. Bianchi and S. Bolognani, "Influence of rotor geometry of an ipm motor on sensorless control feasibility," *IEEE Transactions on Industry Applications*, vol. 43, no. 1, pp. 87–96, Jan.-Feb. 2007.

[9] I. Boldea and S. Nasar, "A general equivalent circuit (gec) of electric machines including cross-coupling saturation and frequency effects," *IEEE Transaction on Energy Conversion*, vol. 3, no. 3, pp. 689–695, Sep. 1988.

[10] A. Takahashi, S. Kikuchi, S. Wakui, H. Mikami, K. Ide, and K. Shima, "Evaluation of torque characteristics in saturated magnetic field for permanent-magnet synchronous motors," *IEEE Power Engineering Society General Meeting, 2007*, pp. 1–7, Jun. 2007.

[11] B. Stumberger, G. Stumberger, D. Dolinar, A. Hamler, and M. Trlep, "Evaluation of saturation and cross-magnetization effects in interior permanent-magnet synchronous motor," *IEEE Transactions on Industry Applications*, vol. 39, no. 5, pp. 1264–1271, Sep.-Oct. 2003.

[12] K. Rahman and S. Hiti, "Identification of machine parameters of a synchronous motor," *Conference Record of the Industry Applications Conference, 2003. 38th IAS Annual Meeting.*, vol. 1, pp. 409–415 vol.1, Oct. 2003.

[13] N. Urasaki, T. Senjyu, K. Uezato, and T. Funabashi, "Adaptive dead-time compensation strategy for permanent magnet synchronous motor drive," *IEEE Transactions on Energy Conversion*, vol. 22, no. 2, pp. 271 –280, Jun. 2007.

[14] H. Seon-Hwan and K. Jang-Mok, "Dead time compensation method for voltage-fed pwm inverter," *IEEE Transactions on Energy Conversion*, vol. 25, no. 1, pp. 1 –10, Mar. 2010.

[15] V. Blasko, "A novel method for selective harmonic elimination in power electronic equipment," *IEEE Transactions on Power Electronics,*, vol. 22, no. 1, pp. 223 –228, Jan. 2007.

[16] T. Senjyu, N. Urasaki, and K. Uezato, "Influence of stator iron loss in flux weakening region for interior PMSM," in *Proceedings of International Conference on Power Electronic Drives and Energy Systems for Industrial Growth*, vol. 1, Dec. 1998, pp. 20–25.

[17] R. Morales-Caporal and M. Pacas, "A predictive torque control for the synchronous reluctance machine taking into account the magnetic cross saturation," *IEEE Transactions on Industrial Electronics*, vol. 54, no. 2, pp. 1161–1167, Apr. 2007.

[18] Y. Jeong, S. Sul, S. Hiti, and K. Rahman, "Online minimum-copper-loss control of an interior permanent-magnet synchronous machine for automotive applications," *IEEE Transactions on Industry Applications*, vol. 42, no. 5, pp. 1222–1229, Sep.-Oct. 2006.

[19] S.-M. Sue and C.-T. Pan, "Voltage-constraint-tracking-based field-weakening control of IPM synchronous motor drives," *IEEE Transactions on Industrial Electronics*, vol. 55, no. 1, pp. 340–347, Jan. 2008.

[20] C. Jo, J.-Y. Seol, and I.-J. Ha, "Flux-weakening control of IPM motors with significant effect of magnetic saturation and stator resistance," *IEEE Transactions on Industrial Electronics*, vol. 55, no. 3, pp. 1330–1340, Mar. 2008.

[21] R. Monajemy and R. Krishnan, "Control and dynamics of constant-power-loss-based operation of permanent-magnet synchronous motor drive system," *IEEE Transactions on Industrial Electronics*, vol. 48, no. 4, pp. 839–844, Aug. 2001.

[22] R. Molavi and D. Khaburi, "Optimal control strategies for speed control of permanent-magnet synchronous motor drives," in *Proceedings of World Academy of Science, Engineering and Technology*, vol. 34, Oct. 2008, pp. 428–423.

[23] C. Mademlis and N. Margaris, "Loss minimization in vector-controlled interior permanent-magnet synchronous motor drives," *IEEE Transactions on Industrial Electronics*, vol. 49, no. 6, pp. 1344–1347, Dec. 2002.

[24] C. Cavallaro, A. DiTommaso, R. Miceli, A. Raciti, G. Galluzzo, and M. Trapanese, "Efficiency enhancement of permanent-magnet synchronous motor drives by online loss minimization approaches," *IEEE Transactions on Industrial Electronics*, vol. 52, no. 4, pp. 1153–1160, Aug. 2005.

[25] I. Panahi and H. Toliyat, "An efficient processor-based online generation of time-optimal trajectories," *IEEE Transactions on Control Systems Technology*, vol. 14, no. 5, pp. 966–973, Sep. 2006.

[26] M. Schlemmer and S. Agrawal, "A computational approach for time-optimal planning of high-rise elevators," *IEEE Transactions on Control Systems Technology*, vol. 10, no. 1, pp. 105–111, Jan. 2002.

[27] J. Choi and B. Kim, "Near-time-optimal trajectory planning for wheeled mobile robots with translational and rotational sections," *IEEE Transactions on Robotics and Automation*, vol. 17, no. 1, pp. 85–90, Feb. 2001.

[28] C. Nino, A. Tariq, S. Jurkovic, and E. Strangas, "Optimal speed control of an interior permanent magnet synchronous motor including cross saturation," in *IEEE International Electric Machines and Drives Conference*, May. 2009, pp. 292–298.

[29] D. E. Kirk, *Optimal Control Theory: An Introduction*, 1st ed. Prentice-Hall, 1970, pp. 329–337.

[30] M. Athans and G. Falb, *Optimal Control*, 1st ed. HMcGrawHill, 1966, pp. 284–351.

[31] M. Ducusin, S. Gargies, and C. Mi, "Modeling of a series hybrid electric high-mobility multipurpose wheeled vehicle," *IEEE Transactions on Vehicular Technology*, vol. 56, no. 2, pp. 557 –565, Mar. 2007.

[32] C. Chan, A. Bouscayrol, and K. Chen, "Electric, hybrid, and fuel-cell vehicles: Architectures and modeling," *IEEE Transactions on Vehicular Technology*, vol. 59, no. 2, pp. 589 –598, Feb. 2010.

[33] F. Salmasi, "Control strategies for hybrid electric vehicles: Evolution, classification, comparison, and future trends," *IEEE Transactions on Vehicular Technology*, vol. 56, no. 5, pp. 2393 –2404, Sep. 2007.

[34] A. Sciarretta and L. Guzzella, "Control of hybrid electric vehicles," *IEEE Control Systems Magazine*, vol. 27, no. 2, pp. 60 –70, Apr. 2007.

[35] S. Barsali, M. Ceraolo, and A. Possenti, "Techniques to control the electricity generation in a series hybrid electrical vehicle," *IEEE Transactions on Energy Conversion*, vol. 17, no. 2, pp. 260 –266, Jun. 2002.

[36] T. Katrasnik, F. Trenc, and S. Opresnik, "Analysis of energy conversion efficiency in parallel and series hybrid powertrains," *IEEE Transactions on Vehicular Technology*, vol. 56, no. 6, pp. 3649 –3659, Nov. 2007.

[37] J. Gao, G. G. Zhu, E. G. Strangas, and F. Sun, "Equivalent fuel consumption optimal control of a series hybrid electric vehicle," *Proc. IMechE, Part D: J. Automobile Engineering*, vol. 223, no. 8, pp. 1003–1018, 2009.

[38] F. Salmasi, "Control strategies for hybrid electric vehicles: Evolution, classification, comparison, and future trends," *IEEE Transactions on Vehicular Technology*, vol. 56, no. 5, pp. 2393 –2404, sept. 2007.

[39] L. V. Perez, G. R. Bossio, D. Moitre, and G. O. Garcia, "Optimization of power management in an hybrid electric vehicle using dynamic programming," *Mathematics and Computers in Simulation*, vol. 73, no. 1-4, pp. 244 – 254, Jun. 2006.

[40] M. Ceraolo, A. di Donato, and G. Franceschi, "A general approach to energy optimization of hybrid electric vehicles," *IEEE Transactions on Vehicular Technology*, vol. 57, no. 3, pp. 1433 –1441, May. 2008.

[41] S. Barsali, C. Miulli, and A. Possenti, "A control strategy to minimize fuel consumption of series hybrid electric vehicles," *IEEE Transactions on Energy Conversion*, vol. 19, no. 1, pp. 187 – 195, Mar. 2004.

[42] Z. Chen, M. Tomita, S. Doki, and S. Okuma, "An extended electromotive force model for sensorless control of interior permanent-magnet synchronous motors," *IEEE Transactions on Industrial Electronics*, vol. 50, no. 2, pp. 288–295, Apr. 2003.

[43] O. Wallmark and L. Harnefors, "Sensorless control of salient pmsm drives in the transition region," *IEEE Transactions on Industrial Electronics*, vol. 53, no. 4, pp. 1179–1187, Jun. 2006.

[44] B.-H. Bae, S.-K. Sul, J.-H. K. won, and J.-S. Byeon, "Implementation of sensorless vector control for super-high-speed pmsm of turbo-compressor," *IEEE Transactions on Industry Applications*, vol. 39, no. 3, pp. 811 – 818, May.-Jun. 2003.

[45] J. Holtz and J. Juliet, "Sensorless acquisition of the rotor position angle of induction motors with arbitrary stator windings," *IEEE Transactions on Industry Applications*, vol. 41, no. 6, pp. 1675–1682, Nov.-Dec. 2005.

[46] S. Ji-Liang, L. Tian-Hua, and C. Yung-Chi, "Position control of an interior permanent-magnet synchronous motor without using a shaft position sensor," *IEEE Transactions on Industrial Electronics*, vol. 54, no. 4, pp. 1989–2000, Jun. 2007.

[47] M. Corley and R. Lorenz, "Rotor position and velocity estimation for a salient-pole permanent magnet synchronous machine at standstill and high speeds," *IEEE Transactions on Industry Applications*, vol. 34, no. 4, pp. 784–789, Jul.-Aug. 1998.

[48] K. Sung-Yeol and H. In-Joong, "A new observer design method for hf signal injection sensorless control of ipmsms," *IEEE Transactions on Industrial Electronics*, vol. 55, no. 6, pp. 2525–2529, Jun. 2008.

[49] A. Piippo, M. Hinkkanen, and J. Luomi, "Analysis of an adaptive observer for sensorless control of interior permanent magnet synchronous motors," *IEEE Transactions on Industrial Electronics*, vol. 55, no. 2, pp. 570–576, Feb. 2008.

[50] M. W. Degner, "Flux, position and velocity estimation in ac machines using carrier signal injection," Ph.D. dissertation, University of Wisconsin Madison, 1998.

[51] M. Degner and R. Lorenz, "Using multiple saliencies for the estimation of flux, position, and velocity in ac machines," *IEEE Transactions on Industry Applications*, vol. 34, no. 5, pp. 1097–1104, Sep.-Oct. 1998.

[52] P. Vadstrup and R. Lorenz, "Robust estimator design for signal injection-based ipm synchronous machine drives," in *39th Industry Applications Conference Annual Meeting*, vol. 2, Oct. 2004, pp. 957–963 vol.2.

[53] M. C. Harke, "Fundamental sensing issues in motor control," Ph.D. dissertation, University of Wisconsin Madison, 2006.

[54] Y. Young-doo, S. Seung-ki, S. Morimoto, and K. Ide, "High bandwidth sensorless algorithm for ac machines based on square-wave type voltage injection," in *Energy Conversion Congress and Exposition*, Sep. 2009, pp. 2123 –2130.

[55] S. Shinnaka, "A new speed-varying ellipse voltage injection method for sensorless drive of permanent-magnet synchronous motors with pole saliency -new pll method using high-frequency current component multiplied signal," *IEEE Transactions on Industry Applications*, vol. 44, no. 3, pp. 777 –788, May.-Jun. 2008.

[56] Z. Zhu, Y. Li, D. Howe, and C. Bingham, "Compensation for rotor position estimation error due to cross-coupling magnetic saturation in signal injection based sensorless control of pm brushless ac motors," in *IEEE International Electric Machines and Drives Conference*, vol. 1, May. 2007, pp. 208–213.

[57] P. Guglielmi, M. Pastorelli, and A. Vagati, "Cross-saturation effects in ipm motors and related impact on sensorless control," *IEEE Transactions on Industry Applications*, vol. 42, no. 6, pp. 1516–1522, Nov.-Dec. 2006.

[58] B. Stumberger, G. Stumberger, D. Dolinar, A. Hamler, and M. Trlep, "Evaluation of saturation and cross-magnetization effects in interior permanent-magnet synchronous motor," *IEEE Transactions on Industry Applications*, vol. 39, no. 5, pp. 1264–1271, Sept.-Oct. 2003.

[59] I. Boldea, M. Paicu, and G.-D. Andreescu, "Active flux concept for motion-sensorless unified ac drives," *IEEE Transactions on Power Electronics*, vol. 23, no. 5, pp. 2612 –2618, Sep. 2008.

[60] D. Reigosa, P. Garcia, D. Raca, F. Briz, and R. Lorenz, "Measurement and adaptive decoupling of cross-saturation effects and secondary saliencies in sensorless controlled ipm synchronous machines," *IEEE Transactions on Industry Applications,*, vol. 44, no. 6, pp. 1758–1767, Nov.-Dec. 2008.

[61] J. Ji-Hoon, H. Jung-Ik, M. Ohto, K. Ide, and S. Seung-Ki, "Analysis of permanent-magnet machine for sensorless control based on high-frequency signal injection," *IEEE Transactions on Industry Applications*, vol. 40, no. 6, pp. 1595–1604, Nov.-Dec. 2004.

[62] H. De Kock, M. Kamper, and R. Kennel, "Anisotropy comparison of reluctance and pm synchronous machines for position sensorless control using hf carrier injection," *IEEE Transactions on Power Electronics*, vol. 24, no. 8, pp. 1905–1913, Aug. 2009.

[63] C. Chan-Hee and J.-K. Seok, "Pulsating signal injection-based axis switching sensorless control of surface-mounted permanent-magnet motors for minimal zero-current clamping effects," *IEEE Transactions on Industry Applications*, vol. 44, no. 6, pp. 1741–1748, Nov.-dec. 2008.

[64] J. Guerrero, M. Leetmaa, F. Briz, A. Zamarron, and R. Lorenz, "Inverter nonlinearity effects in high-frequency signal-injection-based sensorless control methods," *IEEE Transactions on Industry Applications*, vol. 41, no. 2, pp. 618 – 626, Mar. 2005.

[65] N. Bianchi and S. Bolognani, "Sensorless-oriented design of pm motors," *IEEE Transactions on Industry Applications*, vol. 45, no. 4, pp. 1249–1257, Jul.-Aug. 2009.

[66] Y. Li, Z. Zhu, D. Howe, C. Bingham, and D. Stone, "Improved rotor-position estimation by signal injection in brushless ac motors, accounting for cross-coupling magnetic saturation," *IEEE Transactions on Industry Applications*, vol. 45, no. 5, pp. 1843–1850, Sep.-Oct. 2009.